ADDRESSING THE FOREIGN BODY RESPONSE TO HIGH DENSITY PENETRATING MICROELECTRODE ARRAYS

by

Michael David Polei

A dissertation submitted to the faculty of
The University of Utah
in partial fulfillment of the requirements for the degree of

Doctor of Philosophy

Department of Bioengineering

The University of Utah

August 2018

The University of Utah Graduate School

STATEMENT OF DISSERTATION APPROVAL

The dissertation of **Michael David Polei**

has been approved by the following supervisory committee members:

Patrick A. Tresco	, Chair	**March 2nd 2018** Date Approved
Robert Bowles	, Member	**March 2nd 2018** Date Approved
Robert Hitchcock	, Member	**March 2nd 2018** Date Approved
Vladimir Hlady	, Member	**March 2nd 2018** Date Approved
Paul A. House	, Member	Date Approved

and by **David W. Grainger** , Chair/Dean of

the Department/College/School of **Bioengineering**

and by David B. Kieda, Dean of The Graduate School.

ABSTRACT

The Utah Electrode Array (UEA) is a brain-implanted microelectrode recording device that has shown promise to assist patients with motor-control disabilities. Unfortunately, the UEA suffers from a foreign body response (FBR) that results in device movement away from implantation target, encapsulation of devices in meningeal origin tissue, loss of cortical tissue, and persistent neuroinflammation in the brain. These issues affect device functionality, and thus biocompatibility, and hinder widespread implementation of this technology. This dissertation examines whether device anchoring or extracellular matrix (ECM)-based device coating strategies can influence the biocompatibility of chronically implanted UEAs in the rat cortex. Results show that unanchored UEAs have a reduced FBR in comparison to those anchored to the skull, but also suffer from device movement as a result of cortical tissue remodeling, likely attributable to implantation-associated injury. To address implantation-associated injury, ECM was explored as a surface adsorbed device coating and was shown to be both hemostatic and immunomodulatory with *in vitro* assays. An apparatus was developed to coat Avitene™, an FDA-approved neurosurgical hemostatic ECM, onto the complex surface geometry of the UEA. Compared to uncoated control devices in a chronic rat model, Avitene™ coated devices experienced an enhanced FBR characterized by larger lesion cavities, enhanced meningeal encapsulation, and increased neuroinflammation, attributed to a higher degree of proinflammatory macrophages found surrounding the

device coating. These result imply that future ECM-based coatings should include immunomodulatory components that address device-adherent macrophage activation state. Critical improvements in device anchoring and modulation of the FBR are still necessary to improve the biocompatibility of the UEA. Reducing the prevalence of FBR-related device failure is a necessary step that will require further attention before patients can benefit from this technology.

For my late mother Suzanne Mary Miller Polei, who homeschooled me in elementary school, even while undergoing chemotherapy treatment. Her positive attitude, moral compass and firm resolution will always be a guide to me.

TABLE OF CONTENTS

Chapters

LIST OF TABLES

Tables

LIST OF ABBREVIATIONS

Abbreviations

3D	3-Dimensional
ALS	Amyotrophic Lateral Sclerosis
Aβ	Amyloid Beta
BBB	Blood Brain Barrier
BEC	Brain Endothelial Cell
BMI	Brain Machine Interface
CNS	Central Nervous System
CSF	Cerebrospinal Fluid
DMSO	Dimethylsulfoxide
ECM	Extracellular Matrix
ECoG	Electrocorticography
EEG	Electroencephalography
FBR	Foreign Body Response
FDA	Food and Drug Administration
GFAP	Glial Fibrillary Acidic Protein
GM-CSF	Granulocyte Macrophage Colony Stimulating Factor
GPVI	Glycoprotein VI
HFM	Hollow Fiber Membrane

ICH	Intracerebral Hemorrhage
IgG	Immunoglobulin G
IL-1	Interleukin 1
IL-6	Interleukin 6
ISO	International Organization of Standards
LFP	Local Field Potential
MEA	Microelectrode Array
MMP	Matrix Metalloprotease
MPTP	1-methyl-4-phenyl-1,2,3,6-tetrahydropyridine
MS	Muscular Sclerosis
MS/MS	Tandem Mass Spectroscopy
MTT	3-(4,5-dimethylthiazol-2-yl)-2,5-diphenyltetrazolium bromide
NHP	Nonhuman Primate
PDGF	Platelet Derived Growth Factor
PFA	Paraformaldehyde
SCI	Spinal Cord Injury
SNR	Single Neuron Recordings
TBI	Traumatic Brain Injury
TGF-β	Transcription Growth Factor Beta
TNF-α	Tumor Necrosis Factor Alpha
UEA	Utah Electrode Array

ACKNOWLEDGMENTS

I would like to acknowledge my advisor, Dr. Patrick Tresco, who has guided this work and taught me a number of invaluable lessons. His creativity, excellence of research and attention to detail are skills I have observed and learned greatly from. I also want to thank my advisory committee members: Dr. Robert Bowles, Dr. Robert Hitchcock, Dr. Vladimir Hlady and Dr. Paul House for their time spent assisting in training milestones, providing feedback and making themselves available for my training. I would like to thank other members of the Tresco Lab for their support and companionship during my studies including Dr. John Skousen Dr. Elena Budko, Dr. Ben Christiansen, Dr. Robert Oakes, Dr. Nick Nolta and Bharath Velagapudi. I would like to thank the NIH for funding my research. I would like to thank the 600+ students whom I interacted with as a 4-year TA for BIOEN 1020 Fundamentals of Bioengineering, your enthusiasm for the subject keeps me continually refreshed. I wouldn't have had the great experience that Salt Lake City has been for me without my many close friends, many of whom will never believe me when I say my research is fun and easy. Finally, I would like to thank my father, David Polei, who has never once told me to not go for something.

CHAPTER 1

INTRODUCTION TO THIS DISSERTATION

1.1 Background

1.1.1 Statement of Research

High density penetrating microelectrode arrays are cortically implanted medical devices that are intended for stimulation or recording of electrical activity at subsurface levels of the brain. Only one such device, the Utah Electrode Array (UEA), has shown promise to provide patients with motor control disabilities the ability to interact with brain machine interfaces (BMIs), allowing thought-based control of assistive technologies such as robotic prosthetics, computer control or thought-based typing (Section 2.1: Clinical Populations). Cortically implanted UEAs work by recording single unit action potentials from motor neurons with a 10 x 10 array of 1 – 1.5 mm long microelectrodes (Section 2.2: Neural Prosthetics). There are currently 10 ongoing clinical trials in the US evaluating the potential for UEAs to be used as a cortically implanted neuroprosthetic control device (**Table 1.1**). However, BMI technology has yet to move past preclinical development, largely because chronically implanted microelectrode arrays suffer from a limited functional life span.

A clinically relevant timeframe is defined as a functional lifespan whose medical benefit outweighs the costs and risks of surgical intervention. For BMIs it has been speculated that device longevity of 10 years would be the goal for a clinically relevant functional lifespan. In the largest retrospective study to date of device functionality, it was reported that the average time to failure of 78 UEAs implanted in nonhuman primates (NHPs) was only 332 days [1]. To date the longest functional device in a human has been reported out to 1000 days [2], still falling quite short of this goal.

One of the primary reasons that has been identified for this limited functional life span is the foreign body response (FBR). Over 100 published studies have extensively characterized the central nervous system (CNS) FBR to indwelling single-shank microelectrodes (Section 2.3: The Tissue Response to CNS Implants). We have learned that any device implanted in the brain will eventually become colonized by surface-bound proinflammatory macrophages and encapsulated by reactive astrocytes, concurrent with a loss of neurons in the vicinity of the implanted material [3]. A persistent goal in the field of neural engineering has been to discover strategies that can reduce the CNS FBR in order to facilitate long-term stable recording. As astrogliosis, microglial activation and neuronal loss affect the ability of implanted cortical electrodes to record high fidelity signals [4]–[7], reductions in these FBR biomarkers are indicators of biocompatibility (defined as the potential to function with integrated neural tissue [8]). Since first addressed nearly 6 decades ago [9], studies of the CNS FBR have validated a number of improvements in microelectrode designs, materials, surface coatings, and anchoring approaches.

Compared to traditionally studied single-shank microelectrodes, UEAs cause far greater penetrating damage to cortical tissue upon implantation, a result of the high number of regularly spaced microelectrode shafts [7], [10], [11]. In addition to a classical CNS FBR, UEAs experience tissue loss in the vicinity of the device, called lesion cavities, and a meningeal-origin FBR that surrounds the planar base of the device, called meningeal encapsulation [1], [7], [12]–[15]. Additionally, chronically implanted UEAs have been observed to move after implantation, often settling into these surface cavities [1], [7], [13], or being extracted by meningeal tissue [12], [14], [15], resulting in some reports of recording from a shifting population of neurons over time [16]–[18] (Section 2.4: Device Anchoring Strategies). These additional features result in a FBR that is far more complex and variable than what has traditionally been observed around single-shank devices.

As the goal of UEAs is to record single-neuron recordings from a stable population of neurons over time, reduction of lesion cavities, meningeal encapsulation or device movement would be considered improvements in the biocompatibility. This dissertation aims to better understand mechanisms behind biologic failure modes and attempt to reduce the FBR to chronically implanted UEAs.

1.1.2 The FBR to UEAs

At explant, chronically implanted UEAs are often found in locations that vary from their original implant target. Devices have been reported to be tilted, with some electrodes entirely removed from cortical contact [7], [14], encapsulated by fibrotic tissue that separates the array from cortical contact [1], [12], [14], [15], [19], or settled into cortical surface depressions, where electrodes are deeper than originally implanted[1], [7], [12]–[14], [16]–[18], [20]. These issues of device movement constitute a major biological failure mechanism for UEAs. To date, the majority of implanted UEAs have been secured using an unanchored approach, where devices are not rigidly secured to the skull after implantation, but rather left freely floating. A number of studies have compared the tissue response to chronically implanted anchored and unanchored single-shank microelectrodes [21]–[25]. Anchored devices experience far greater reactive gliosis and neuronal loss, leading to a widely accepted view that freely floating strategies are preferable to minimize the FBR. However, these studies have never been performed with a high density penetrating array like the UEA, the only microelectrode recording device currently under clinical investigation

Previous efforts in our lab implanted rats with unanchored 4 x 4 recording UEAs and observed a steep drop off in the number of functional devices and recordable single units with time [7]. Loss of recording performance was correlated with blood-brain barrier (BBB) dysfunction, astrogliosis and cortical tissue loss under the device. To further understand the impact of UEA implantation, rats were implanted with a UEA, which was removed after two minutes and allowed to recover for 4 weeks, resulting in what is called a stab wound injury. In both implanted and stab wounded rats a pyramidal shaped lesion cavity was observed under the implant location, indicating that vascular damage from implantation was sufficient to cause tissue loss, even in the absence of an indwelling device. Currently observed biological failure mechanisms suggest that the tissue changes observed around implanted UEAs are likely a combination of implantation-associated injury and a chronically sustained FBR.

Due to the highly vascularized nature of the cortex, implantation of high density devices with regular and closely spaced microelectrode shafts ruptures blood supplying descending arterioles or ascending venules (Section 2.5: Neurovasculature). Short-term implantation studies in humans have shown that implantation of the UEA causes significant vascular damage along electrode tracts and the formation of subcortical hemorrhage [10]. This damage is called a focal cerebral insult, which is a term used in stroke and traumatic brain injury (TBI) research to describe localized damage to the brain and neurovasculature.

Studies of focal cerebral insults show a pattern of changes in the CNS architecture that is quite similar to the response observed around stab-wounded or animals implanted with high density penetrating UEAs (Section 2.6: The Glial Response to Injury). By acknowledging that insertion of multiple side-by-side penetrating shafts causes a notable focal cerebral insult, it is possible to expand our knowledge of implantation associated injury by studying the biological response to stroke, TBI and meningeal injury.

Experimental stroke models in rodent cortex can occlude blood flow in single penetrating arterioles or ascending venules, creating localized vascular insults much like those caused by electrode insertion [26]. Occluding a single penetrating vessel, with a diameter of 10 - 100 μm, leads to the formation of microinfarcts 450 μm in diameter and 1 mm deep. Furthermore, when such occlusions are spaced closer than 1.6 mm from each other, the resulting infarctions coalesce to form larger areas of cortical tissue loss than would be predicted with isolated occlusions. As UEA electrodes are only spaced 0.4 mm from each other, it is likely that multiple penetrating injuries act in concert and result in the characteristic lesion cavities observed under implanted UEAs.

In addition to disturbing vascular perfusion and creating stroke-like damage, the implantation of a UEA into the cortex causes localized bleeding and intracerebral hemorrhage (ICH) similar to that observed in TBI. Blood is normally excluded from the brain by a highly specialized vascular barrier, known as the blood-brain barrier (BBB). In the healthy brain, the BBB excludes the extravasation of plasma components such as thrombin, fibrinogen and complement, which have known deleterious effects on neuronal viability [27], [28]. When blood products are experimentally injected into rat cortex and compared to injection of equivalent amounts of saline, the area of neuronal loss is enhanced by an order of magnitude [29]. Research indicates that intracerebral hemorrhage associated with UEA implantation could be a likely contributor to the lesion cavities and neuronal loss observed under implanted, or stabbed, devices.

Following dural resection or controlled cortical impact, the meningeal response to injury results in proliferation of meningeal tissue and formation of a fibrotic scar. Implantation of a UEA creates a comparable damage as the dura is resected and electrodes are pushed through the pial layer of the meninges during insertion (Section 2.7: The Meningeal Response to Injury). A hallmark of the meningeal response to injury is recruitment of nonneuronal cell types including leukocytes, fibroblasts and mesenchymal stem cells that create a fibrotic scar along the injury profile that is nonpermissive to neuronal regeneration [30]. The injury-activated connective tissue grows into lesion cavities and shares many features with the connective tissue observed encapsulating extracted UEAs. This tissue is characterized by the presence of activated macrophages, dural fibroblasts and associated deposition of fibrous extracellular matrix (ECM) such as collagen [31]. This fibrotic scarring is also observed around the base of chronically implanted UEAs, often times notably thicker than uninjured meninges, indicating that the meningeal response to injury is likely involved in fibrotic encapsulation of UEAs.

The development of lesion cavities and a meningeal-origin fibrotic scar in response to UEA implantation compromises the ability of UEAs to record from intact neural tissue. Furthermore, lesion cavities, fibrotic scarring and the FBR create an area of reactive gliosis that is associated with decreased neuronal density and demyelination in the parenchyma surrounding reactive areas [32]. As such, approaches that could limit implantation associated injury or the FBR to UEAs would likely lead to improvements in device biocompatibility and allow UEAs to move forward as a clinically utilized device to restore sensation in patients with motor control disabilities.

1.2 Research Focus

One noted biological failure mechanism of chronically implanted UEAs is the propensity of these devices to move from their original implant location when left freely floating on the cortical surface, only loosely tethered by the bundle of wires that comes off the back platform of the UEA (Section 2.7: Device Anchoring) [1], [7], [14]. A variety of studies have indicated that CNS implants anchored to the skull have an increased FBR, presumably due to enhanced strain at the device-tissue interface while freely floating devices have a lower FBR [21], [33]. However, similar studies of device anchoring have never been performed with high density penetrating devices like the UEA where the FBR includes the additional issues of device movement, meningeal encapsulation and lesion cavity formation. In Chapter 3 we use a rodent model to build upon previous studies of device anchoring to determine if freely floating, unanchored UEAs have a reduced FBR compared to devices anchored to the skull. The focus of this study was to elucidate mechanisms responsible for device movement and the ensuing FBR in order to inform the future device anchoring strategies for high density recording microelectrode arrays.

Due to the highly vascularized nature of cortical tissue, the implantation of devices with regular and closely spaced microelectrode shafts creates considerable vascular damage leading to substantial tissue loss on the cortical surface. In the neurosurgical suite, hemostats are routinely utilized to control bleeding and limit hemorrhage associated injury. Extracellular matrix (ECM) based hemostats are naturally derived glycoproteins and carbohydrates that contain collagen, a natural agent that stimulates the coagulation cascade [34]. Lesion formation has been attenuated with ECM in both stroke and TBI models of cerebral insult, indicating that ECM-based approaches to limiting tissue loss could prove advantageous [35], [36]. Indeed, a limited number of studies have shown positive improvements in the FBR to single-shank microelectrodes using both surface adsorbed ECM components and intact ECM [37]–[40]. In Chapter 4, a variety of ECMs were isolated and tested for their hemostatic and immunomodulatory capability. The complex geometry of the UEA makes uniform surface adsorption difficult, so an apparatus was developed and parameters were empirically derived to uniformly coat the FDA-approved neurosurgical hemostat, Avitene™ (a bovine-derived microfibrillar collagen hemostat), onto the surface of a UEA. This chapter focuses on the isolation of cell-type specific ECM, *in vitro* testing of ECM, and development of a device coating method that is necessary to study the effect of an ECM coating on the FBR to UEAs.

Intracerebral hemorrhage is sustained during the implant of a UEA, with blood accumulating along electrode tracts, below the electrode tips, and observed on the surface of stabbed devices [7], [10]. The extravasated blood has deleterious effects in the cortical parenchyma, resulting in neuronal death, tissue necrosis and lesion formation [27], [29]. In Chapter 5, anchored devices coated with the hemostatic ECM, Avitene™, were implanted chronically into rats to determine if a hemostatic device coating can limit tissue loss surrounding implanted devices and reduce elements of the FBR. In this chapter we tested the hypothesis that limiting initial blood loss associated with implantation using a surface adsorbed, clinically used hemostat will lead to decreased areas of tissue loss under the device and would reduce the FBR surrounding implanted UEAs.

1.3 Research Objectives

The *long-term goal* was to improve the biocompatibility of the UEA by using biologically informed approaches to minimize the stroke-like lesion cavity associated with implantation and reduce the chronic FBR.

The *objective* of these experiments was to investigate device anchoring strategies and ECM-based device coatings in an effort to minimize device movement and address cortical lesion formation that occurs under chronically implanted devices.

The *central hypotheses* were; 1) strategies to anchor UEAs would lead to a reduction of device movement from implantation target, and 2) a hemostatic device coating will lead to reduced lesion cavity size and the decrease the relative distribution of FBR biomarkers in the vicinity of coated devices.

The *rationale* for these experiments was motivated by findings that chronically implanted UEAs are found recessed into cortical surface depressions, sometimes heavily tilted and moved from original implant location, and by emerging evidence that suggests that ECM can attenuate lesion formation in stroke and TBI and improve aspects of the FBR to single-shank microelectrodes.

1.4 Significance

The value of this dissertation is provided in the approaches described that aim to validate a number of clinically translatable methods to improve the biocompatibility of a neural recording device currently under clinical evaluation. These devices show incredible promise to assist patients suffering from motor control disabilities, but show unsatisfactory performance in the chronic setting. Here we investigate pragmatic approaches that may have near immediate impact on improving the functionality, and thus biocompatibility, of implanted UEAs.

Very few studies have detailed the histological changes that occur around the UEA over chronic implant durations, in spite of the fact that the FBR has been indicated as a major failure mode in chronic applications [1], [7], [12], [14], [15]. Chapter 3 asked a largely unaddressed question, whether a simple change in anchoring strategy can reduce changes in implant trajectory without greatly affecting the FBR in the recording zone. In Chapter 4, methods were developed that will facilitate the study of a wide variety of cell-type specific ECM constituents as surface-adsorbed device coatings to improve biocompatibility of many types of implanted materials. Chapter 5 investigated a clinically utilized neurosurgical hemostat to determine if such a device coating could improve aspects of the FBR to UEAs. Conclusions from these studies will inform the design of next generation microelectrode recording arrays, moving us incrementally closer toward the goal of long-term stable neural interfaces for BCI control.

Table 1.1 Ongoing Clinical Trials of Intracortical Microelectrodes.

This table was compiled from searching ClinicalTrials.gov for the following search terms: Tetraplegia, Paraplegia, BCI, BMI, Intracortical, intracerebral, microelectrode, cortical electrode. Results were excluded if electrodes were intended for intraoperative use or implant durations less than 2 days, additionally deep brain stimulation (DBS) systems, were excluded unless the target implant location was the cortex. This table shows that the only device currently under clinical investigation for brain-machine interfacing (BMI) is the Utah Electrode Array (UEA).

Start Date	Identifier #	Title	Institution	Condition	Treatment	Device Type
Jul-05	NCT00122915	CONCEPT: Crossover Efficacy Pain Trial in Motor Cortex Stimulation for Intractable Neuropathic Pain	Medtronic	Intractable pain, Facial Pain	Pain mgmt	DBS lead
Jun-09	NCT00912041	BrainGate2: Feasibility Study of an Intracortical Neural Interface System for Persons With Tetraplegia (BrainGate2)	Hochberg Group, Massachusetts General hospital	Tetraplegia SCI, ALS, Brain stem infarctions, Locked in Syndrome, Muscular Dystrophy	BMI	UEA
Jun-11	NCT01364480	Microelectrode Brain-Machine Interface for Individuals With Tetraplegia	University of Pittsburgh, Johns Hopkins	Tetraplegia SCI	BMI	UEA
May-13	NCT01849822	Providing Brain Control of Extracorporeal Devices to Patients With Quadriplegia	University of Southern California	Tetraplegia	BMI	UEA
Jul-13	NCT01894802	Cortical Recording and Stimulating Array Brain-Machine Interface (CRS-BMI)	Johns Hopkins University	Tetraplegia SCI, stroke	BMI	UEA

Table 1.1 Continued.

Start Date	Identifier #	Title	Institution	Condition	Treatment	Device Type
Oct-13	NCT01964261	Providing Closed Loop Cortical Control of Extracorporeal Devices to Patients With Quadriplegia	University of Southern California	Quadraplegia	BMI	UEA
Oct-13	NCT01958086	Brain Implant for Neural Control of a Computer	University of California, Los Angeles	SCI	BMI	UEA
Oct-13	NCT02932839	Investigating the Neuronal Bases of Epilepsy With Microelectrode Arrays in Candidates for Epilepsy Surgery (IN-MAP)	Wyss Center for Bio and Neuroengineering	Epilepsy	Surgical Planning	UEA
Nov-13	NCT01997125	Reanimation in Tetraplegia	The Ohio State University	SCI	BMI	UEA
Jul-15	NCT02491476	Recording "Fast Ripples" Using Microelectrodes During Stereoencephalography in Patients With Drug-resistant Partial Epilepsy (Epi-FaR)	University Hospital Toulouse	Epilepsy	Surgical Planning	Depth Electrode
Dec-16	NCT02983370	Development of a Cortical Visual Neuroprosthesis for the Blind (CORTIVIS)	Universidad Miguel Hernandez de Elche	Blindness	BMI	UEA
Apr-17	NCT03100110	NeuroCognitive Communicator: Safety Study (NCC-1701)	Ottawa Hospital Research Institute	SCI, ALS	BMI	UEA
May-17	NCT03161067	Investigation on the Bidirectional Cortical Neuroprosthetic System (BiCNS)	Johns Hopkins University	Rehabilitation	BMI	UEA

CHAPTER 2

THE FOREIGN BODY RESPONSE TO CNS IMPLANTS:
AN OVERVIEW

2.1 Focused Clinical Populations

2.1.1 Motor-Control Disabilities

Hundreds of thousands of Americans suffer from motor-control disabilities in which brain-derived processes cannot generate functional movement due to nervous system dysfunction as a result of damage to the brain, spinal cord or muscles [41]. For many of these conditions functional recovery is not an option. Currently, patients must learn to live with their disabilities, often further debilitated by substantial costs in living and healthcare expenses. The field of Neural Engineering aims to reconnect these patients with their bodies or extracorpeal devices by using neural recording interfaces to provide thought-based control of Brain Computer Interfaces (BCI). Outlined below are the three leading causes of motor function disabilities, a summary of the patient populations affected and the overall economic burden. The strategies discussed in this dissertation aim to improve BCI technology that could vastly improve quality of life for these patients and decrease the economic burden associated with long-term care for affected individuals.

It has been estimated that there are currently between 240,000 and 370,000 Americans living with spinal cord injury (SCI), an injury primarily associated with automobile accidents [41], [42]. Furthermore, it has been estimated that between 12,000 and 20,000 new cases present themselves each year [42]. The severity of injury can range from incomplete paraplegia (40 %), in which the legs suffer partial loss of function all the way to complete paraplegia (20 %), in which patients loose motor and sensory function in all four limbs. The costs associated with these injuries varies, but the overall mean cost is $523,089 in the first year and $79,759 per year following injury [43]. In one study 57 % of SCI patients reported having a job before their injury, while only 11.8 % had a job the year following injury; underscoring the tremendous difficulties these patients face as they reintegrate with their environment [42]. Overall it has been estimated that SCI-related disabilities create between $7.7 and $9.7 billion in direct medical expenses and roughly $5 billion in estimated annual indirect cost to patients [44].

Stroke is the primary cause of CNS-related disabilities in the US. A stroke refers to a cerebrovascular insult that typically results in loss of cognitive or motor function. Two forms of stroke are: ischemic, where a blood vessel becomes blocked, or hemorrhagic, where a blood vessel ruptures. Depending on the location of the stroke, patients can suffer severe disabilities that will last a lifetime. As of 2017, 7.2 million Americans have had a stroke, with 795,000 new cases reported annually. The direct medical cost of stroke is $17.9 billion, indirect costs make up another $16 billion annually [45]. For patients with brain stem strokes or strokes in the motor cortex, the consequence is permanent paralysis, referred to as locked-in-syndrome. Approximately 5-10 % of all hemorrhagic stroke occur in these regions, with 39 % of patients dying within the first 30 days and only 9.6 % of patients experiencing functional recovery [46]. For the remainder of these 20 - 40 thousand patients per year, BCIs could offer assistance in regaining motor control.

An estimated 1.6 million Americans suffer from limb loss, with the primary causes being a combination of vascular disease and complications related to diabetes followed closely by trauma-related amputations [47]. These patients are limited in their functional ability based on the severity and location of limb loss [44]. Some of these patients could be assisted by BCI technology. It has been estimated that the cost of hospital care for amputees was roughly 9 billion dollars in 2013 [44].

2.2 Focus Area within the Field of Neural Prosthetics

2.2.1 Overview

Neural prosthetics show promise to help restore neural connectivity lost as a result of damage or disease [48]. The basic premise of these devices is that a neural interface is used to either stimulate electrical activity in the brain, and use this information to restore sensation, or record activity in the brain, and use this information to control assistive medical devices like powered wheelchairs, computers or prosthetic limbs. The first Food and Drug Administration (FDA) approved neural prosthetic device, the cochlear implant has been in use since the mid-1980s. Cochlear implants restore hearing to profoundly deaf adults and children using a two-part system comprised of an external microphone and an implanted electrode system that stimulates the auditory nerve. Today, roughly 45,000 cochlear implants are sold every year, highlighting the potential of neural prosthetic devices as a clinically relevant tool to restore lost function [49].

In addition to restoring hearing, neural prostheses have been utilized to restore bladder function and respiration, alleviate chronic pain, restore basic visual perception in the blind, and control Parkinson’s tremor, epilepsy and obsessive-compulsive disorder.

In all of these examples the neural prosthetic works by directly interacting with the nervous system using implanted electrodes that stimulate neural activity. In addition to stimulating electrodes, neural prosthetics can also utilize recording electrodes to translate signals from the body to the outside world.

Neural recording devices offer the possibility of BCIs, where a user would only need to think to control devices like robotic prosthetics. The four basic modalities for recording neural information are electroencephalography (EEG), [50], electrocorticography (ECoG) [51] and implanted microelectrode arrays (MEAs). Each of these modalities has an increasing degree of evasiveness, EEG sits atop the skull, ECoG sits under the skull and microelectrodes are implanted into the cortex to collect single-neuron recordings (SNR). SNR provides the fastest and most responsive neural interface; however, this high specificity comes at the expense of very delicate devices that are influenced by physiological changes that occur at the device-tissue interface. Following implantation into the mammalian cortex a sequence of events occurs eventually resulting in decreased neuronal density in the vicinity of devices. This neuroinflammatory sequella is collectively referred to as the CNS FBR. As implanted intracortical microelectrodes have shown the highest potential for fine neural control, stabilizing the CNS FBR has been a goal of neuroscientists since the late 1950s. The remainder of this dissertation will focus on intracortical MEAs, as they show the highest potential for improving the lives of patients with motor-control disabilities.

2.2.2 Intracortical Microelectrodes

A variety of microelectrode designs and configurations are available for intracortical stimulation and recording. This subsection will briefly review the three basic configurations of implanted microelectrodes: microwires, planar microelectrodes and multielectrode arrays. All of these devices are influenced by the FBR, as this neuroinflammatory sequella results in eventual failure of devices to record in the chronic setting. A number of design improvements to intracortical microelectrodes made over the last half century have been validated by studies that show a reduction in the FBR and improvements in recording capability.

Microwires were of the first and most basic implanted electrodes. In 1942 Grundfest and Campbell used 50 to 250 μm stainless steel wires sharpened to a roughly 20 μm point to record neural activity in the spinal cord of cats [52]. By 1957 this method was improved to use 125 μm diameter tungsten microwires, which could be sharpened to a 5 μm tip, allowing for recording of single-unit action potentials in the cortex of cats. Further work in the 1960s identified that certain metals, like silver and tungsten had a much more "violent" tissue response than metals like stainless steel and gold [53]. Utilizing available information, in 1976 Salcman and colleagues developed a microelectrode intended for chronic recording, composed of an iridium wire insulated with poly-monochloro-p-xylene (Parylene-C) [54]. Using this electrode, Schmidt *et al.* recorded neural activity from unrestrained monkeys for up to 223 days [55]. This was also one of the first studies to note that electrode impedance increased for the duration of the implant and that gliotic encapsulation may contribute to this decrease in recording performance.

In the early 1970s advances in integrated circuit design allowed Dr. Wise at Stanford University to create a silicon based planar microelectrode [56]. Utilizing silicon manufacturing techniques to place gold recording sites along a silicon substrate, these electrodes could be designed in any 2 dimensional fashion and even allow multiple recording sites along the electrode. After a brief funding gap in the 70s and a move to the University of Michigan, continued work in 1986 by Dr. Wise highlighted the ability of these planar microelectrodes to record single-unit action potentials in gerbils and rats when implanted into the cortex [57], [58]. Planar microelectrodes offered a significant advantage over microwires in that multiple recording sites could be combined into one device, and the distance between recording sites remained well defined over time. This style of electrode became known as the "Michigan" probe, and was an important tool used for understanding neural connectivity in the 90s [59], [60]. Dr. Wise estimates that over 10,000 of these devices have been distributed to neuroscience research labs across the world.

Around the same time as the invention of the planar microelectrode, Dr. Richard Norman at the University of Utah began developing a silicon-based multishank MEA. Originally developed to stimulate the visual cortex in blind patients, this device was able to incorporate 100 closely spaced microelectrodes that could all be implanted to the same depth [61]. This device, known as the Utah Electrode Array (UEA), is built from a top-down dicing and etching process in which a silicon wafer is cut down to a 10 x 10 grid of 1 - 1.5 mm length microelectrodes. These electrodes are spaced 400 µm apart and each one has a platinum coated tip which records signals that transmit down the P-doped silicon electrode shaft, insulated with Parylene-C. On the backside of the device electrodes are wire-bonded to individual gold wires that are grouped into a trailing wire bundle that extends off one end of the device. This wire bundle has a connector on the other end that is typically affixed to the animal's skull, in what is referred to as a headstage.

The UEA has since been studied for use in the auditory cortex [62], the olfactory bulb [63], cochlear nerve [64], barrel cortex [65], and extensively in the motor cortex [1], [66]–[73]. The UEA is also the only microelectrode type that has been chronically implanted in humans in a variety of ongoing clinical trials (**Table 1.1**) [2], [66], [67], [71], [72], [74]–[76]. These trials have shown that cortically implanted UEAs can be used to connect paralyzed patients with assistive technologies.

Although many microelectrode designs exist for research uses, only the UEA has gained traction as a clinically utilized device. For this reason, the focus of this dissertation will be on methods to improve the biocompatibility of high density penetrating UEAs; although many of the findings could hold relevant for a variety of CNS implant designs.

2.2.3 Functional Longevity of High Density Penetrating Arrays

The longevity of multielectrode arrays, defined as the time frame in which they can collect useful signals, has been investigated in a number of animal and clinical trials. The eventual goal of this technology is to develop stable recording interfaces that can function for periods out to 10 years, so as to outweigh the cost and risk of surgical intervention. In 1998 the Normann group at the University of Utah (U of U) reported recording metrics for UEAs in cats and showed that only 60 % of arrays were capable of recording discernable neural activity 6 months after implant [12]. Additionally, spiking appeared to generate from a shifting population of neurons. In 2005 Suner *et al.* published finding from their experience in a number of nonhuman primates (NHPs) with recordings out to 83, 179 and 564 days. They also reported that neural waveform varied between, but not within, recording days; suggesting a shifting population of recorded neurons over time [17].

In 2013 the Donoghue group at Brown University compiled recording data from 78 NHPs implanted for durations of 0-5.75 years and performed a retrospective analysis to determine failure modes and observed recording longevity [1]. **Figure 2.1** shows the array time to failure over 50-day intervals, and indicates a steep drop off of recording longevity for the majority of arrays. In particular, this study noted that 56 % of failures occurred with the first six months of implant, and that biological failure modes accounted for 60 % of all chronic failures. They also noted that neural recordings showed a progressive drop in impedance, signal amplitude and viable channels over time, with the longest time to failure at 1008 days post implant. This study demonstrated that long-term functionality of cortically implanted UEAs is still an elusive goal. How and why these devices fail in the chronic setting is important to determine before sending patients home with this technology.

2.2.4 Failure Modes of UEAs

For MEAs to be adapted clinically it has been suggested that these devices should function for 10 years or longer to outweigh the cost and risk of surgical intervention. To date, the longest published functional MEA in a human has been observed to last 1000 days, however this is only one example out of 10 ongoing clinical investigations utilizing these devices (**Table 1.1**) [68]. At present, the UEA is the only microelectrode recording device that is gaining clinical traction, in spite of a number of studies showing that such devices have a propensity for failure to record over long implant durations [1], [7], [12], [14], [15].

It has been determined that UEAs fail to record due to three primary reasons: mechanical, material, or biologic failures [1]. Mechanical failures include breakage of wire bundle, connector damage, headstage failure and physical extraction of the device by the animal. Mechanical failures usually occur in the operating room or in the acute setting [1], [7]. Material failure refers to a loss of insulation on the electrode shaft, resulting in decreased impedance and poor signal quality [14], [77]–[80]. It has been shown that the physiological environment surrounding chronically implanted devices is capable of causing these material failures [80]. These issues are being addressed by improvements in manufacturing and materials selection, but the biological response to the implanted devices still deserved further attention.

The biological response to implanted devices constitutes the remainder of failure modes and is often most prevalent at chronic time points. Barrese *et al*. reported that 60 % of chronic failures in NHPS were due to biological related reasons [1]. In rodents, two studies have shown that 40 % of implanted devices fail due biological related failure mechanisms [7], [15]. These biological failure modes are a direct result of the FBR to implanted electrodes including: neuronal tissue loss, meningeal encapsulation and device movement away from recording site. While the FBR to single-shank microelectrodes is a well-characterized neuroinflammatory sequella, relatively few studies have performed an in-depth investigation of the FBR to chronically implanted UEAs.

2.2.5 Focus Area

While material and mechanical failure modes leave room for improvement in the longevity of implanted UEAs, we believe that these strategies can be addressed by relatively straightforward design modifications to the existing technology. However, the

FBR to implanted UEAs seems to result in a variety of biological failure modes, including cortical tissue loss, meningeal encapsulation and device movement. These varied and undesirable responses indicate that a variety of factors are at play, and highlight a need for further understanding of the FBR to UEAs. The focus of this chapter is to improve the reader’s understanding of the FBR to high density penetrating devices like that UEA. Due to a lack of studies using high density penetrating devices, this will require leaning on the fields of traumatic brain injury, stroke and intracranial hemorrhage to understand the fundamental biological changes that occur when high density penetrating devices are implanted into the cortex.

To establish what is currently known of the FBR to microelectrodes, Section 2.3 will discuss what is known of the FBR to both single and multishank microelectrodes. Device movement is a variable that this dissertation intends to address, so Section 2.4 will explore previous studies of device anchoring and reports of UEA movement. Because electrode implantation results in vascular damage, Section 2.5 will detail the highly vascularized nature of the cortex, explain the blood-brain barrier (BBB) and draw comparisons between human and rodent neurovasculature. As studies of UEA implantation-associated damage are rare, Section 2.6 will explore how focal cerebral insults, like stroke and TBI, are resolved in the absence of a foreign body. Due to a prevalence of meningeal encapsulation, Section 2.7 will explore the meninges and their response to injury. By gaining an understanding of the FBR and implantation-associated injury, we can begin to address biological failure modes in Chapters 3 – 5.

2.3 Foreign Body Response to CNS Implants

2.3.1 Overview

The FBR to microelectrodes is a well characterized neuroinflammatory sequella, with an estimated 100 or more publications since the first study by Collias and Manuelidis in 1957 [9], [81]. The majority of studies performed to date have characterized the FBR using either microwires or planar silicon electrodes, as these were of the first utilized electrode types. Less work has focused on characterizing the response to higher density devices with multiple electrode shafts, as multiple side-by-side reactions complicate understanding.

Higher density devices have a seemingly more variable FBR than what is observed around single electrodes [19]. In particular, there are increased areas of neural tissue loss, called lesion cavities, which present as either fluid-filled (cystic) or filled with meningeal tissue (fibrotic). Lesion cavities often span multiple electrodes and are highly variable in shape and size [7], [19]. In rats, these cavities take on a pyramidal shape that decreases as a function of depth [7]. In felines and NHPs, similar loss of cortical tissue under the device has been described as “device settling” [1], [12], [13]. These reports are explored in the subsection labeled “Lesion Cavities.”

Within cortical surface depressions and lesion cavities, we find fibrotic tissue that is continuous with the meninges. This fibrotic tissue often encapsulates the base of the device and a portion of the electrode shafts [1], [7], [12], [14], [15]. This meningeal encapsulation has been report to entirely encapsulate devices, preventing contact with cortical tissue [12], [14], [15]. All available reports of UEA encapsulation are reviewed in the subsection “Meningeal Encapsulation.”

Device movement away from implantation target is a noted biological failure mode that is likely a result of the 2 aforementioned variables, lesion cavity formation and meningeal encapsulation, or other yet to be determined mechanisms. This problem is explored in detail in Section 2.4.

This section will focus first on the inflammatory cascade that follows implantation of a single microelectrode and then consider the differences that appear when a high density penetrating microelectrode array is implanted in the cortex.

2.3.2 The FBR to Single-shank Microelectrodes

Nonhuman primate (NHP), feline, rabbit and rodent animal models have all been utilized and have been observed to share a very consistent neuroinflammatory sequella following implantation of a single electrode, known collectively as the CNS FBR. **Table 2.1** details the historical contributions that have led to our understanding of this CNS FBR. These shared features are herein referred to as classic or hallmark sings of the CNS FBR as they are conserved across species and show similar morphology and distribution regardless of animal model studied.

Insertion of an electrode into the cortex invariably ruptures a number of capillaries, as the cortex is a highly vascularized structure. When implanting various device shapes at a number of different speeds, Bjornsson and colleagues noted bleeding as a result of electrode insertion [82]. They found that insertion at higher speeds helps minimize cortical surface deformation, but still severing, rupturing and dragging of blood vessels was noted in areas several hundred micrometers from the insertion site.

Resulting from vascular rupture, serum-derived proteins, complement molecules and other blood-derived factors are the first to colonize the surface of implanted devices [83]. Vascular rupture activates extrinsic clotting cascade via exposure of tissue factor on vascular wall cells, which binds and activates factor VII, initiating the extrinsic coagulation cascade [84]. Factor XII adsorption to the electrode surface initiates the contact pathway of the clotting cascade [84], [85]. Both pathways eventually result in conversion of prothrombin to thrombin, which activates platelets and initiates fibrin polymerization, eventually resulting in the formation of a primary hemostatic plug [86].

This plug is rich in chemoattractant molecules like transforming growth factor beta (TGF-β), platelet derived growth factor (PDGF) and interleukin-1 (IL-1) that direct macrophages to the wound site [87]. The complement system is also activated by adsorption of plasma proteins to the biomaterial surface. Complement signaling recruits inflammatory cells to the site of injury utilizing the alternative arm of the complement cascade [88]. In the early stages of electrode implantation endogenous wound healing mechanisms recruit neutrophils and later macrophages to the site of injury [89]. These macrophages colonize the surface of the implanted biomaterial and further propagate inflammatory signals by releasing PDGF, tumor necrosis factor alpha (TNF-α), interleukin 6 (IL-6) and granulocyte macrophage colony stimulation factor (GM-CSF) [87]. Macrophages persist on the device surface for the duration of implant [3], [21], [90]–[92], and remain highly activated, a phenotype associated with further release of proinflammatory cytokines [93].

Macrophages also attempt to degrade the foreign material by releasing reactive oxygen species and degrative enzymes in what has been deemed a “classical” activation state [94]. These classically activated macrophages have been shown to induce neurotoxicity [95], as the signals they release diffuse from the device surface and into the surrounding tissue [96]. Upon unsuccessful degradation of the implanted biomaterial macrophages enter a stage called frustrated phagocytosis, where macrophages begin to fuse into multinucleate foreign body giant cells (FBGC) [97], [98].

The consequence of these persistent inflammatory stimuli on the device surface is astrogliosis, which refers to the formation of a compacted area of high astrocyte density along the electrode surface. Macrophage secreted cytokines have the ability to activate astrocytes, a fibroblast-like, glial-derived cell that is responsible for maintaining CNS homeostasis [99]. Astrocytes are also activated by hypoxic stress and osmotic pressure related with CNS ischemia [100]. The hallmark sign of astrocyte activation is upregulation of the intermediate filament GFAP and a hypertrophic morphology. In the first 24 hours following injury, astrocytes are observed to be activated near the implant site and as far away as 400 μm away from the site [37]. As soon as one week after implant the astrocytes form a tight band of GFAP+ immunoreactivity around the surface of the electrode, presumably in an effort to wall of the inflammatory signals produced by surface-adherent macrophages [37]. Turner *et al.* studied the time course of astrogliosis and showed that GFAP immunoreactivity extended 500 μm from the implant interface at 2 weeks post implant, but had compacted to a continuous sheath by 6 weeks post implant [101]. It has been suggested that astrogliosis is responsible for excluding nearby neurons from the vicinity of the device [16], [101], [102], increasing electrode impedance by limiting diffusion [103], or creating a inhibitory environment that prevents neural processes from contacting recording sites [104].

In the vicinity of the device, where gliosis is ongoing, there is a decreased density of neurons adjacent to the device [98]. Earlier studies showed a variety of distances this decreased neuronal density travelled, ranging from 10 μm to 100 μm [101], [105]. First quantified by our group in 2005 [3], extensive characterization has led to the generally accepted consensus that neurons show a 40 - 60 % reduced density in the first 100µm away from the surface of single-shank electrodes [81], [106], [107]. As current recording mechanisms require neurons to be within 140 µm of recording tips, this loss of neurons has been presumed to contribute to declining electrode performance [60].

Blood brain barrier (BBB) dysfunction is another classic hallmark of chronically implanted microelectrodes [108], [109]. The BBB is a term used to describe the series of tight junctions surrounding neurovasculature that is responsible for preventing the extravasation of serum proteins, circulating neurotransmitters (i.e., glutamate) and soluble factors not normally found in the brain parenchyma [110]. In conditions of chronic inflammation, such as that observed near implanted microelectrodes and in a variety of other CNS pathologies, the BBB becomes chronically compromised as evidenced by secretion of serum proteins like immunoglobulin G (IgG) and albumin in the CNS parenchyma [111]. Extravasated serum, compliment and coagulation components activate endogenous protection mechanisms and activate nearby microglia [27], [112]–[115]. Activated microglia secrete a number of proinflammatory cytokines that recruit cells to the area; this recruitment leads to further breakdown of the BBB as recruited cells disrupt BBB integrity via trafficking across it and phagocytosis of vascular wall endothelial cells [27], [115], [116]. This cycle, where BBB disruption leads to further BBB disruption has been described as a vicious cycle, where initial insult leads to a sustained inflammatory response[117].

The chronic FBR is a relatively stable and repeatable response that occurs around all devices implanted in the brain. **Figure 2.2** shows a representative image of the FBR to a single-shank Michigan electrode chronically implanted in a rat cortex [3]. It is observed that ED1+ (analogous to the CD68 antigen used in this dissertation) activated macrophages accumulate near the device surface. Surrounding these inflammatory cells, a layer of GFAP+ astrogliosis is observed. Within the first ~100 µm there is a reduction in neuronal cell bodies (NeuN) and neurofilament (NF). Later studies have also established that IgG immunolabeling is enhanced surrounding chronically implanted devices [106], indicative of BBB dysfunction that likely compromises neuronal health in the vicinity of devices.

2.3.3 The FBR to Multishank Microelectrode Arrays

Nearly all long-term recording studies in humans and NHPs have been conducted using multielectrode arrays, predominantly the UEA. To date, a limited number of studies have investigated the tissue response when MEAs with multiple electrodes are implanted into the cortex. **Table 2.2** highlights all previous studies that have included any histological assessment of the FBR to implanted UEAs. Many of these studies lack comprehensive assessment of all samples; often only a small percentage of animal histology is reported. Furthermore, these published studies only show histology to select animals; rarely using representative images that show the cohort mean response. The work completed in this dissertation intends to address this lack of knowledge by using clearly defined methods and reporting results observed as cohort means.

When electrode shafts are located within neural tissue, the FBR to UEAs is characterized by all of the hallmark signs of a CNS FBR that have been described to single-shank devices. These include including microglial cell attachment, astrogliosis and neuronal loss in the vicinity of implanted electrodes [7]. This classical FBR, however, has not been implicated as the major cause for biological-related failure modes. Declines in recording performance are often attributed to lesion cavities under the device [7], partial or complete meningeal encapsulation of the UEA [1], [7], [12], [14], [15], or devices moving or tilting away from implantation target [1], [7], [15], [17].

2.3.4 Lesion Cavities

Initial trauma from insertion is invariably higher when implanting a high density intracortical MEA, as the increased number of electrodes increase the number of capillaries ruptured and make avoiding visible surface vessels much more difficult. Using literature values of capillary density in rodent brain, it can be calculated that the insertion of a 4 x 4 UEA, such as those utilized in this dissertation, will rupture at least 750 capillaries [118]. Indeed, when Dr. Paul House and colleagues implanted 10 x 10 UEAs into human cortex for short durations they noted grossly visible subarachnoid hemorrhage associated with each penetrating shaft and in an area of a few millimeters surrounding the device. When assessed histologically, acute petechial hemorrhage was noted under tips of the device, below the penetrating injury (**Figure 2.3**) [10], [11]. Similarly, Nolta *et al.* briefly stabbed rats with a 4 x 4 UEA and reported that retrieved devices were coated with a layer of blood [7]. In these stab-wound animals we noted the formation of a cystic cavity in the area where UEAs had been implanted that was similar in size and shape to those observed under chronically implanted electrode arrays [7]. These results suggest that the cystic cavity formation observed under multielectrode arrays is related to initial vascular injury, as opposed to being due to the continued presence of a foreign body.

Figure 2.4 shows the typical distribution of FBR biomarkers around a chronically implanted 4 x 4 UEA in rat cortex. Near the base of the device, a large amount of cortical tissue is missing, as outlined by GFAP+ hypertrophic astrocytes. Within this lesion cavity we observe enhanced labeling for IBA-1 and CD68, indicative of activated macrophages, as well as intense DAPI+ labeling of cell nuclei and IgG labeling of endogenous immunoglobulin. What is not observed within this lesion cavity is the presence of neurons or neuronal processes, indicating that tissue within these cavities would not be capable of generating recordable single-unit action potentials. As one moves deeper into the cortical tissue the size of this cavity tapers off, leading to the term "pyramidal shaped lesion cavity" reported by Nolta [7]. Near the tips of these devices a more classic FBR to implanted microelectrodes is observed, with CD68+ microglia adhering to the device surface, surrounded by GFAP+ hypertrophic astrocytes that wall off the surface of the device, as well as diminished neuronal density in the vicinity of such reactions.

A number of other studies in a variety of animal models have determined that when chronically implanted, multielectrode devices show evidence of device settling [1], [12], [13], [119]. Chronically implanted UEAs that maintain neural contact are found recessed into cortical surface depressions that match the shape and size of the electrode base. **Figure 2.5** shows a descriptive example from a study that evaluated the long-term tissue response to 10 x 10 UEAs implanted in feline cortex for durations of 34 - 76 weeks [120]. From above the surface it can be observed that the device has settled into the cortex, creating a flat imprint under the base. When sectioned along the sagittal plane and observed from the side, cortical tissue immediately under the device shows a granular appearance in contrast to the surrounding healthier tissue that has more solid white color, typically associated with myelinated tissue. Histological evaluation using horizontal sections shows that in upper cortical layers, toward the center of the device footprint a hypercellular tissue is evident, devoid of NeuN staining. Towards the tips of the device a more concerted and classic FBR is evident surrounding each of the electrode tips. This study shows similar features to those described in rodent cortex, where the tissue immediately adjacent to the base shows signs of decreased neural health and neuroinflammation and, when viewed from the cortical surface, shows localized areas of tissue loss.

2.3.5 Meningeal Encapsulation

Meningeal, or fibrotic, encapsulation of implanted high density penetrating microelectrode arrays has been noted in NHPs, felines and rodents [1], [7], [12]–[15], [121]. Consistently observed is a layer continuous with the meninges that spans underneath the base of the device and occupies the upper portion of the electrode shaft. In longer implant durations, this encapsulation tissue has been shown to entirely encapsulate the device, entirely excluding it from neuronal contact. This encapsulation response is unique to UEAs, as meningeal encapsulation has rarely been noted in response to single-shank microelectrode implants.

Rousche and Norman examined 12 UEAs chronically implanted in cats and noted that a progressive meningeal encapsulation under the base of the device and suspected that this tissue gradually lifted arrays from the cortex [12]. The thickness of the encapsulation tissue was correlated with the duration of implant, and in some cases entirely extracted the device from cortical contact at time points out to 20 months. A later study by this group attempted to layer Teflon sheets over the top of freely floating devices in effort to “prevent dural adhesions [13].” They reported that this technique was successful in reducing fibrotic tissue growth under the arrays, but in 2 of 15 cases this Teflon material moved away from the implant and dural encapsulation was observed. The Donoghue group adopted this technique to prevent dural adhesions in NHPs, but stopped using it as they noted an aggressive meningeal FBR to implanted Teflon and noted that encapsulation tissue was found on arrays both with and without a Teflon covering [1].

In 2013, Barrese *et al.* showed that meningeal encapsulation accounted for more than half of chronic failures of UEAs in NHPs [1]. They showed explanted arrays in NHPs out to 853 days that had been entirely encapsulated in tissue that appeared continuous with the dural and arachnoid layers. A later study by the same group of 8 UEAs implanted in NHPs reported that all UEAs investigated in the study had a variable amount of fibrotic encapsulation, and attributed this tissue to excluding the arrays from cortical contact [14]. These studies highlighted that, in NHPs, meningeal encapsulation is a primary cause for failure of devices to record in chronic settings.

When Nolta *et al.* examined the histological response to UEAs in rat cortex, those which had remained in place until the 12-week end point were encapsulated in fibrotic tissue [7]. In a study of UEAs implanted in the rat visual cortex, Cody *et al.* noted meningeal encapsulation of all 10 implants studies [15]. Half of these devices were entirely encapsulated by the 12-week study end-point, while the other half had fibrotic encapsulation spanning the base and the upper portion of electrode shafts. Even in rodents, where the meninges are markedly less substantial, fibrotic encapsulation of UEAs is regularly noted.

This encapsulation material has been investigated under light microscopy and indirect immunohistochemistry and has consistently been identified as meningeal in appearance. Using light microscopy, Rousche & Normann indicated that fibroblasts are spindle-shaped cells that were more closely packed towards the top of the encapsulation material, indicating an upward compressive force [12]. Barrese and colleagues showed that encapsulation tissue was devoid of neurons and astrocytes but rich in macrophages with immunohistochemistry [14]. Additionally, they noted the appearance of a subarachnoid space under the material and suggested that the encapsulation material was a combination of dural and arachnoid tissue. Nolta *et al.* examined this tissue with immunohistochemistry and found a high degree of CD68 immunolabeling, indicating the presence of activated macrophages. At present, we have identified that encapsulation material is devoid of neuronal cell types and likely is meningeal tissue in origin.

To summarize, multielectrode arrays experience a FBR far greater in extent and severity than that observed around smaller single-shank devices. Likely due to the highly vascularized nature of the cortex and the increased penetrating injury from multiple electrodes, cortical tissue loss occurs under the implant footprint of a UEA. These lesion cavities fill in with settling devices and meningeal origin tissue that also accumulates around the device base. Concurrent with this response we observe devices that tilt, rotate and move away from implantation target, explored further in the next section. Where electrode shafts remain in contact with neural tissue, a classical FBR is observed, which likely still challenges the ability of these devices to record from a healthy neuronal population. Combined, these factors highlight the need for strategies to improve the FBR to chronically implanted multielectrode arrays in the CNS.

2.4 Device Anchoring Strategies

One major hurdle facing the field of BCI is the propensity of high density recording devices to not record from a stable population of neurons over time [12], [16]–[18]. In a limited number of histological evaluations of chronically implanted UEAs, prevalence for device tilting, extraction and rotation has been noted when observing explanted devices. Current surgical approaches attempt to leave intracortical high density microelectrodes freely floating in the cortex, as anchoring to the skull has been shown to increase aspects of the FBR including astrogliosis and neuronal loss [21]. However, all these studies have been performed with single-shank microelectrodes, which are not subject to the complicating issues of meningeal encapsulation, lesion cavity formation or device movement that UEAs experience. This section will explore the available literature that has investigated the effects of anchoring on the FBR to CNS implants.

There is some ambiguity in the terminology that should first be addressed; a number of studies have used the terms "tethering" and "anchoring" somewhat interchangeably. For the sake of clarity, we will define an anchored device as one that is rigidly affixed to the skull, a tethered device will define any device with a trailing wire bundle that partially restricts movement of the device via the wire bundle. By these definitions a tethered device could still be unanchored, that is to say, freely floating on the skull but minimally restricted by a trailing wire-bundle that transmits signals to a headstage connector. At present, all recording microelectrodes are tethered, as wireless technology has only began to be manufactured small enough to allow wireless signal amplification and transmission to occur within a self-contained device [122]. In studies where the terminology "tethered" has been used to describe a scenario in which the device was anchored to the skull, the results will be presented using the correctly defined terminology.

2.4.1 Previous Studies of Device Anchoring

It is known that brain moves in relation to the skull, as cerebrospinal fluid (CSF) provides a fluid barrier that damps rotational energy transfer from the skull to the brain and allows for minor fluctuations in pressure due to respiration and vascular flow. In the field of neural recording, such movements are referred to as micromotion. In one attempt to quantify micromotion in the rat brain of anesthetized rats using microactuators, Muthuswamy and colleagues measured that the brain surface moves 2 – 25 μm due to pressure changes during respiration and 1 – 3 μm due to vascular pulsation [123]. In 2005, Lee and Belamkonda performed finite element studies of device-induced strain on the brain using these values [124]. They modeled Michigan electrodes in an elastic model of brain tissue in the ANSYS 3D finite element modeling software and simulated strain fields resultant from micromotion induced mechanical strain. They found that devices anchored to the skull would experience strain fields that extend over 100 μm from the electrode, which they point out is roughly the distance that GFAP+ astrocyte hypertrophy extends from the device interface.

In 2006, Subbaroyan and Kipke integrated this information and investigated the use of a flexible tethering bundle to reduce the modeled micromotion induced strain [125]. They performed finite element modeling and found that flexible interconnects made of polydimethylsiloxane reduced strain at the device interface by 2 orders of magnitude. They also performed *in vivo* studies with 3 Sprague Dawley rats to validate the modeling results. Immunohistochemical quantification showed that GFAP expression and neuronal loss were decreased with low-strain flexible interconnects. More recently, *in vitro* studies have shown that glial cells, in particular astrocytes and microglia, are active mechanosensors and respond to strain with reactive gliosis [126].

Following up on these studies, Biran, Martin and Tresco performed a robust analysis of the FBR to anchored and unanchored microelectrodes in rats to compare the response at 1, 2 and 4 weeks [21]. They reported increased macrophage activation and GFAP expression in anchored devices at all time points studied. This also was the first study to determine that microelectrodes with the highest level of macrophage activation had increased neuronal loss surrounding the devices. This study solidified the growing consensus that anchored devices suffered an enhanced FBR that likely hindered device function.

In 2011 Thelin *et al.* compared anchored and unanchored 50 and 200 μm diameter stainless steel probes implanted in the rat cortex for durations of 12 weeks [22]. It was noted that devices anchored to the skull had an enhanced FBR, indicated by upregulation of GFAP astrogliosis and microglial reactivity at the surface of anchored electrodes. Additionally, they noted oval-shaped lesions that extended in the rostral-caudal direction in anchored electrodes. They attributed these lesions to be resultant of either the enhanced FBR that exacerbated tissue loss, or as a result of micromotion induced tissue displacement. They justify this later hypothesis by incorrectly citing a later Muthuswamy article [127], saying that movements of the brain relative to the skull are enhanced in the anterior-posterior axis compared to the medial-axial in activities of daily life. (In fact, the paper reported that in *anesthetized* animals the brain moves 10 – 30 μm during breathing and 2 – 4 μm due to vascular pulsatility, confirming previously reported magnitudes of micromotion [127]). Regardless of speculated mechanism, this study added to the growing consensus that anchored microelectrodes have an enhanced FBR, and that brain movement relative to the skull is a cause for enhanced gliosis around chronically implanted microelectrodes.

In 2013 Karumbaiah *et al.* studied the FBR to a variety of microelectrode recording designs, of those they compared anchored and unanchored high density microwire arrays [23]. With 7 different electrodes compared at 2 time points, this study had far too many variables to perform a robust analysis, however the authors did report higher levels of GFAP around anchored microwire arrays compared to freely floating designs. Although reported details are minimal, this was the first study to compare the effects of anchoring on the FBR to a high density penetrating array.

In summary, a number of studies have investigated the FBR to anchored and unanchored microelectrodes, and all studies have shown that anchored devices have an enhanced FBR. While these studies have indicated that anchoring is not ideal, it remains largely unaddressed if such strategies hold true for high density penetrating arrays, where implantation associated injury is orders of magnitude greater. To date, the majority of high density microelectrode arrays have been implanted using a freely floating approach, where devices are left unanchored and loosely tethered by a trailing wire bundle. The next section will detail a number of studies that have reported UEA movement on a scale that limits recording capabilities.

2.4.2 Reports of Device Movement

Work in the 1990's conducted by the Normann group at U of U investigated the feasibility of UEAs as cortical stimulation and recording devices [121], [128], [129]. In 1998 Rousche and Normann published, at the time, the largest retrospective study of the chronic biocompatibility of UEA implanted in the feline cortex. In this study, 10 cats were implanted with 10 x 10 UEAs for durations of 2 to 20 months and recording performance was analyzed and compared with postsacrifice histological observations.

Around this same time, William Agnew's group at the Huntington Medical Research Institute was investigating the potential of high density microwire arrays in cats [16]. These devices had 7 penetrating iridium electrode shafts, 35 µm in diameter and 1.5 to 2 mm in length, all attached to a flat base with a trailing wire bundle. They observed time-dependent gradual changes in signal amplitude and attributed these changes to a slow migration of microelectrodes through neural tissue. At explant the devices were found settled into a cortical surface depression and it was determined that connective tissue growth over the array caused a gradual downward displacement of the array, eventually resulting in loss of resolvable SNRs.

In 2000 the Normann group attempted to improve the FBR to chronically implanted 5 x 5 and 10 x 10 UEAs implanted in feline cortex by preventing dural adhesion [13]. Devices were implanted underneath the dura and then a layer of Teflon was layered over the top of the device. It was expected that this technique would prevent the array adhering to the skull and reduce micromotion induced tissue damage. The array base did have less connective tissue encapsulation than the aforementioned study by Rousche and Normann [12]. However, these devices were also observed to settle into cortical surface depressions, resulting in devices shifting from original implantation target. This result may indicate that even in the absence of a meningeal encapsulation response, devices move from implantation target due to cortical tissue remodeling under the device base.

In 2005 the Donoghue group at Brown University investigated the reliability of freely floating UEAs implanted in NPH cortex [17]. While identifying that the primary cause of recording failure was failure of acrylic headstage and subsequent device removal, they also noted that neural waveform varied between, but not within days, suggesting a shifting population of recorded neurons over time. Histological analysis was not included in this study, but this became the first NPH study to confirm the previous reports of device migration in feline cortex. A later study in humans also observed recording signals that changed across recording sessions, indicating a shifting population of recorded neurons [18].

In 2013 the Donoghue group followed up with a retrospective evaluation of device failure mode, including data from 72 UEA implanted in NHP for periods of 0 to 5.75 years [1]. In a number of cases the device was heavily tilted from the original implantation trajectory, as shown in **Figure 2.6**.

In 2015 Nolta *et al.* described the FBR to rats chronically implanted with 4 x 4 UEAs, and also observed devices that were tilted at varied angles upon explant [7]. UEAs were implanted unanchored, with only a trailing wire bundle loosely tethering the caudal end of the device. Upon explant, 6 of 11 devices that failed due to the FBR had tilted to one side or were found in a more superficial location relative to implantation target, often with entire rows of electrodes visible from the cortical surface. This study again indicated that device movement was a primary failure mechanism of high density penetrating microelectrode arrays, adding to the growing number of animal studies indicating that the CNS FBR was a secondary concern to addressing device movement related issues.

In summary, the majority of histological studies of the FBR to UEAs have indicated that devices either settle into cortical surface depressions, change orientation, or become encapsulated in meningeal-origin tissue, resulting in recording from a shifting population of neurons over time. While it may seem reasonable to affix a device in place to prevent such movement, studies of device anchoring have indicated that the FBR is increased to anchored devices. No study to date has studied this particular failure mode of UEAs. In Chapter 4 we explore the question of how anchoring influences the FBR to chronically implanted UEAs in the rat cortex.

2.5 Neurovasculature

With limited capacity for energy storage, oxygen tension or ionic fluctuations, the brain's extracellular milieu must remain tightly regulated to ensure proper neural function. The human brain, while comprising roughly 2 % of total body weight consumes roughly 20 % of all oxygen and 15 - 25 % of all glucose produced in the human body [130]. This nutrient delivery is achieved by a system of macro and micro vessels that feed a dense system of capillaries, allowing every area of the brain to receive comprehensive regulation of ion balance, nutrient delivery, oxygen tension and metabolic waste removal. It has been estimated that there is roughly 20 m^2 of capillary surface area for nutrient exchange in the human brain, assembled from roughly 400 miles of capillary length [131]**.** This section will explore the structure and function of the neurovascular unit in both humans and rodents and the blood-brain barrier will be explored in detail.

2.5.1 Cortical Organization

Studies of the neurovasculature and its relation to neurons have shown that neural angioarchitecture is a highly organized structure that permeates all areas of the brain with incredibly high fidelity. Using two-photon microscopy and tissue clearing techniques in rodents, the Kleinfeld group at UCSD has shown that a given cubic millimeter of cortical brain volume has 0.88 ± 0.17 meters of vascular length [132]. Additionally, they showed that every neuronal nuclei lies within 15 μm of a capillary, displaying the abundance of vasculature in the cortex [132]. Other studies by the Duvernoy group in France have confirmed these statistics and added a few others, such as a vascular surface area to volume ratio of 11.74 mm^2/mm^3 and a vascular volume of 2.4 % to 3.0 % of cortical tissue volume [133]. Collectively these morphometric parameters give indication of the high degree of vascularization within the cortex.

Blood is fed to the brain from 4 major arteries: the left and right carotid and left and right vertebral arteries. These arteries join together at the Circle of Willis, a first step in providing redundancy to the cerebral circulation as occlusion of one of these arteries can be compensated by the 3 others. From here cerebral arteries branch off and provide circulation to distinct brain regions. Cortical blood supply is routed through the pial arteries (30 - 200 μm diameter) that travel on the surface of the brain in the subarachnoid space [134]. These surface arteries supply blood to descending arterioles (40 μm diameter primate, 11 μm in rodent) that plunge into the cortex [135], [136]. Cortical arterioles descend perpendicular to the cortical surface and branch off into a capillary network referred to as the capillary bed. At the capillary level (6 - 8 μm diameter in primate: 3.5 - 4 μm in rodent), nutrient exchange is achieved before blood enters into ascending venules that return blood to the surface of the brain [132], [133], [137]. These ascending venules coalesce into larger superficial veins, which empty into the dural venous sinuses, eventually draining to the jugular vein and emptying into the superior vena cava.

2.5.2 The BBB

All organisms with an intact CNS have a BBB that participates in the regulation of the CNS parenchyma by acting as a selective barrier for transport of molecules, proteins and cells from blood into the CNS parenchyma. The bulk of nutrient exchange in the CNS happens at the capillary level, as capillaries run an extensive network through the brain leaving no neuron greater than 15 μm from blood supply [132].

The innermost layer of the BBB is composed of brain endothelial cells (BECs), which form the inner lining of the capillary. These cells are adhered to each other with tight junctions and adherens junctions, which prevent the extravasation of larger solutes, proteins and polar molecules, creating the first line of defense against unwanted solute diffusion across the BBB [110]. Along these junctions a number of active and passive transport proteins allow selective passage of ions, amino acids, nutrients via carrier-mediated transport, ion transporters, active efflux and peptide transporters [138].

Immediately outside this layer of BECs is the basement membrane, an extracellular matrix layer that provides structural support for the vessel. Composed of extracellular matrix (ECM) proteins including fibronectin, laminin, chondroitin sulfate proteoglycans and collagen type IV, the basement membrane is rich in cellular attachment domains where endothelial cells, pericytes and astrocytes all bind, creating a zonal area where these cells can cross-talk and regulate vascular permeability [139]. The basement membrane also serves as a barrier to leukocyte migration, as this ECM must be degraded with matrix metalloproteases (MMPs) in order to allow passage of leukocytes from the blood stream into the brain parenchyma [140].

Embedded in and around the basement membrane are pericytes, who form close contact with BECs. Pericytes are found surrounding all vasculature, and to date, no distinct gene expression profile has been noted that differentiates brain-derived pericytes from those observed elsewhere in the body. However, the ratio of pericytes to endothelial cells in the brain is high, 1:3, compared with 1:100 in striated muscle [141]. Similar in function to vascular smooth muscle cells, pericytes are responsible for contractile forces that regulate blood flow through capillaries [141], [142]. Pericytes help facilitate nutrient transport from BECs by interacting with these cells at tight and adherins junctions [141].

Embedded outside of and in-between pericytes are numerous astrocyte end feet, which form a layer known as the glia limitans perivascularis. In this layer astrocytes extend long cellular processes from their locations in the parenchyma toward capillaries and communicate with pericytes and endothelial cells via secreted cytokines, ECM molecules (integrin signaling) and direct cell-to-cell coupling [143], [144]. *In vitro* studies have shown that a number of astrocyte-secreted components are capable of modulating endothelial cell permeability, and are also responsible for the differentiation of endothelial cells to BECs in the developing brain [145]. Responsible for CNS homeostasis, astrocytes are closely associated with the BBB and contribute to its function. Astrocytes have been shown to regulate brain water levels and electrolyte metabolism via astrocyte secreted growth factors that affect BEC function [143]. Indeed, cerebral blood flow is controlled at the capillary level by astrocytes to meet the specific metabolic demands of neurons via neurovascular coupling between neurons and vascular smooth muscle cells [146]. Astrocytes serve as the bridge between metabolic demands of neurons and the highly exclusive BBB; these cells are innate sensors of homeostatic needs and react by controlling cerebral blood flow and nutrient exchange, making astrocytes an important target when investigating the structure and function of the BBB.

Taken together, the complex interactions of BECs, pericytes, astrocytes and neurons create what has been called the neurovascular unit. This highly complex and dynamic interface between various cell types allows the BBB to function properly. While the triggers remain largely unknown and likely varied, all CNS neuroinflammatory disorders result in BBB dysregulation that allows passage of serum proteins, cytokines, and large molecules into the brain [138]. These components have known neurotoxic effects and contribute to the degenerating pathology observed in neuroinflammatory diseases like Alzheimer’s, Parkinson’s, muscular sclerosis (MS), ALS and dementia. As such, a functional understanding of how the BBB works and strategies to intervene during dysfunction will greatly enhance the ability of modern science to treat a broad range of disease pathologies.

2.5.3 Rat Versus Human Neurovasculature

Rat models are consistently used to study the FBR to materials implanted in the CNS, preferred for their availability, low cost and low status on the phylogenic tree. Additionally, rodents have shown to express a FBR that shares the hallmark signs of a CNS FBR, in particular activation of microglia, astrogliosis, neuronal loss and BBB dysfunction [90]. It also appears that cortical tissue organization is relatively conserved across mammalian species, resulting in a rodent cortex that is nearly as thick as human cortical tissue [147]. Of importance to our studies is a thorough understanding of differences in the cortical architecture between humans and rodents, so that insights generated can be rendered applicable to human patients as well (**Table 2.3**).

When observing cortical thickness of the 2 species it can be seen that the rodent cortex is 73 % the thickness of that measured in humans (1.83 mm and 2.5 mm, respectively). This is somewhat remarkable when considering that the weight of a rodent brain is only 0.2 % that of the human brain (2.6 g versus 1.176 kg, respectively) [148]. When discussing the evolution of the mammalian cortex, DeFelipe suggests that cortical thickness is preserved across many species due to similar functionality of the cortical column, however larger species like the primate have a much more ruffled cortex, which allows a much higher ratio of cortical volume [147]. It has been estimated that, in the human brain, the cerebral cortex makes up 82 % of the total brain volume [149]. This astounding preservation of cortical thickness highlights the similarities of cortical column organization between the 2 species, and suggests that the rat cortex maybe an acceptable test bed for the implantation of 1 mm long electrodes, which will extend into similar cortical layers in the rodent.

When looking at **Table 2.3** it is apparent that penetrating arteries are much larger in humans than rodents (40 μm versus 11 μm). In the primate brain the ratio of descending arteries to ascending venules is roughly 1.6:1, indicating a preference towards oxygen delivery. In the rodent this ratio is reversed (1:1.8 - 3) [26], [136], [137], [150]. These differences could have functional implications due to the fact that in humans more and larger descending arterioles would be ruptured by the implant of a device, while in rodents a larger relative number of smaller ascending venules would be ruptured. However, both species have similar numbers for vascular volume percentage (2.5 - 3 %), and recent evidence suggests that stroke formation is similar whether arteriole or venules are ruptured.

In a study of rodent microvasculature and the effect of stroke, Shih *et al.* utilized photothrombosis to occlude either arterioles or venules of sizes ranging from 10 - 100 μm in diameter and found that lesion formation and overall damage did not depend on vessel type occluded, but rather the flow rate of red blood cells through the vessel [26]. Given that in both humans and rodents total vascular volume is roughly 2.5 % of the total cortical volume, it could be inferred that the reversed ratios of arterioles to venules in rodents would not significantly alter the development of ischemic zones in response to penetrating injury.

2.6 CNS Insult and Reactive Gliosis

2.6.1 Focal Insult

CNS trauma is initiated in acute stroke or focal traumatic injury such as TBI or penetrating injuries like electrode implantation. Work over the past decades has used ischemia-reperfusion models of stroke, impact associated TBI and controlled cortical stab to investigate the dynamic multicellular responses to CNS injury. In all these experimental models neurovascular injury is sustained and results in the dynamic responses of both CNS and non CNS cell types to restore function and protect unaffected areas from deleterious inflammatory signals associated with tissue remodeling and repair. The end result of stroke, TBI and cortical stab is the formation of a nonneuronal lesion core, surrounded by a glial scar and a gradient of tapering reactive gliosis that is associated with decreased neuronal density [151].

2.6.2 Triphasic Response to Focal Insult

The CNS response to injury can be divided into 3 overlapping phases: (1) cell death and inflammation, (2) cell proliferation and (3) tissue remodeling [32]. **Figure 2.7** demonstrates the overlapping nature of these phases and serves as a generalized time-line for resolution of acute CNS trauma in the absence of persistent inflammatory stimuli as may be present in pathologies such as infection, neurodegenerative disorders or the FBR to implanted biomaterials.

Transmission electron microscopy (TEM) studies of middle cerebral artery occlusion (MCAO) have shown that in the 48 hours following ischemia, astrocytes retract their processes from vascular contact and MMPs degrade the basement membrane of the vascular wall [152]. In contrast, microglia have been shown to rapidly extend processes towards focal vascular insult caused by laser ablation [153]. *In vivo,* two-photon imaging of genetically labeled cells has shown that microglia react on the scale of second to minutes, retracting from a dynamic ramified morphology and extending processes towards damaged capillaries, eventually sealing off the capillary leak.

Ischemic injury causes hypoxia to the neurovascular unit, resulting in failure of the BBB, which allows the passage of serum proteins into the normally protected CNS parenchyma [154]. This extravasation results in hemostatic mechanisms including platelet aggregation, complement accumulation and the coagulation cascade that form a primary hemostatic plug [87]. These components and serum components are neurotoxic, and coupled with hypoxic stress, result in necrosis and apoptosis of surrounding neurons [155].

Locally generated cytokine signals, derived from cellular necrosis and the hemostatic plug, recruit monocytes to the injury site. Peak concentrations are typically found 48 hours after insult [156], [157]. Bone marrow derived macrophages are directed to the injury site via MCP-1 signaling, where they show elevating levels in the first 72 hours following controlled cortical impact [158]. There is also evidence that resident perivascular microglia contribute to BBB breakdown by phagocytosis of brain endothelial cells as soon as 24 hours after injury [115]. Due to a lack of specific antibody markers, the distinct functional roles of brain resident microglia and bone-marrow derived macrophages remain elusive. Both cells label with the pan-macrophage marker, IBA-1, and are responsible for phagocytizing apoptotic cells and molecular debris and removing this damaged material [159]. This initial phase of wound recovery is characterized by acute cell death of parenchymal neurons and the recruitment of nonneuronal immune cells that actively phagocytize and clear dead cells and damaged tissue.

The second phase of this response, typically occurring days 2 - 10 post injury, is the cellular proliferation phase where gliotic and fibrotic barriers are established. Neovascularization begins to resupply affected areas with blood, but an incomplete BBB allows the extravasation of serum proteins into the CNS parenchyma [151]. Macrophages remain present at the site of inflammation, with phenotypic shifting of macrophages toward neurotoxic inflammatory activation states increasing with a peak at 3 days post injury [95]. The lesion core is rich in soluble factors such as macrophage-derived inflammatory cytokines and serum proteins resultant from disrupted BBB; these signals have deleterious effects on surrounding neural tissue until lesion core boundaries are established. A complex interplay of fibroblasts and astrocytes deposit ECM molecules that establish a basal lamina-like barrier that separates lesion core from surrounding CNS parenchyma [30], [160], [161]. BBB-disrupted area is confined during this phase as reactive astrocytes enclose the affected area to create a barrier composed of newly proliferated, elongated astrocytes [31], [162]. Genetic knock-out models have shown that astrocyte involvement is necessary to “corral” the inflammation and successfully wall off inflamed lesion core from surrounding neuronal tissue [151].

In the third phase of the CNS wound response, tissue-remodeling mechanisms stabilize as permanent gliotic and fibrotic scars form. BBB integrity is restored and a stable border between meningeal and glial cells is established. Within the lesion core nonneuronal cells types such as fibroblasts, mesenchymal stem cells, endothelial cells, pericytes and macrophages interact to form a fibrotic scar. This scar tissue is associated with deposition of ECM components, including collagens and proteoglycans that have inhibitory effects on neuronal regeneration [30], [160]. Eventually tissue remodeling in this zone stabilizes, denoted by the absence of activated macrophages in the lesion core.

Surrounding the nonneuronal fibrotic scar, a glial scar comprised of newly proliferated, elongated astrocytes forms a compact sheath that surrounds the lesion core. In the absence of persistent inflammatory stimuli this response typically stabilizes by 14-days post injury [162]. The gliotic scar contains astrocyte-secreted proteoglycans that limit neuronal growth or axonal extension into the lesion core [163]. Immediately surrounding the area of glial scarring there is a perilesion perimeter that shows a gradient of reactive gliosis and decreased neuronal density that eventually transitions into healthy neuronal tissue [32], [151], [162]. This perilesion perimeter zone is an area of intensive tissue remodeling where newly recruited neurons are capable of synapse formation and axonal sprouting [164], [165]. In these perilesion areas, reactive microglia are found, and it has been shown that their phenotype can be responsible for neurotoxicity or functional tissue regeneration [95]. The goal of interventional strategies is to spare neurons in this perilesion perimeter, where reactive gliosis is observed, and likely effects neuronal function.

The end result of focal cerebral insult is the generation of a nonneuronal lesion in the affected area. This lesion is filled with meningeal tissue and, in the adult, does not regenerate, manifesting as lesion cavities that are present for lifetime.

The time course for resolution of inflammation in the CNS is heavily dependent on the severity of injury, proper function of immune responses and clearance of inflammatory stimuli. Neurodegenerative disorders are classified by sustained inflammatory stimuli such as the presence of Aβ in Alzheimer's, or the continued death of dopanergic neurons in the substantia niagra of Parkinson's patients. Such sustained inflammatory stimuli create a sustained inflammatory responses that reopen the BBB and restart the process of cell death and inflammation. Neurodegenerative pathologies are defined by the inability to resolve CNS inflammation and as such are complicated by the formation of nonneural lesion cores, decreasing brain volume and loss of cognitive and motor functions.

The FBR to implanted biomaterials shares this neurodegenerative issue of sustained inflammatory stimuli, originating form device-adherent macrophages undergoing frustrated phagocytosis [3]. Similar to stroke-like lesion cavities, devices are surrounded by reactive gliosis and a tapering gradient of neuronal loss extending from the device interface [166]. Recent data has shown that microelectrode implantation is correlated with progressive fine motor skill decline in rodents [167], providing a cautionary example of potential drawbacks associated with chronic microelectrode implantation for therapeutic potential.

2.7 The Meningeal Response to Injury

2.7.1 Structure of the Meninges

The meninges are composed of three primary layers that encapsulate CNS organs (i.e., brain and spinal cord), form a protective barrier against mechanical forces and provide blood and cerebrospinal fluid (CSF) supply to the skull and brain.

The outermost layer, the dura matter, surrounds the brain and spinal cord and is a collagen rich layer that is notably thick and fibrous. This layer does not conform to the rippled surface of the brain, but rather encases the entire organ, more like a bag than a surface layer. This layer is mostly composed of collagen with sparse and well spread fibroblasts located throughout the layer [168]. These fibroblasts are very flat and spread, and do not form many cell-to-cell junctions. The dura matter does not have an extensive system of tight-junctions, as would be seen in exclusive barriers like the BBB, indicating that this layer does not perform barrier functions [168]. This layer is so dense that most microelectrode implantations, particularly those with high density penetrating arrays, must first resect the dura to gain access to the underlying, softer, brain tissue [169].

Below the dura matter lays the arachnoid matter. Given its name due to the spider-like appearance of this layer, the arachnoid is composed of an intertangled web of collagen that can absorb forces, and thus dampen mechanical trauma to the brain. Additionally the arachnoid hosts a 2-3 cell thick layer of fibroblasts that form a series of tight-junctions that limit the exchange of solutes across this membrane [168]. Studies of drug diffusion have shown that the arachnoid layer is the major constitutive barrier of the meninges, as this layer shows the slowest diffusion of drug and anesthetic molecules [170].

In larger mammals such as the primate, a subdural space exists between the dura matter and the arachnoid layer; however in smaller mammals, like the rodent, the dura and arachnoid layers are closely associated and a subdural space does not exist. Typical resection of the dura matter also pulls the arachnoid layer with it in rodents. In primates, the arachnoid layer is left intact and electrodes are implanted through this subdural space. These differences may be responsible for meningeal encapsulation being reported more frequently in primates than in rodents.

Under the arachnoid layer is the subarachnoid space, which houses the brain's cisterns of CSF as well as a mix of both arteries and veins that provide blood circulation to the brain. CSF is circulated through this layer where it serves the function of fluidly suspending the brain to protect it from impacts and swelling. The CSF also serves part in the brain's lymphatic drainage and homeostatic maintenance systems.

The innermost layer of the meninges is the pia matter, a thin layer that conforms to the surface of the brain and encases arterial vasculature as it penetrates into the brain [171]. The pia matter itself is composed of flattened fibroblasts and sparse collagen fibrils and is impermeable to fluid. This allows the pia to act as a barrier between the CSF and underlying brain tissue. On the inner side of the pia matter, astrocyte end-feet form a glial limitans, similar to that observed around pericytes of the BBB, and help establish selective permeability of the pia layer.

In concert, the layers of the meninges form a protective barrier that shields the CNS from mechanical forces, provides a barrier against cell, protein and solute diffusion, and facilitates circulation to the brain and skull.

2.7.2 Response to Injury

In response to injury, the meningeal layer regrows thicker, and often deeper in the cortex than the original layer, and is referred to as a fibrotic scar [161]. Fibrotic scarring, and associated meningeal cell types, are responsible for ECM, cytokine and ligand signals that inhibit neuronal regeneration and diminish the ability for functional regeneration of scarred CNS tissue [30].

After experimental cortical stab with a knife, Maxwell *et al.* observed that a fibrotic lesion forms, as denoted by the presence of fibroblasts and collagen along the penetrating tract [172]. During the acute phase of stab injury (1 - 3 days) BBB disruption, neuronal death, reactive gliosis and infiltration of hematogenous cells is observed. By 4 days post injury this lesion fills with a large number of fibroblasts, macrophages and astrocytes. Between 8 and 14 days after injury these cells begin to show apparent organization, with the formation of a basal lamina denoting the edges of a lesion border zone [173]. Astrocytes form a glial limitans along this basal lamina and interact with meningeal cells types to reestablish the intraparenchymal border [174]. Within the lesion fibroblasts travel from the pia matter down into the lesion and line the edges of the fibrotic scar [172]. This fibrotic scar presents a definitive barrier that is not permissive to axonal regeneration, and excludes neural network recovery across the injured zone.

Interestingly, neonatal rats do not have fibrotic scarring of the CNS and recover from experimental cortical stab without the collagenous and fibrotic response that is observed in adult rats [31]. Fibrotic scarring can be altered in adult rats by varying the availability of transforming growth factor beta one (TGF-β1). Logan *et al.* showed that TGF-β1 was integral in fibroblast signaling that leads to dense fibrotic growth, and that this fibrotic response could be attenuated with TGF-β1 antagonists [175]. Additionally, blockers of collagen synthesis have been shown to reduce the presence of the fibrotic scar and facilitate axonal regrowth across fibrotic lesions [104], [176]. Collectively, these results suggest that attenuating fibrosis in response to CNS injury can facilitate functional regeneration after injury.

The meninges also show diffuse enhancement, or thickening, in response to a number of inflammatory stimuli. Diffuse dural enhancement is a term that stems from the field of radiology, where thickness changes in the dura can be observed by magnetic resonance [177]. It has been observed that dural thickening happens in dogs and cats with a variety of CNS diseases, including meningitis and ear infections [178]. A number of other studies have demonstrated dural thickening in response to direct injury, such as that obtained from dural puncture [179], craniotomy [180], and ventricular shunting [181]. The studies indicate that the meninges is a dynamic layer that regrows thicker in response to rupture, injury or underlying inflammation.

In summary, after penetrating injury cortical tissue wound healing is augmented by a meningeal response that initiates primary wound closure, eventually resulting in a nonneuronal lesion core. In the case of high density penetrating microelectrode array implantation, the meninges span underneath the base of the device and create a continuous fibrotic scar that physically separates the base of the array from the underlying cortical tissue. The fibrotic encapsulation response has been a suggested cause for variable and declining performance observed in chronically implanted UEAs [1], [14]. As such, strategies that could decrease the thickness of the fibrotic scar, better integrate the UEAs with this tissue, or stabilize device migration could potentially benefit the goal of long-term consistent neural recording. Chapter 3 will explore how anchoring strategies can influence the meningeal and cortical tissue FBR to implanted penetrating arrays.

2.8 ECM to Influence CNS Wound Healing

ECM-based bioscaffolds have been used to facilitate functional and constructive tissue remodeling in a number of soft tissues [182]. In some cases, ECM has been used as a surface adsorbed device coating to facilitate wound healing and reduce fibrosis surrounding chronically implanted medical devices, such as surgical meshes [183], [184]. In the central nervous system, ECM has been used far less extensively to influence wound healing or the FBR. This section will detail available reports of ECM-based wound repair strategies and additionally highlight the limited number of publications that have indicated ECM as a surface adsorbed device coating for chronically implanted microelectrodes.

2.8.1 ECM to Treat Focal Cerebral Insult

In the last decade a number of promising studies have indicated that ECM can be used as an injectable hydrogel to attenuate CNS damage sustained from TBI and stroke. As described previously, the end result of such focal cerebral insults is the formation of a lesion cavity that is unpermissive to neuronal regeneration. Regenerative strategies have aimed at reducing lesion size, facilitating axonal regeneration across lesions and decreasing astrogliosis and microglial reactivity within the lesion border zone.

Hyaluronic acid is a glycosaminoglycan component of ECM that has been used extensively in wound repair and skin healing due to its hydrogel characteristics and relatively inert nature. Hyaluronic acid hydrogels have been supplemented with the ECM protein laminin or ECM-based amino acid sequences like RGD and IKVAV, to be used as an injectable hydrogel to stabilize wound healing following TBI in rodents [185]–[187]. In all three of these reports, ECM-hydrogel treated animals showed increased axonal infiltration into lesion cores, increased presence of endogenous glial cells within the lesion core and reduction of glial scarring surrounding lesion cavities. Compared to unmodified hyaluronic acid hydrogels, the addition of laminin or RGD increased the positive properties of hydrogels compared to unmodified hydrogels, indicating that bioactive signaling was responsible for the observed improvements in tissue response.

Another ECM-based hydrogel that has received significant attention is ECM derived by decellularization of porcine urinary bladder wall. In a first *in vivo* CNS study, Wei *et al.* showed that urinary bladder ECM can attenuate lesion formation following stroke and decrease the area of demyelination compared to untreated or saline injected animals [187]. Following up on these studies, Ghuman *et al.* characterized the cell types recruited by urinary bladder ECM and showed that increasing ECM concentrations in hydrogels resulted in enhanced cellular recruitment within lesion cores and reduced the percentage of activated macrophages within the lesion core at 24 hours post injury [188]. When investigated at 13 weeks, it was reported that ECM-treated animals had reduced lesion volumes, however no difference was noted in astrogliosis or behavioral tests [35]. While not markedly improving the overall response following stroke, these studies suggested that ECM did not exacerbate any metrics of neuroinflammation and may possibly serve as a hydrogel to reduce lesion size and encourage glial cell infiltration.

Recently, Wu *et al.* used porcine brain-derived ECM to attenuate lesion formation following controlled cortical impact (a form of TBI) in rats [36]. Compared to

PBS treated control animals, those injected with ECM not only had reduced lesion formation, but also had decreased biomarkers for astrogliosis and microglial reactivity and performed better in behavioral tests. This was the first study to date using an ECM hydrogel to show that markers of neuroinflammation were decreased following treatment and additionally the only study to show functional recovery with behavioral tests. These exciting results indicated that using CNS-derived ECM had additional benefits that had not been observed when using hyaluronic acid or urinary bladder-derived ECMs. Indeed, a number of studies in various other organs have shown that tissue-specific ECM is preferable for functional wound healing by directing cellular phenotypes towards tissue-specific roles [189]–[192].

Collectively these studies have indicated that ECM is a relatively biocompatible hydrogel when used to attenuate lesion formation following focal cerebral insult in rodents. All reports to date have indicated that ECM does not negatively affect wound healing and has some effect at reducing lesion size following injury. While ECM has been speculated to direct wound healing by altering macrophage phenotype, only brain-derived ECM has shown the ability to modulate macrophage activation state in the brain [36]. Additionally, brain-derived ECM has shown improved behavioral outcomes, and decreased astrogliosis, indicating that tissue source is likely an important consideration when selecting ECM for wound healing in the CNS.

2.8.2 ECM as a Device Coating for Microelectrodes

To date, very limited studies have reported on the use of ECM as a surface adsorbed device coating for chronically implanted microelectrodes. All of these studies have been conducted in the rodent and much smaller microelectrodes where implantation associated injury and device surface area are significantly decreased compared to high density devices like the UEA. It remains unclear how these approaches would translate to clinically utilized, high density designs, where implantation associated injury, vascular rupture and hemorrhage are notably increased compared to the smaller research electrodes used in these studies.

In 2006, He *et al.* reported that a nanoscale laminin coating on the surface of a silicon microelectrode was capable of attenuating the FBR [193]. They reported that 4 weeks after implantation laminin coated devices had reduced macrophage activation and astrogliosis compared to uncoated, control devices. Additionally, they reported that at 1 day following injury ECM-coated probes had increased activated microglia near the device surface, indicating that ECM likely affected the immediate cellular response, leading to the downstream reduction of persistent neuroinflammation at the device interface.

In 2010, Lind *et al.* investigated the use of gelatin as a device coating to increase the insertion stiffness of flexible microelectrodes [38]. Dehydrated bovine gelatin, a denatured form of collagen, provided a structural support to insert electrodes and then quickly hydrated to become a low modulus material. This study did not perform any quantitative comparison to uncoated electrodes, but did report that bovine gelatin did not significantly exacerbate the FBR to coated electrodes.

In 2015, Shen and colleagues investigated micromachining techniques to fabricate an electrode out of bovine collagen and Matrigel™, an ECM derived from cultured brain tumor cells. Compared to silicone coated electrodes at 16 weeks postimplant, the ECM-based electrodes showed a significant decrease in astrogliosis surrounding the implanted device. This study speculated that the reduction in the FBR was due to reducing the amount of unnatural materials in the brain and also due to the decreased stiffness of ECM-based electrodes.

This year, our group published on findings of single-shank microelectrodes coated with either astrocyte-derived ECM or Avitene™, a bovine collagen ECM product [40]. Electrodes were dip coated with either ECM component and compared to control cohorts with no device coating at one week and 12 weeks post implant. In the Avitene™ coated cohort, all compared FBR biomarkers were similar except IgG, a marker of neuroinflammation, which was increased in the Avitene™ coated cohort at 8 weeks. When astrocyte ECM was compared to uncoated control devices, a reduction in astrogliosis was noted surrounding astrocyte ECM coated devices at chronic time points. Compared at 1 week, neither device coating significantly affected FBR biomarkers, but a significant increase in DAPI+ cells was noted around both types of device coating, indicating that ECM did in fact influence early phases of the wound healing response (data not published). *In vitro* assays showed that both ECMs were capable of accelerating hemostasis in rat blood, but only astrocyte ECM was capable of modulating macrophage activation state, suggesting that immunomodulation was a possible mechanism of action for the differences observed.

In regard to high density penetrating devices, no study to date has investigated the use of ECM-based device coating to limit the FBR. As has been described in this chapter, the UEA experiences a FBR far greater in extent and severity compared to single-shank device. The major differences are issues of lesion cavity formation, fibrotic encapsulation and device movement, which are rarely reported in response to single microelectrodes. With the UEA it has been reported that implantation of the high density penetrating device results in significant areas of hemorrhage and this implantation-associated damage results in lesion cavity formation under the base of implanted or even just briefly stabbed devices [7], [10]. As such, one goal of this dissertation is to investigate if limiting implantation-associated hemorrhage can lead to improvements in device outcome. For these studies we intend to use a strongly hemostatic ECM, ideally one with a proven safety and efficacy record, so that results could be rapidly translated to ongoing clinical trials. Collagen is the most abundant ECM in the body and forms the structural backbone of nearly all isolated ECMs. Additionally, collagen is a natural inducer of hemostasis and readily available as a FDA-approved hemostatic agent. Chapter 4 will explore a variety of other ECM-based device coating options, while Chapter 5 will focus on investigating if a FDA-approved ECM can limit tissue loss and reduce the FBR surrounding UEAs in the rat. Investigations of ECM as a device coating for microelectrodes have shown potential to reduce the FBR around single-shank devices, whether such improvements are translatable to high density devices remains unknown.

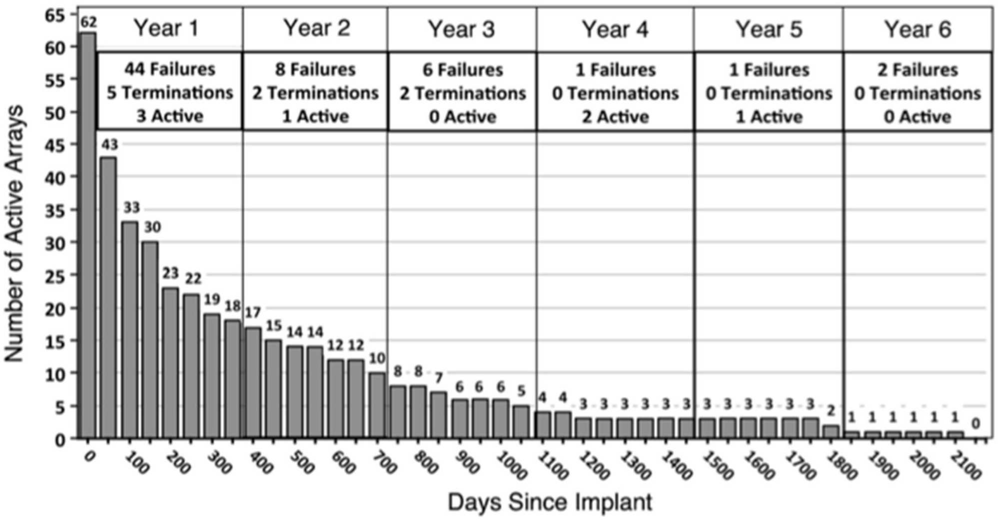

Figure 2.1 Failure mode analysis of UEAs in NHPs. In the largest retrospective study to date, the Donoghue Group at Brown University analyzed the time to failure for 78 UEAs implanted in NHPs. All array durations are aligned to time of implantation. Each bar represents 50 days further into the study duration, with the y-axis representing the number of functional arrays at the end of that period. Reproduced from [1] with permission from Elsevier Science and Technology Journals.

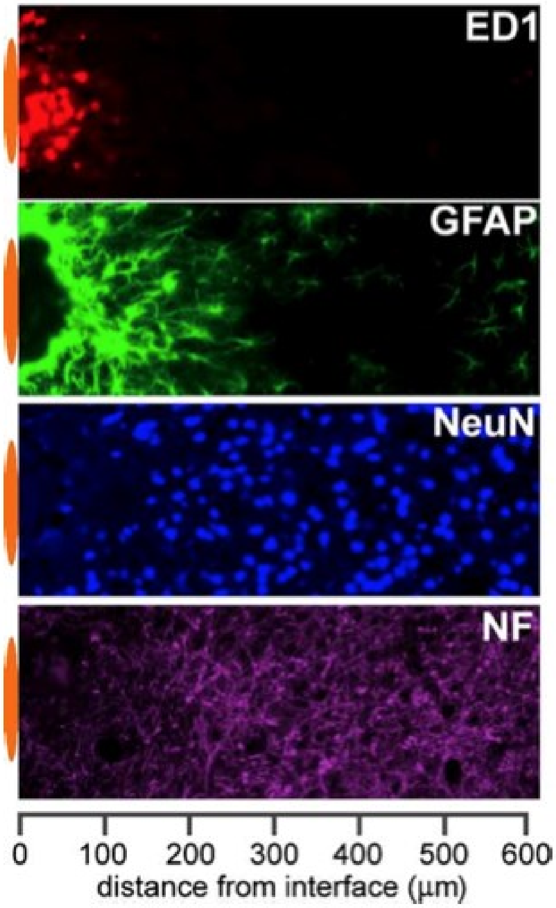

Figure 2.2 Hallmark signs of FBR to a single-shank microelectrode: Representative images collected from two adjacent sections of an animal with a 4-week microelectrode implant illustrate the general appearance of the foreign body response characterized by minimally overlapping inflammatory (ED1) and astrocytic (GFAP) phenotypes adjacent to the implant interface. The area of inflammation and intense astrocyte reactivity contains a reduced number of NeuN+ neuronal bodies and a loss of neurofilament (NF) density. The position of the microelectrode is illustrated by the orange oval (drawn to scale) at the left of each image. Images were captured in grayscale and pseudocolored for illustration. Figure and caption reproduced from [3] with permission from Elsevier Science and Technology Journals.

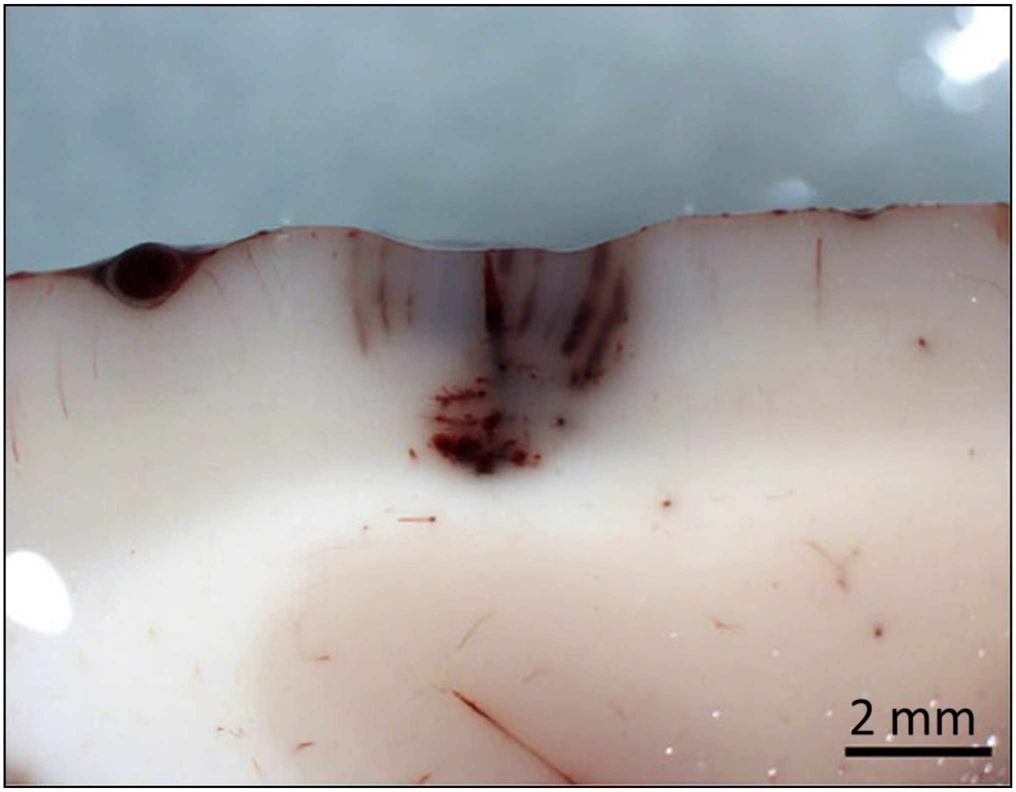

Figure 2.3 Acute petechial hemmorhage under UEA. A side-profile view of human cortical tissue after brief implantation of a 10 x 10 UEA. Evidence of bleeding is noted along electrode tracts as well as the formation of a petechial hemorrhage under the implanted device. Reproduced from [11] Permission for reprint assumed under Creative Commons Attribution License (CC-BY).

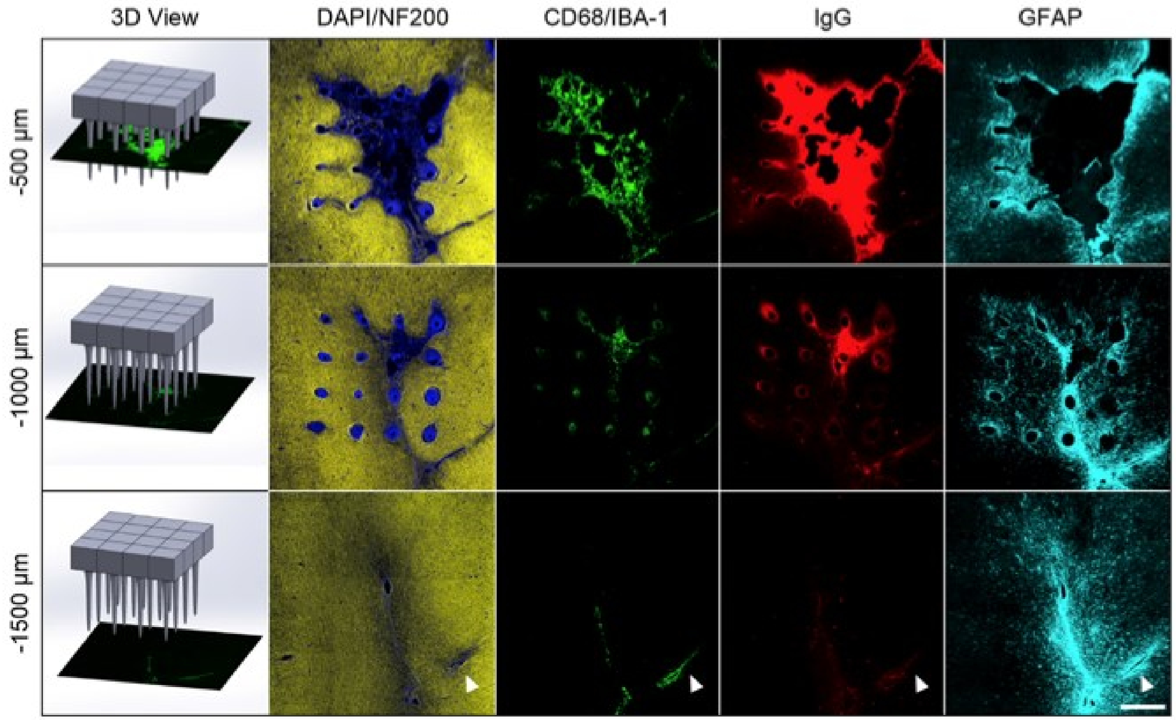

Figure 2.4 Typical distribution of FBR biomarkers around UEA in rat cortex. Cell nuclei (DAPI, blue), axons (NF200, yellow), activated macrophages (CD68/IBA-1 colocalization, green), BBB leakage (IgG, red) and astrocyte cytoskeleton (GFAP, cyan). Sections from three different depths are shown; 3D view illustrates approximate position of sections relative to UEA. Lacy, hypercellular, CD68+, IBA-1+, IgG+, NF200- areas of damaged neural tissue covered a large portion of the UEA footprint in superficial cortex (-500 µm), while microelectrodes not near tissue loss areas had an FBR typical of single-shank electrodes. In deeper cortex, the tissue loss area was smaller. Arrowheads indicate a region of increased CD68, IgG and GFAP immunoreactivity and decreased NF200 immunoreactivity associated with a large blood vessel. Scale bar 500 µm. Figure and caption reproduced from [7] with permission from Elsevier Science and Technology Journals.

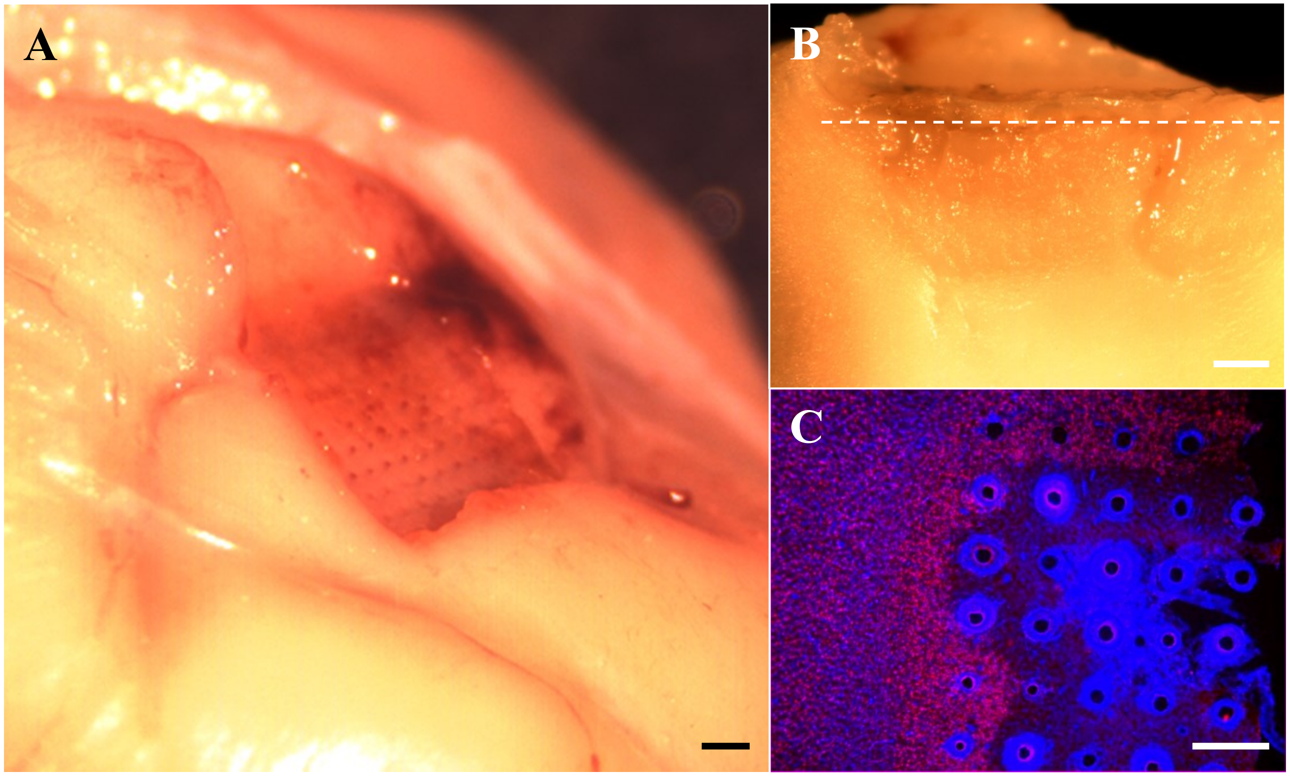

Figure 2.5 FBR to 10 x 10 UEA in a cat for 511 days. A) Gross view of the surface of the cortex showing a visible depression under the UEA. Scale bar 1 mm. B) The implant site was cut vertically and is shown in cross section. Note that cortical tissue immediately adjacent to the base of the UEA has a granular appearance, in contrast to healthier looking tissue deeper in cortex. Scale bar 500 µm. C) 30 µm horizontal section at the depth indicated by the dotted line in B, stained for NeuN (red) and DAPI (blue). Note the hypercellularity around electrode tracts and the lack of NeuN labeling towards the center electrodes. Scale bar 500 µm.

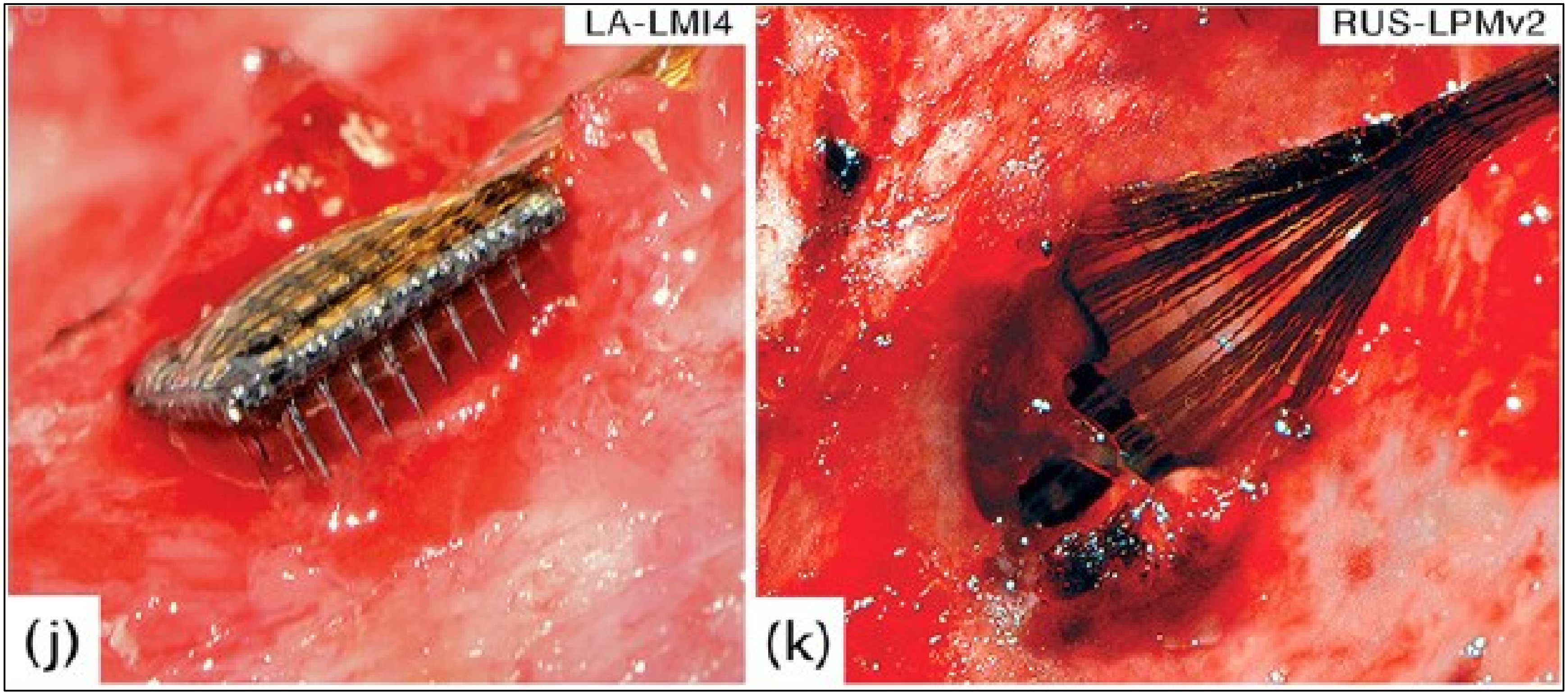

Figure 2.6 Explanted UEAs show changes in orientation. J) Array LA-LMI4 was implanted for 639 days in a NPH motor cortex; upon dissection the device was observed to have a row of electrodes entirely separated from cortical contact. K) Array RUS-LPMv2 was implanted for 994 days in a NHP and, at explant, showed significant changes from original device orientation, with the front of the device tilted deeper into the cortex. Figure reproduced from [14] with permission from Elsevier Science and Technology Journals.

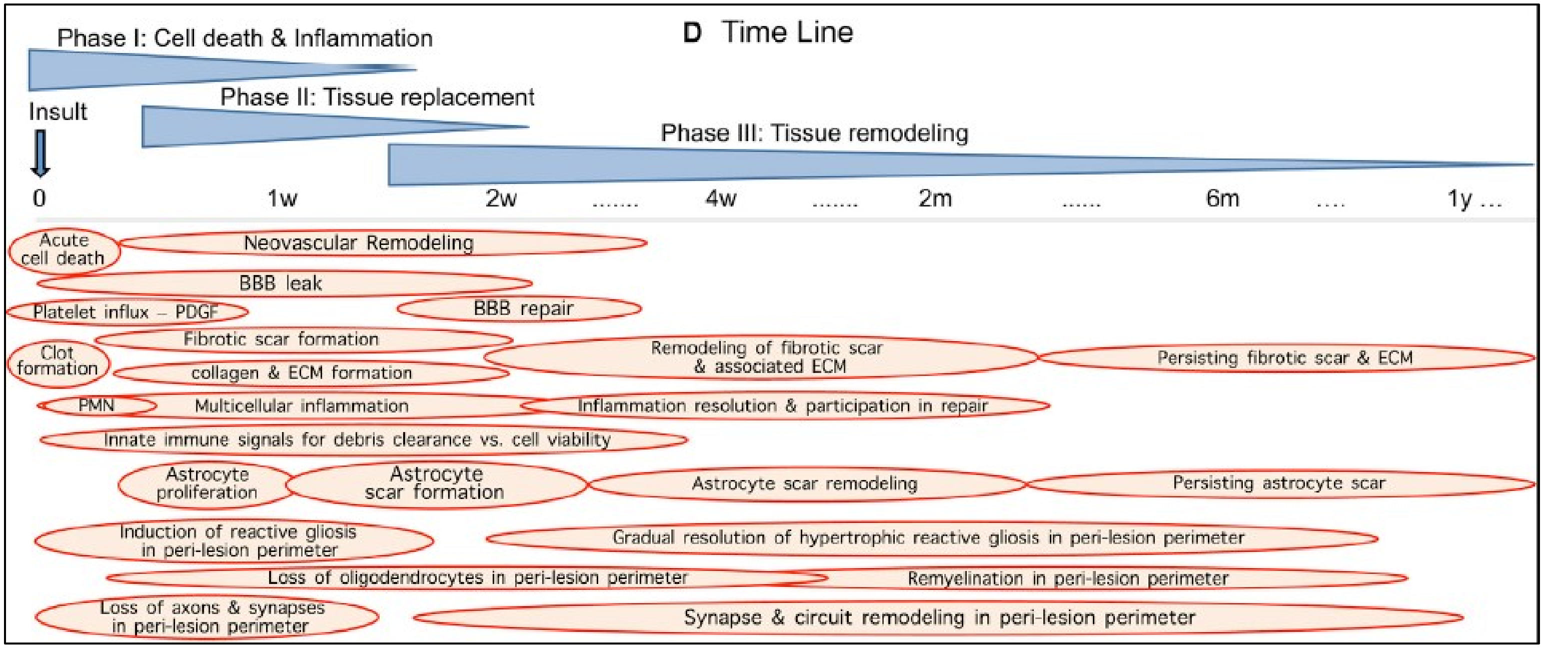

Figure 2.7 Tri-phasic response to focal cerebral insult. Immediately after focal cerebral insult, such as implantation of a high density penetrating array, cellular responses react to restore homeostasis. This chart shows the overlapping nature of the multicellular response and acts as a generalized time-line for the resolution of CNS trauma in the absence of persistent inflammatory stimuli as may be present in neurodegenerative disorders or the FBR to implanted biomaterials. PDGF - platelet derived growth factor, PMN - polymorphonuclear leukocyte. Figure reproduced from [32], with permission from Elsevier Science and Technology Journals.

Table 2.1 History of the FBR to Implanted Microelectrodes.

This table details the important scientific contributions that have built our understanding of the foreign body response (FBR) to chronically implanted microelectrodes. Each row details one seminal work and highlights the electrode type(s) studied, implant duration and animal model, as well as the important scientific contribution of each work and potential caveats

Year	Author	Model	Implant Duration	Implant Type	Scientific Contribution	Caveats
1957	Collias & Manuelidas[9]	Cat	1,3, 7, 15 days 1,2,4 & 6 months	Enameled Stainless Steel 127 µm microwire	Insertion leads to Hemmorhage Hypertrophic Astrocytes ensheathe reaction FBGC noted at later time-points Reaction stabilized > 1 month	Only 2 animals per time point studied Multiple side-by-side implants
1970	Dymond[194]	Cat	2 month	Chrome-nickel Platinum Stainless Steel Silver Boron 180-500 µm microwires	Implant material makes a difference in reaction Stab wounds create similar reaction to “non-toxic” implants Silver is a ‘toxic’ implant material	Variable diameter microwires (180-500 µm) create different damage profiles and make changes hard to discern
1976	Schultz[102]	Cat	26-328 days	Insulated Stainless Steel 250 µm microwires	Observed reduction in synapses around chronic implant Used SEM to identify FBGCs at device interface Showed astrocyte accumulation near surface	Implanted through meninges
1978	Stensaas[105]	Rabbit Rat	50-723 days	27 different materials	Variable (asymmetric) reaction Increased vascularity around implants Reactive astrocytosis increased around ‘toxic’ implants First quantitative approach First to report a connective tissue capsule around ‘toxic’ materials	

Table 2.1 Continued.

Year	Author	Model	Implant Duration	Implant Type	Scientific Contribution	Caveats
1984	Babb[195]	Rat	11, 36, & 65 days	Copper Silver Steel Nichrome Polyimide Epoxylite 200-950 µm microwires	Depletion of neurons surrounding implant First study to identify active phagocytosis at biotic-abiotic interface Phagocytosis stabilizes over time with 'nontoxic' metal implants	Compared various metals, but of differing diameters (200-950µm) 6 implants per animal
1992	Edell	Rabbit	6 month	Silicone multi-electrode arrays (1x10) 40x60 µm shafts	First silicon probe study Tip shape (round vs sharp) affects FBR with rounded tips causing less damage Took good care to implant axially aligned shafts First study of FBR to silicon microelectrodes First to identify effects of micromotion First quantitative study to identify neuronal loss as a function of distance from electrode shaft (termed "kill zone")	
1993	Schmidt[121]	Cat	24 hours, 6 months	Polyimide coated and bare silicone UEAs 10 x 10	First analysis of Utah Electrode Array Capsule thicker at base of UEA Although only modestly mentioned, first to indicate edema and hemorrhage surrounding multielectrode implant	Propensity towards bias as PI is device inventor No quantitative analysis
1994	Grill[196]	Cat	82-156 days	Expoy and silicone (rubber) arrays (1x4) 500 µm shafts	Electrical resistivity increases with duration of implant During first 14 days a large drop in resistance occurs (due to fluid accumulation) followed by a steady increase in resistance dependent on encapsulation thickness	No early histology to confirm "fluid accumulation"
1998	Rousche and Normann[12]	Cat	2-13 months	Polyimide coated silicone UEAs 10 x 10	Showed decline in functional arrays over time First to note fibrous encapsulation of device base	

Table 2.1 Continued.

Year	Author	Model	Implant Duration	Implant Type	Scientific Contribution	Caveats
1999	Turner[101]	Rat	2, 4, 6 & 12 weeks	Silicon single-shank electrodes 200x130 µm shaft	First study to utilize Immunohistochemistry (GFAP) Identify 2- weeks as a critical shift from initial injury response to capsule development Astrocytes migrate towards electrode	No quantitative data and relatively small n (3 for most time points)
2003	Szarowski[92]	Rat	24 hours, 1, 2, 4, 6 & 12 weeks	Silicon single-shank electrodes 200x130 µm 100x100 µm 120x15 µm shafts	IHC label for ED-1 showed reactive microglia at surface of device Response stabilizes after 6 weeks, but still includes activated microglia and astrocytes at 12 weeks	No quantitative assessment Only 3 electrode types used to postulate that size, geometry and roughness are all unimportant factors
2005	Biran[3]	Rat	2 & 4 weeks	Silicon single-shank electrodes 120x15 µm shafts	First quantitative IHC study Minimal astrocyte and microglia response to stab-wound (ie. foreign body is responsible for observed response) Cells adhered to implant are ED-1+ and secrete TNF-α and MCP-1	No chronic (8+ weeks) time point studied
2007	Biran[21]	Rat	1-4 weeks	Silicon single-shank electrodes 120x15 µm shafts	Devices tethered to the brain elicit more GFAP & ED-1 reactivity and reduction of NF160 and NeuN compared to freely floating electrodes	Untethered electrodes placed by hand, while tethered placed stereotaxically No control for head stage components
2010	Winslow[106]	Rat	2, 4 & 12 weeks	Silicon single-shank electrodes 120x15 µm shafts	First study to examine blood-brain barrier (BBB) permeability via IgG IHC Neuronal Loss is <u>not</u> progressive (stabilizes by 2 weeks) Inflammation and BBB leakage are persistent around chronic implants Tissue response is more variable at later time points	

Table 2.1 Continued.

Year	Author	Model	Implant Duration	Implant Type	Scientific Contribution	Caveats
2013	Barrese[1]	Nonhuman Primate	0-5.75 years	Parylene-C coated silicone UEAs 10x1	Largest NHP study to date (78 UEAs) Most failures (56 %) occur in year 1 48 % of failure mechanical related, 24 % biological failure Fibrous encapsulation of base noted	No matched end-point or comparative histology
2015	Nolta[7]	Rat	12 weeks	Parylene-C coated silicone UEAs 4 x 4 200 µm tapered shafts	First study to correlate FBR biomarkers (BBB leakage & GFAP) with reduced electrode performance Multiple penetrating injuries lead to exacerbated BBB leakage and tissue loss	Very few devices (2 of 28) reached experimental end-point
2016	Barrese[14]	Nonhuman Primate	37-1051 days	Parylene-C coated silicone UEAs 10 x 10 200 µm tapered shafts	Progressive meningeal encapsulation separates array from cortex FBR leads to degradation of materials Drop in impedance, signal and viable channels over time	

Table 2.2 Previous Studies Documenting the Histological Response to Cortically Implanted UEAs.

1st author	Year	Species	Duration	Number of UEAs	Number of UEAs histologically assessed
Schmidt [121]	1993	cat	1 day & 6 months	27	27
Nordhausen [197]	1996	cat	acute	5	1
Rousche [12]	1998	cat	3-20 months	12	9
Normann [61]	1999	cat	6 months	1	1
Maynard [13]	2000	cat	3-8 months	12	4
Warren [198]	2001	cat	acute	4	1
House [10]	2006	human	acute	8	1
Ward [19]	2009	rat	1 month	6	2
Barrese [1]	2013	NHP	0-5.75 years	78	7
Nolta [7]	2015	rat	1-12 weeks	27	13
Barrese [14]	2016	NHP	37-1051 days	8	6
Cody [15]	2018	rat	12 weeks	10	2

Table 2.3 Rats Versus Primate Neurovasculature.

The table compiles reported literature values for a number of measures of vascular aspects in the primate and rodent cortex.

Aspect	**Primate**	**Citation**	**Rat**	**Citation**
Cortical Thickness	2.5 mm	[133]	1.83 mm	[147]
Vascular Volume	2.43 - 3.02 % 2.49 %	[133] [199]	2.52 %	[200]
Capillary Diameter	6 - 8 μm	[133], [137]	3.5 - 4 μm 6 μm	[132] [200]
Descending Arteriole Diameter	40 μm	[135]	11 μm	[136]
Descending Arteries: Ascending Vein Ratio	1.6:1	[137], [200]	1:1.8 1:3 1:2.67	[150] [136] [26]
Vascular Length/mm^3	0.5 mm/mm^3	[133]	0.88 mm/mm^3	[132]
Vascular Surface Area/mm^3	13.6 mm^2/mm^3	[199]	5.19-7.24 mm^2/mm^3	[201]

CHAPTER 3

A COMPARISON OF THE TISSUE RESPONSE TO ANCHORED AND UNANCHORRED CHRONICALLY IMPLANTED HIGH DENSITY PENETRATING MICROELECTRODE ARRAYS IN RAT CORTEX

3.1 Abstract

The chronic foreign body response to silicon high density penetrating arrays that were anchored to the skull was compared to unanchored, freely floating devices implanted into the motor cortex of male Sprague Dawley rats. Consistent with previous reports with single-shank microelectrodes, the anchored arrays showed a greater FBR, including increased fibrotic encapsulation, a greater lesion cavity area under the array, greater GFAP immmunoreactivity and increased immunoreactivity of neuroinflammatory biomarkers CD68 and IgG. Regardless of the anchoring approach, retrieved arrays had adherent activated (CD68+) macrophages and patches of foreign body giant cells mostly associated with the sides and underside of the array. In spite of a reduction in the FBR, unanchored, freely floating devices were observed at various angles that deviated significantly from their original implantation position, indicating that this approach leads to changes in device orientation over time. Our results confirm that the method of anchoring a penetrating high density microelectrode array significantly affects the magnitude of brain tissue response, and raise questions whether similarly designed freely

floating or wireless high density arrays will be capable of maintaining their recording site position in their intended targets over chronic time frames.

3.2 Introduction

Cortically implanted high density microelectrode arrays have provided paralyzed patients with the ability to control computers and robotic prosthetics [2], [66], [67], [71], [72], [74], [76], [202]. Available evidence indicates that the chronic performance of such high density arrays is characterized by inconsistent recording performance over time, which hinders their wider clinical implementation [1], [6], [18], [69]. Studies have demonstrated that UEAs implanted in cortical brain tissue elicit a chronic foreign body response (FBR) that includes encapsulation of the array with tissue comprised of both neural (gliotic) and mesenchymal (fibrotic) origin [1], [3], [7], [9], [12], [121]. In addition, a loss of cortical tissue under the base of high density penetrating arrays has been observed [1], [7], [10], [11], [14]. Moreover, the degree of blood-brain barrier (BBB) dysfunction, astrogliosis and tissue loss under chronically implanted high density penetrating arrays correlates with declining recording performance in the rat [7]. Therefore, preserving cortical tissue under the array and reducing the FBR surrounding chronically implanted high density microelectrode arrays remains a goal in the field of Neural Engineering.

Our group and others have reported that single-shank penetrating microelectrode arrays that are fixed to the skull (anchored) elicit a greater FBR compared to electrodes left unanchored or freely floating at the surface of the brain [21]–[23], [25], [203]. Single-shank penetrating microelectrodes cause less physical damage upon implantation compared to higher density arrays with multiple, regularly spaced penetrating microelectrode shafts, such as the Utah Electrode Array (UEA) utilized in the majority of nonhuman primate and clinical trials. Although the precise mechanisms are unclear, freely floating UEAs chronically implanted in the cortex have been observed in various orientations that differ from their original position after implantation [1], [7], [12], [14].

An additional observation that has not been reported in response to single-shank penetrating microelectrode implantation in the mammalian cortex is the formation of a stroke-like lesion cavity observed weeks to months after implantation. Demonstrated with a stab wound model, where a high density array is inserted and then removed shortly after implantation in the rat cortex, the injury from device penetration leads to a pyramidal shaped lesion cavity that was observed as soon as 4 weeks post injury [7]. Such stroke-like lesion cavities vary in size and location, likely attributable to the variable initial physical damage caused to the neurovasculature by device implantation and the variable subject-specific immune response that follows.

Current theories regarding the mechanism of recording instability and degradation of recording performance of high density arrays suggest that mechanical and physical damage, along with various elements of the FBR, combine to challenge chronic device function [1], [7], [14]. While the recent literature reflects a concerted effort to identify and characterize each of these mechanisms, most of the studies using regularly spaced high density silicon microelectrode arrays like the UEA have used freely floating arrays implanted in the mammalian cortex that are tethered by a flexible wire bundle attached to the backside of the array. At present, it is unclear whether the manner in which high density microelectrode arrays are anchored has an impact on the magnitude of the FBR and device orientation over time.

To address this issue, the current study was designed to examine the influence of the anchoring mechanism of a 4 x 4 UEA implanted in the rat motor cortex over a 12 week indwelling period. Array orientation, neural lesion size and various components of the FBR were quantified. Ours results confirm an earlier study performed with far less complicated single-shank microelectrodes, indicating that the method of anchoring a penetrating high density microelectrode array significantly affects the magnitude of FBR [21]. These results raise questions whether wireless high density arrays will be capable of maintaining their recording sites in their intended target tissue over chronic time frames.

3.3 Methods

3.3.1 Microelectrodes

Unwired silicon UEAs were custom fabricated by the University of Utah Nanofab for this study. UEAs were fabricated with a 1.6 mm by 1.6 mm base with 400 μm regularly spaced, 1 mm long microelectrode shafts in a 4 x 4 pattern (**Figure 3.1**). The microelectrode shaft tips were plated with platinum before the entire array was coated with Parylene-C to a thickness of 5 μm, and then the tips were exposed via partial insertion into aluminum foil followed by reactive ion etching to remove the parylene coating from the tips. Thin (0.22 mm) stainless steel wires were attached to the back of each UEA with a UV-curable acrylic (Dymax 1187-M, Torrington, CT) to assist in handling the devices. Each UEA was cleaned by dipping into agitated solutions of 1 % Alconox, DI water (3x), acetone, isopropanol, DI water (3x) and then packaged into holders for ethylene oxide (EtO) sterilization at the University of Utah Hospital Surgical Processing Center.

3.3.2 Surgery

All animal studies were conducted in accordance with the University of Utah Institutional Animal Care and Use Committee to assure NIH guidelines for the care and use of laboratory animals (NIH Publication #85-23 Rev 1985) have been observed. Adult male Sprague Dawley rats (Charles River, San Diego, CA) with an average weight of 425 ± 50 g were stereotactically implanted with 4 x 4 UEAs. Animals were anesthetized with 5 % isoflurane, skull shaved/disinfected and placed in a stereotactic frame (David Kopf Instruments, Tujunga, CA). During the procedure animals were maintained at 2.5 % isoflurane. They were administered i.p. Buprenorphine (0.1 mg/kg) at surgery and 12-hours postoperatively. Carprofen (subcutaneous) was given at surgery and 2 days following at a dose of 5 mg/kg. Bupivacaine (2 mg/kg) was administered at the incision site. An incision down midline, or 5 mm to the left of midline in unanchored cases, and blunt dissection exposed the skull surface. A pneumatically driven circular diamond burr dental drill was used to cut a 3 mm by 2 mm craniotomy in the right hemisphere, centered at 1 mm rostral of bregma and 3 mm lateral to midline, above the primary motor cortex [204]. As in previous studies, irrigation with PBS was utilized to minimize the impact of heat generated during drilling. The dura was retracted with a 23 ga needle and large surface blood vessel locations were noted. Bleeding from incision and craniotomy was controlled with cotton gauze and air-drying before a UEA was inserted into the cortex to a depth of 1 mm with an electrode manipulator mounted to the stereotaxic frame (Kopf, model 1460-1); care was taken to avoid large surface vessels when possible. Implantation order was randomized.

3.3.3 Unanchored Preparation

In the unanchored preparation (n = 6), after implantation, a quick setting silicone elastomer (Kwik-Cast, World Precision Instruments, Sarasota, FL) was used to fill in the craniotomy around the implanted device. The handling wire was clipped and then another layer of elastomer was added to cover the exposed wire end (**Figure 3.1, B**). The skin was sutured with 5-0 polygalactin sutures (Ethicon, Somerville, NJ), with the suture line centered over the left hemisphere, opposite the implant. Animals were allowed to recover in individual cages with daily monitoring.

3.3.4 Anchored Preparation

In the anchored preparation (n = 7) four self-tapping bone screws (shaft length 4.7 mm, diameter 1.17 mm; Fine Science Tools, Foster City, CA) were placed at the four corners angled into the cranial ridge using pilot holes created with a handheld dental drill. The UEA was stereotaxically implanted and the craniotomy was filled with silicon elastomer around the implanted device in the same manner as the unanchored UEAs. However, in this case, UV curable acrylic (Dymax 1187-M, Torrington, CT) was applied over the surface of the skull such that all 4 screws and the exposed handling wire were embedded in resin (**Figure 3.1, B**). After curing, the handling wire was clipped and another layer of acrylic applied to cover the heads of the screws and the handling wire tip with a smooth tapered dome. The skin was not sutured but allowed to form a tight junction with the edges of the acrylic head stage. Animals were allowed to recover in individual cages with monitored daily.

3.3.5 Euthanasia and Tissue Processing

After a 12-week indwelling period animals were anesthetized with 5 % isoflurane and then euthanized by transcardial perfusion with 200 mL of ice-cold 0.1 M phosphate buffered saline (PBS), followed by 200 mL of 4 % paraformaldehyde (PFA) in PBS at a rate of 50 ml/minute. Animals were decapitated and the headstage was separated from the screws by cutting the UV glue with the dental drill. The headstage was carefully separated from the skull and the underlying silicone with a scalpel. In the unanchored cohort careful dissection allowed the devices to stay implanted in the brain while most of the anchored devices were removed with the overlying acrylic. Cranial bones were removed with rongeurs, the brain was removed and allowed to post fix 24 hours in 4 % PFA.

Gross photos of the explanted brains were obtained with a digital microscope (VHX-5000, Keyence, Osaka, Japan) before and after device removal. Brains were equilibrated in 30 % sucrose, embedded in tissue freezing media and sectioned at 30 µm on the cryostat (Leica Biosystems, Buffalo Grove IL) in the horizontal plane. Brains were leveled such that the cutting plane was parallel to the base of the device at the time of implantation; this allowed a maximum number of sections to be obtained that showed a reaction to all 16 microelectrode shafts at the same depth, in the same slice, when the device base was level with the cortical surface.

3.3.6 3D Surface Observations

For 3-dimensional (3D) reconstruction of surface features the implant location was imaged at 50x zoom in 3D mode with a Keyence VHX-5000 microscope. Multiple images (average 15) were acquired at a z-spacing of 100 µm per image. The Keyence software program registers the in-focus area of each picture and creates a 3D surface rendering. In order to estimate cavity volume, sagittal line profiles were drawn across the rendered surface at a spacing of 30 μm and averaged to obtain a 2D line profile detailing the surface height versus distance along the sagittal plane. The z-height profiles were overlaid with the *Paxinos Rat Atlas* in order to compare normal brain morphology with the observed surface [204]. Areas of difference were measured in Image J then multiplied by the number of line profiles and line spacing to calculate changes in cortical surface tissue. This process was repeated using line profiles drawn along the coronal plane and showed a difference in measurements of 2 ± 8.5 %. The two measurements were averaged.

3.3.7 Tilt/Migration Measurements

Unanchored devices in the brain after dissection were imaged in the sagittal and coronal plane in order to determine degree of device tilting and lifting. These images were analyzed in Image J and compared to the plane of the cortical surface to calculate a side-to-side tilt angle (α) and a front-to-back tilt angle (β) (**Figure 3.2, C and D**). From these 2 angles, the 3D Cartesian Formula [1] was used to calculate the absolute degree of tilt the electrode had shifted from the original implantation vertical z-axis (γ) using equation [2].

$$[1]\ \cos^2\alpha + \cos^2\beta + \cos^2\gamma = 1$$

$$[2]\ \gamma = \cos^{-1}\sqrt{1 - \cos^2\alpha - \cos^2\beta}$$

Additionally, the distance the device traveled vertically (z) from implantation was calculated from the sagittal image and used to calculate a total distance (D) that the average microelectrode recording tip moved from the original implant location using equation [3].

$$[3]\; D = \sqrt{\left(2\sin\frac{\gamma}{2}\cos\gamma\right)^2 + \left(2\sin\frac{\gamma}{2}\sin\gamma + z\right)^2}$$

In the anchored condition, devices remained attached to the head stage hardware and were lifted out during dissection. These devices did not appear to have any tilt or vertical displacement and remained anchored to the overlying acrylic head stage in the original orientation at implantation.

3.3.8 Immunohistochemistry

Immunohistochemistry was performed to identify antigens of interest (**Table 3.1**). Care was taken to avoid using mouse-derived antibodies where possible, as unspecific binding to endogenous rat IgG leads to background noise, due to antigenic similarities between the two species IgG isotypes. Furthermore, background endogenous IgG immunolabeling can also be reduced by using a 1 to 250 dilution of polyclonal goat antirat IgG bound to AlexaFlour 647 nm (denoted 647-GtαRtIgG@1:250) as a first step in all stainsets (Thermo A-21247). Antibody incubation steps were 12 hours, followed by 4 x 3 hours in 0.1 M PBS to rinse out unbound antibody. Cell nuclei were labeled with 4’6-Diamidino-2-Phenylindole, Dihydrochloride (DAPI) (D1306, Thermo Fisher Scientific, Waltham, MA) with 15 minute incubation at a concentration of 10 µM. Sequential processing was used when primary antibodies shared isotype. All steps were performed in batch to ensure uniform labeling of antigens.

3.3.9 Imaging and Quantification

For immunohistological comparison, all sections depths were based off distance below the actual cortical surface, not the raised tissue adjacent to the arrays, in order to compare similar anatomical depths in relation to the UEA as it was originally implanted. Horizontal sections were mounted on glass slides under stereoscopic observation with Flouromount-G (Southern Biotech, Birmingham, AL) mounting media. Sections were observed on the Nikon E600 upright fluorescent microscope. A motorized stage (OptiScan II, Prior Scientific, Cambridge, UK) and CCD camera (Retiga R6, Q-imaging, British Columbia, Canada) were controlled with Micromanager v1.4 (NIH) to capture a 3 x 3 grid of 10x photos or a 2 x 2 grid of 4x photos at the implant site. After light-field correction with autofluorescent plastic control slides (Chroma, Bellows Falls, VT) montages were assembled with FIJI (National Institutes of Health, Rockville, MD) using the “Stitching” plugin with 20 % overlap and linear interpolation.

For GFAP and NeuN immunolabels, 4x images were assembled into 2 x 2 montages for quantification. GFAP images were quantified to identify the lesion perimeter surface area by using the freehand selection tool to trace the edge of the upregulated GFAP+ perilesion perimeter and measuring the surface area contained within the lesion. In each section the number of visible electrodes was counted, as defined by a circular enhanced GFAP+ border.

The prismoidal formula (4) was used to calculate lesion volume from serial 2D sections, and summed over multiple sections to calculate a volume of affected tissue.

$$[4]\ \mathrm{V} = \sum_{\mathrm{n}=1}^{\mathrm{n}-1} \frac{\mathrm{L}}{3}\left(\mathrm{A_n} + \sqrt{\mathrm{A_n A_{n+1}}} + \mathrm{A_{n+1}}\right)$$

Where V = estimated volume, A_n = surface area of interest in section n, A_{n+1} = surface area of interest in section n + 1, L = distance between section n and (n + 1) and n = total number of sections. Volumetric areas of interest were averaged across a cohort and compared statistically using a student’s t-test to test for significance ($p < 0.05$).

To calculate neuronal density from NeuN immunolabeled horizontal sections, one 4x image (2.5 mm x 3 mm) was taken centered around the base of the device. The image was thresholded, watershed separated and the cells were counted using the Analyze Particles function in FIJI. The neuronal count was then divided by the total area of tissue. In cases where the edge of tissue was in-frame, the area was subtracted from analysis area to obtain the number of neurons/mm^2.

CD68 and IgG quantification was performed on montaged 3 x 3 10x images, roughly a 9 mm^2 area centered under the base of the array. IgG was quantified by first deleting areas devoid of tissue, such as tissue loss or cystic cavity areas, the inside of blood vessels or the edge of the tissue section, and then calculating the average pixel intensity within cortical tissue. CD68 images were analyzed by first thresholding the image to only show pixels above a set baseline intensity, then the area of CD68 immunoreactivity was calculated and normalized to area of brain tissue analyzed. Quantification was performed using custom macros that applied the same settings to all images.

3.3.10 Second Harmonic Generation Imaging

Explanted devices were fixed in 4 % PFA and imaged with second harmonic generation (SHG) imaging to identify collagen in the electrode encapsulation material. The Ultima *in vitro* multiphoton microscope (Bruker, Billererica, MA) was used with a 16x water objective (Nikon) to view explanted devices. Images were obtained with the Praire View Software (Bruker) using an 800 nm excitation and 400 nm emission filter.

3.3.11 Statistical Analysis

From each animal, 5 sections were selected based off depth from the cortical surface. Sections from the same depth were averaged across a cohort and compared statistically using a student's t-test, with $p < 0.05$ considered significant. All results are presented as mean ± standard error of the mean.

3.4 Results

3.4.1 Failure Analysis

A number of studies of the FBR to MEAs have indicated that head stage removal or damage to connectors is a contributor to mechanical failure modes[1], [7], [16]. Two of 7 anchored animals lost their head stage and device early (8 and 9 weeks), and thus were excluded from analysis. All 6 of the unanchored animals retained their device until the study endpoint.

3.4.2 Explanted Devices

Anchored devices showed firm integration with the surrounding dural tissue. The tissue was similar to the dura in appearance with the exception of being markedly thicker around the device and at the edges of the craniotomy (**Figure 3.2**). The encapsulation tissue surrounded all edges of the base of the array and in all cases extended along the underside of the array base, where it typically occupied the upper third to half of the microelectrode shafts and showed a morphology that mirrored the changes observed on the brain surface. The tissue appeared fibrotic and in some cases showed hemosiderin deposits. Under immunohistochemical evaluation the tissue was densely cellularized, as indicated by DAPI+ staining, and rich in activated CD68+/IBA-1+ macrophages that were amoeboid in appearance.

SHG imaging showed that the encapsulation tissue contained fibrillar collagen (**Figure 3.2, D**), as SHG identifies fibrillar type I and IV collagen it is unclear what the specific nature of the collagen was [205]. SHG imaging of tissue sections also showed fibrillar collagen in the nonneuronal lesion core and lining blood vessels in the cortical parenchyma, but collagen was not observed in cortical tissue (data not shown).

The majority of unanchored devices were not covered with encapsulation tissue. Only one of 6 had fibrotic encapsulation similar to that observed in the anchored cohort. The other 5 devices were retrieved mostly clean of visible tissue (**Figure 3.2, A**). All of the unanchored devices showed a single-cell layer of variably adherent cells attached to the device surface that were IBA-1+ and CD68+ (data not shown).

Foreign body giant cells (FBGC) were identified attached to the base of the array irrespective of anchoring approach (**Figure 3.2, C**). The cells were multinucleated that labeled positively for IBA-1+ and in some cases CD68+. Towards the distal end of the microelectrode shafts we observed no difference in the morphology, type or level of attachment of the adherent cells, which were mostly IBA-1+ and CD68+.

3.4.3 Dissection and Gross Observation

During dissection it was noted that all of the anchored devices that made it to study endpoint were still in their original implant location, orientation and depth. A depression in the cortex was observed under all anchored devices, with an average surface tissue change of -1.10 ± 0.25 mm^3 as measured from the surface with 3D digital microscopy.

In all unanchored cases, the device did not retain its original implant orientation or depth of recording sites. A surface cavity was observed directly under the array. The raised cortical tissue, minus the void volume under the device, resulted in a positive change in surface tissue volume such that the observed surface tissue increased in volume 0.10 ± 0.31 mm^3, which was significantly different than the surface tissue loss observed under anchored devices (*p* = 0.016) (**Figure 3.3**). In general, neural tissue was raised at the brain surface around the edges of the array, tilting or lifting the device from the original implantation depth.

3.4.4 Changes in Unanchored Device Orientation

Arrays that were anchored to the acrylic head stage did not rotate or tilt at the 12-week study endpoint but maintained the same position as originally implanted. The unanchored devices had an average absolute tilt angle of 10 ° ± 5.9 ° front-to-back and 25 ° ± 12 ° side-to-side in relation to their original implant orientation (**Figure 3.4**). When viewed from above the devices showed an average rotation of 10 ° ± 3 ° from the original implant orientation. In addition, the unanchored devices were often slightly raised above the cortical surface on average 270 ± 68 µm. In some cases, unanchored devices were so tilted that microelectrode tips on one side of the array were visible from the surface **(Figure 3.4, A).**

Using the measurements of device displacement, we estimated the distance an electrode recording site moved on average from the original implant location. Across all unanchored cases, electrode tips moved on average 381 ± 130 µm from the original target recording location, unlike the anchored cohort, where device movement was not observed 12 weeks after implantation.

3.4.5 Histological Analysis

Figure 3.5 shows GFAP immunolabeling at depths of 450 μm, 650 μm and 1 mm below the original implant location in both cohorts. For comparative purposes, we show the FBR to a relatively well-oriented unanchored array, so that changes as a function of depth can be better understood. Towards the surface of the brain (450 μm under base), the upregulated GFAP+ perilesion perimeter was associated with a larger cystic cavity in the anchored compared to the unanchored cohort (1.38 ± 0.39 mm^2 unanchored versus 4.42 ± 0.78 mm^2 anchored, $p = 0.005$). At lower depths the size of the cystic cavities were comparable. The number of individual microelectrode shaft tips visible with GFAP labeling at the intended recording depth of 1mm was compared and showed that 8.7 ± 3.1 of the 16 electrodes were visible at this depth in the unanchored case versus 15.2 ± 0.8 in the anchored case ($p = 0.07$).

The number of NeuN+ cells per mm^2 was compared at depths of 450 μm, 650 μm and 1 mm under the base. In general, neuronal loss was observed along the borders of the lesion cavity and in proximity of microelectrode shafts, and decreased with depth into cortex. At a depth of 450 μm neuronal cell body density was significantly decreased in the anchored cohort ($p = 0.03$). At 650 μm, where cystic cavity size was comparable, neuronal density was significantly decreased in the anchored cohort ($p = 0.035$). At a depth of 1 mm below the cortical surface near the presumptive recording zone both cohorts had comparable levels of neuronal cell bodies ($p = 0.95$).

Anchored devices showed positive IgG immunolabeling around each of the microelectrodes shafts as well as diffuse immunoreactivity in cortical tissue extending > 1 mm away from all edges outside of the array footprint. In unanchored cases only a small fraction of microelectrode shafts showed IgG immunolabeling, and in no cases was IgG observed at a level comparable to that observed in cortical tissue as in the anchored cohort. **Figure 3.6** shows IgG quantification as well as representative images showing IgG near the microelectrode, as well as microglial/macrophage activation (as indicated by rounded IBA1+ cells) in the surrounding cortical parenchyma. A 7 mm^2 area was compared for average GFAP+ pixel intensity at 450 µm, 650 µm, and 1 mm under the base. We observed that GFAP was significantly higher in the anchored cohort when compared to the unanchored sections at all 3 depths ($p < 0.05$, **Figure 3.6, 4th Column**).

CD68 immunoreactivity was compared at a depth of 650 µm and showed an increase in immunoreactivity under the anchored device (6.0 ± 2.4 unanchored versus 11.0 ± 3.9 anchored, $p = 0.29$). Although this difference was not statistically significant, CD68 immunoreactivity showed linear correlation with average IgG intensity within each cohort ($R^2 = 0.94$ unanchored & $R^2 = 0.89$ anchored) (**Figure 3.6, Bottom Row**).

When devices were heavily tilted, it was qualitatively observed that the intensity of FBR biomarkers increased as a function of exposed surface area of the device that was in contact with cortical tissue. **Figure 3.7** shows a horizontal section that shows a high degree of device tilting. GFAP intensity was upregulated surrounding the entire surface of the device and markers of CD68 and IgG were elevated in cases with an increased amount of exposed surface area. Additionally, cystic cavity area was larger in tilted devices, as the presence of the device base within cortical tissue led to enhanced areas of cortical tissue loss.

Combined IgG, NF200 (axons) and RIP (myelin) immunolabeling indicated that demyelination is observed in the vicinity of electrode tracts, as well as surrounding nonneuronal lesion cores. The pattern of demyelination was similar in distribution to IgG immunolabeling, showing a tapering decrease with distance from electrode shaft or lesion border.

3.5 Discussion

The present study indicates that anchoring a high density silicon microelectrode array to the skull increases the size of the lesion resulting from implantation and increases the magnitude of FBR compared to freely floating, unanchored arrays examined 12 weeks after implantation using a rat model. The other major difference between the cohorts was that the recording sites of unanchored freely floating arrays were rarely all located in the planned stereotactic target tissue after a 12-week indwelling period, while those firmly anchored to the skull maintained their original implantation position with their recording sites located in the same cortical plane as originally targeted.

Increased FBR around anchored high density microelectrode arrays may result from differing tethering forces, differing amounts of meningeal encapsulation, or the presence of the headstage, all of which likely enhanced the neuroinflammatory burden. Although the size of the lesion and magnitude of the FBR differed across the cohorts, the spatial distribution of FBR associated biomarkers agreed with previous studies [7].

As was observed in a previous study using a single shank electrode, we also observed areas of demyelination surrounding microelectrode shafts [90]. Areas of demyelination were also observed in the perilesion perimeter surrounding cystic cavities, which together likely affect neural function in the cortex (**Figure 3.8**).

We observed cystic lesion cavities adjacent to and below the base of the UEA, generally in a pyramidal shaped volume that extended in some cases 1 mm into the cortex.

The lesion cavities were similar in shape, size and variability to those observed in a previously published study using a similar UEA but examined at a much shorter indwelling period [7], indicating that lesioned cortical tissue likely does not regenerate. In larger mammals, such as cats and nonhuman primates, UEAs examined after long indwelling periods are often found recessed into cortical surface depressions that surround the device [1], [12]–[14], [16], [20], [119]. It is possible that such features represent the settling of devices into lesion cavities that continue to remodel due to the persistent inflammatory stimuli associated with the FBR.

Insights into the potential mechanisms responsible for cortical tissue loss may be gained by considering the similarities resulting from penetrating electrode implantation and neurovascular insults that occur in experimental stroke models. In a recent study, occluding a single descending arteriole or ascending venule by photothrombosis led to a cylindrical cortical infarct roughly 0.5 mm in diameter and 1 mm deep, defined by loss of NeuN labeling [26]. Moreover, when spacing between penetrating vessel damage was < 1.6 mm such infarcts coalesced into larger cortical lesions than would be predicted with isolated occlusions alone.

On the UEA used here and used clinically, the microelectrode shafts are regularly spaced in a grid-like pattern separated by 0.4 mm. The cortical tissue volume occupied between the electrode shafts of the 4 x 4 array is 1.44 mm^3. Given that each cubic millimeter of rat cortex contains 6 penetrating arterioles and 16 penetrating venules [26], it appears highly likely that the at least some of the implanted microelectrode shafts would physically damage a portion of the arterioles and venules during implantation. It also seems reasonable that the implantation induced vascular damage varies from animal to animal. These observations indicate that next generation high density arrays should try to minimize blood vessel damage associated with array implantation by either decreasing electrode diameter or by increasing inter-electrode spacing.

Wireless or unanchored high density recording arrays offer a promising solution to eliminate the need for head stage hardware and percutaneous connectors thereby lowering the risk of infection, a major clinical risk with percutaneous leads [122], [206]. We observed that devices left unanchored and freely floating at the surface of the brain were often tilted, rotated and lifted 12 weeks after implantation. Similar observations cats and nonhuman primates also have reported changes in array position after chronic time frames, often referred to as "device settling" where a cortical surface depression is observed under chronically implanted devices (**Figure 2.5**) [1], [7], [12]–[14], [16]. Although the precise mechanisms are unclear, the variable vascular damage caused by device implantation and the ensuing tissue remodeling associated with the FBR, may explain the variety of angles observed in this study.

It is important to note that in the rat we observed little fibrotic encapsulation tissue surrounding unanchored arrays. Anchored devices stayed in place, but were covered by fibrotic encapsulation tissue that extended underneath the array and into the superficial lesion cavity. Similar dural encapsulation has also been observed with UEAs in cats and nonhuman primates, and has been suggested as a causative factor behind arrays being lifted and twisted from their originally implanted position [1], [7], [12]–[14], [121]. The anchored implants in this study were all encapsulated by a 200 - 500 μm thick layer of collagen-rich fibrous material along the base that was continuous with dural tissue and occupied with vimentin positive cells, presumably indicating the presence of fibroblasts. Following CNS injury such as dural resection and cortical impact injuries, meningeal cells, macrophages and dural fibroblasts infiltrate lesion cavities and reform the meningeal barrier, creating a fibrotic scar that inhibits axonal regeneration [30], [32], [161]. It appeared that implantation-associated lesion cavity filled in with this meningeal-origin tissue, which often mirrored the size and shape of underlying cortical surface depressions. These results indicate that strategies to avoid implantation-associated injury could reduce both meningeal encapsulation and cortical surface tissue loss.

In the case of unanchored devices, a thin dural/arachnoid layer was observed above devices and encapsulating the silicon used to fill the craniotomy, indicating that dural closure may have occurred over the top of unanchored freely floating arrays. The results suggest that strategies that actively promote dural closure after array insertion may be able to engineer connective tissue regrowth away from underside the device base to stabilize the array.

The encapsulation tissue observed underneath anchored arrays contained many amoeboid CD68+/IBA-1+ activated macrophages, which have been shown to secrete a number of proinflammatory and neurodegenerative cytokines and other soluble factors that likely exacerbate the FBR and may affect the size of the stroke-like cavity caused by high density penetrating array implantation in the highly vascularized cortex [94], [95], [207]. These results indicate that the meningeal aspects of the FBR is perhaps as important as glial encapsulation as a target to improve long-term function of UEAs [1], [14].

Quantitative immunohistochemistry confirmed previous studies that have shown that unanchored devices have a decreased FBR [21]–[23], [25], [33]. The majority of observed differences occurred near the cortical surface, where the base of the device is in contact with neural tissue. It was noted in both cohorts that biomarkers of neuroinflammation (IgG), neuronal loss (NeuN) and cystic cavity area decreased with depth into the cortex, indicating that the FBR to UEAs is a depth-dependent tissue reaction that tapers off toward the tips where the recording zones are located. It has been suggested that this is due to the decreased diameter of electrode shafts and associated reduction of implantation induced tissue damage as a function of depth into the cortex [121]. The FBR occurred irrespective of the orientation of the array in cortex, where we observed that even devices that were shifted almost perpendicular to their original implantation position exhibited a FBR along the exposed surface area of the array (**Figure 3.8**).

Consistent with previous reports, there was the strong correlation between the number of CD68+ labeled cells in cortical tissue and the degree of BBB dysfunction estimated by the amount of IgG immunolabeling in cortical tissue [90], [106], [107]. The initial BBB disruption that accompanies device implantation causes localized bleeding in the brain, which triggers the inflammatory sequela that follows [82]. The resulting extravasated blood proteins such as fibrinogen, albumin and IgG have negative effects on neuronal viability and activate microglia and astrocytes that initiate wound healing responses [27], [112]–[115]. Available evidence suggests that recruited macrophages and activated microglia, like those found around chronically implanted devices, contribute to further breakdown of the BBB resulting from recruitment and trafficking across postcapillary venules near the implant [27], [115], [116], [208].

This cycle, where initial BBB disruption leads to further BBB disruption explains the chronically leaky BBB observed adjacent to chronically implanted microelectrodes and other types of implants [108], [109], [209]. Collectively these results support the suggested model of electrode failure [108], where initial vascular damage leads to activation of glial cells that further leads to BBB disruption by the recruitment of myeloid cells, resulting in plasma protein accumulation and persistent activation of macrophages as observed for as long as implant remains in tissue.

3.6 Conclusions

Our results show that implant anchoring approaches can significantly affect the magnitude of the foreign body response to high density recording devices chronically implanted in rat cortex [21]. While unanchored arrays had a significantly reduced FBR in the upper cortex, they rarely kept their originally implant orientation, resulting in significant changes in the recording zones 12 weeks after implantation. While multiple factors likely contribute to the differing FBR responses, this study shows that in the absence of significant fibrotic encapsulation, neural tissue remodeling within the cortex is sufficient to affect the orientation of unanchored UEAs. The results of this study raise important questions of how to proceed with anchoring current high density microelectrode arrays and whether similarly designed next generation high density wireless arrays will be capable of maintaining their recording sites in their intended targets over chronic time frames without some sort of anchoring system in place.

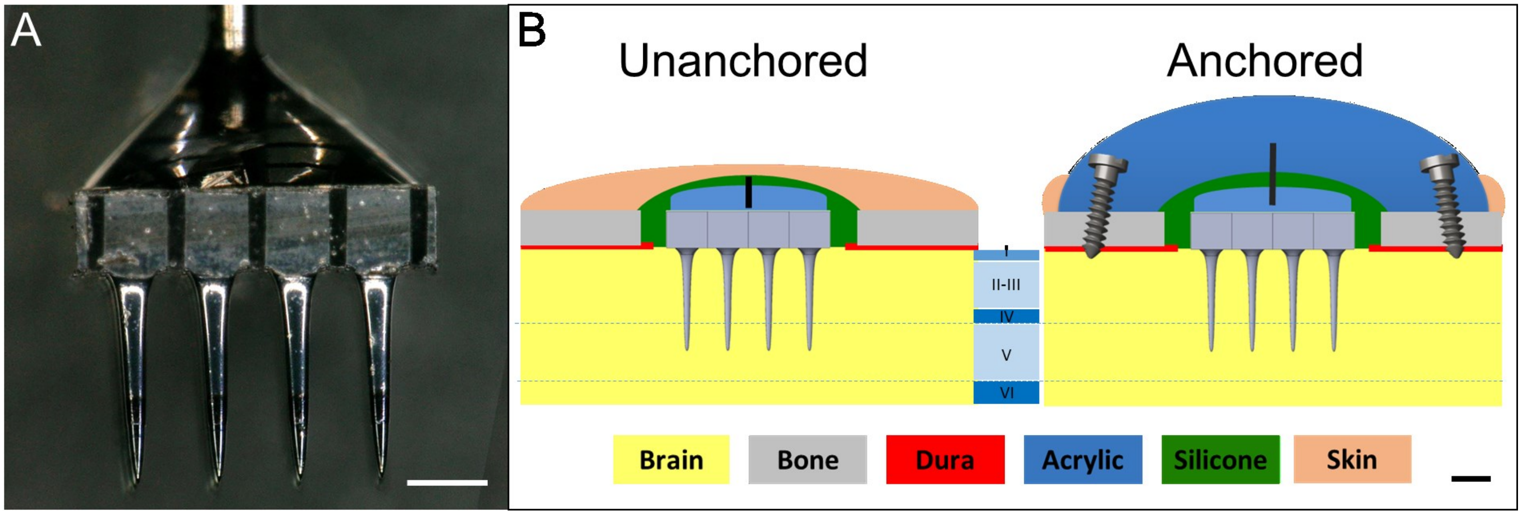

Figure 3.1 Device utilized and diagram of anchoring approach. A) 4 x 4 UEAs were used in this study, secured to a handling wire on the backside with acrylic. B) In the unanchored approach silicone was used to fill the craniotomy space and skin sutured over the implant. In the Anchored approach, an acrylic head stage was assembled that anchored the handling wire to cranial bone screws. Cortical Layer V is outlined with blue dashed line, as this was the intended target recording location. Scale bars 400 µm.

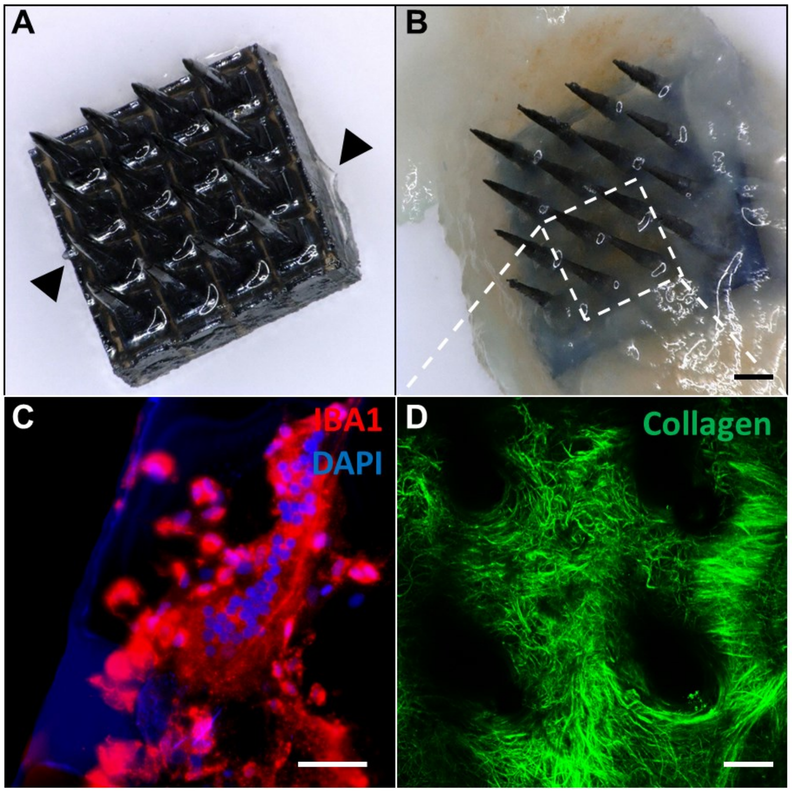

Figure 3.2 Explanted devices showing cellular and material attachment. A&B) Representative explanted devices viewed from the bottom of the array. Scale bar 250 µm. A) Unanchored devices showed minimal attached tissue upon explant (arrowheads). B) Anchored devices were integrated with an encapsulation layer that was continuous with the dura. C) Foreign body giant cells were observed on the device surface, as indicated by a large multinucleate (DAPI, blue) IBA1+ cells (red). Scale bar 50 µm. D) Encapsulation tissue showed the presence of fibrillar type 1 collagen (green) under second harmonic generation imaging. Scale bar 100 µm.

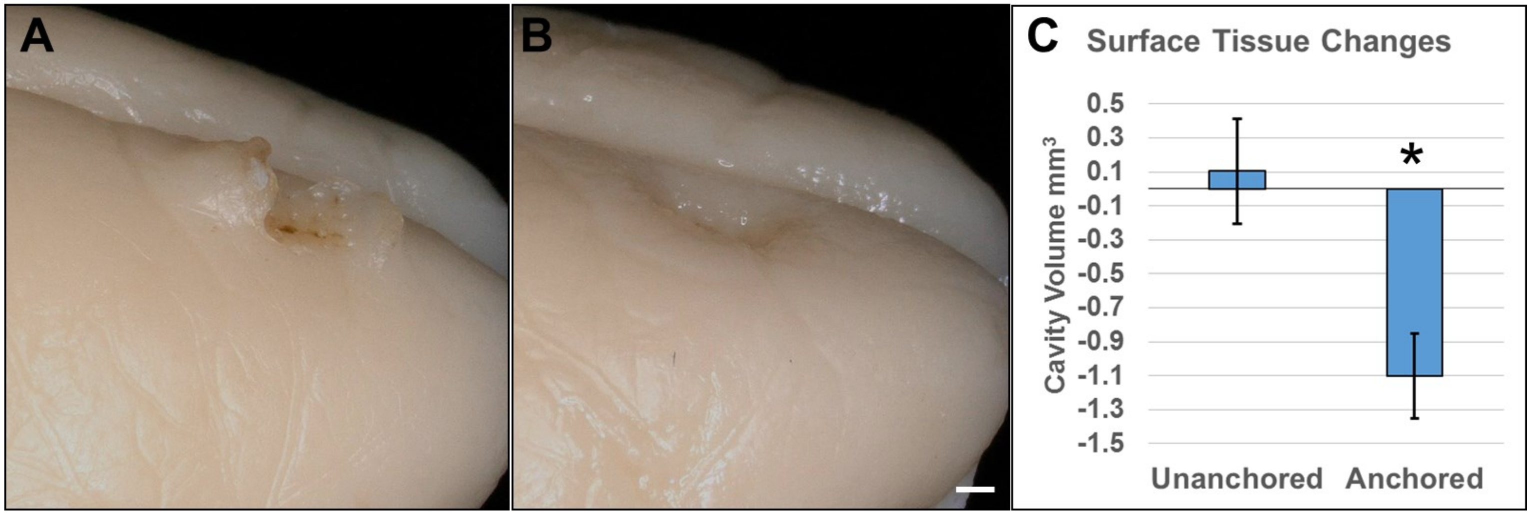

Figure 3.3 Surface tissue changes measured by 3D surface topology. A&B) Representative pictures of explanted brains. A) Unanchored animals had areas of tissue raised above the cranial surface surrounding edges of device, but also typically had a cystic cavity centered under the device. B) Anchored devices resulted in the formation of a notable surface depression. C) Anchored devices were observed to significantly increased surface tissue loss (*, $p < 0.05$). Scale bar 1 mm.

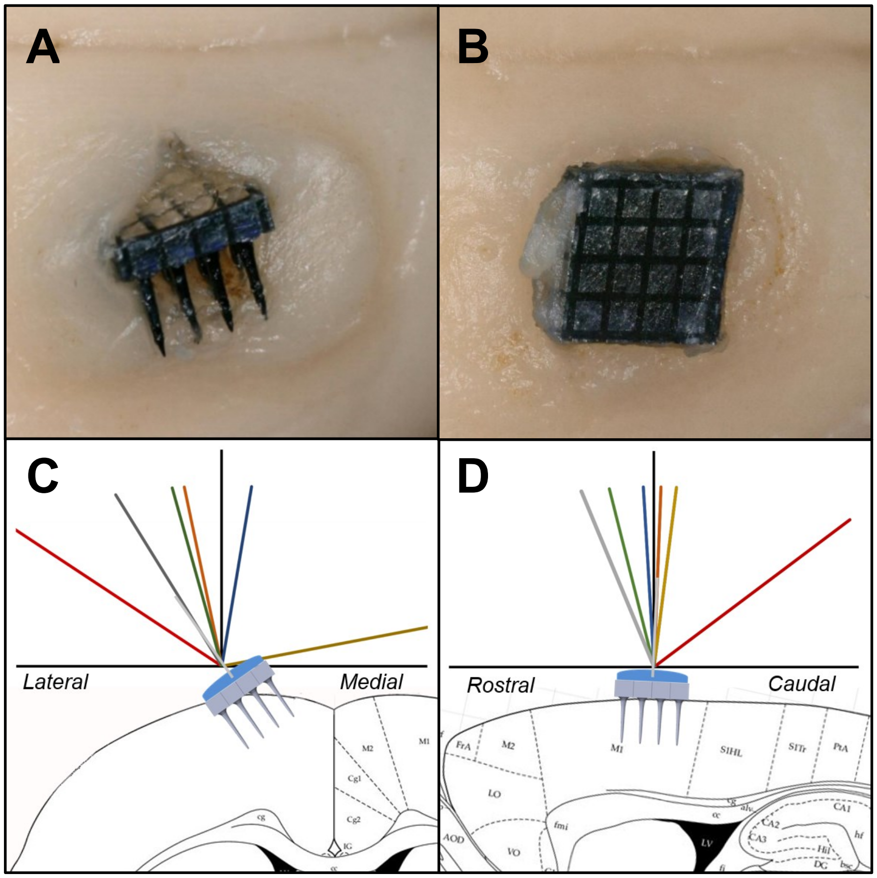

Figure 3.4 Tilt angle depiction and qualitative gross images. A) Unanchored device that is heavily tilted showing the lateral row of electrodes above the raised cortical surface. B) An example of an anchored device that did not tilt, showing the backside of the device. Scale bar 500 µm. C&D) Graphical depictions showing lines drawn perpendicular to the back side of the device when viewed in the A) coronal plane or B) sagittal plane. Illustrations adapted with permission from [204].

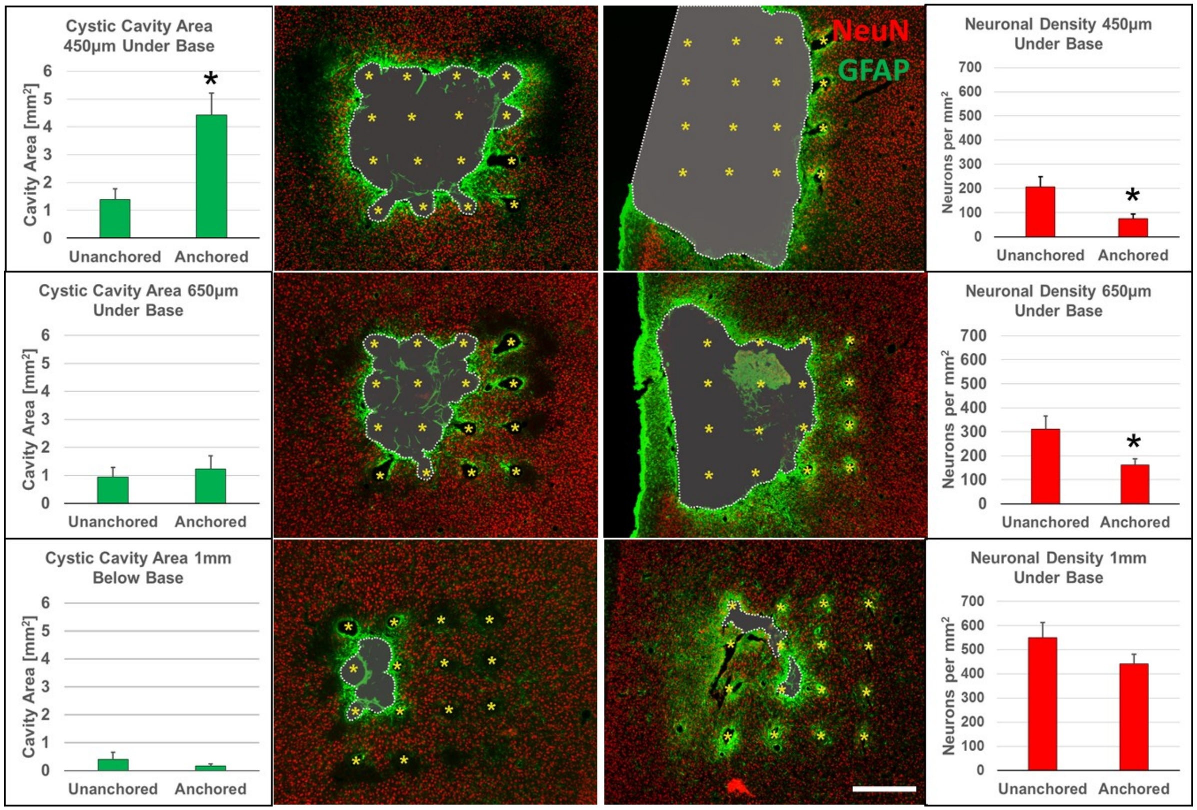

Figure 3.5 Cystic cavity area and neuronal density compared at 3 depths. (First Column) Cystic cavity area was compared at 3 depths below the device base and showed a significant increase in the anchored cohort at 450 µm below the base (*, $p < 0.05$). (Second Column) Representative histological sections from one unanchored animal and (Third Column) one Anchored animal show GFAP (Green) and NeuN (Red) labeling at all 3 compared depths. Greyed out areas represents cystic cavity area, highlighted by upregulated GFAP labeling at the lesion border zone, yellow asterisks indicate presumed electrode locations. Scale bar 500 µm. (Fourth Column) Neuronal density was compared across cohorts at each depth and showed a significant decrease in the anchored cohort at 450 µm and 650 µm below the base (*, $p < 0.05$).

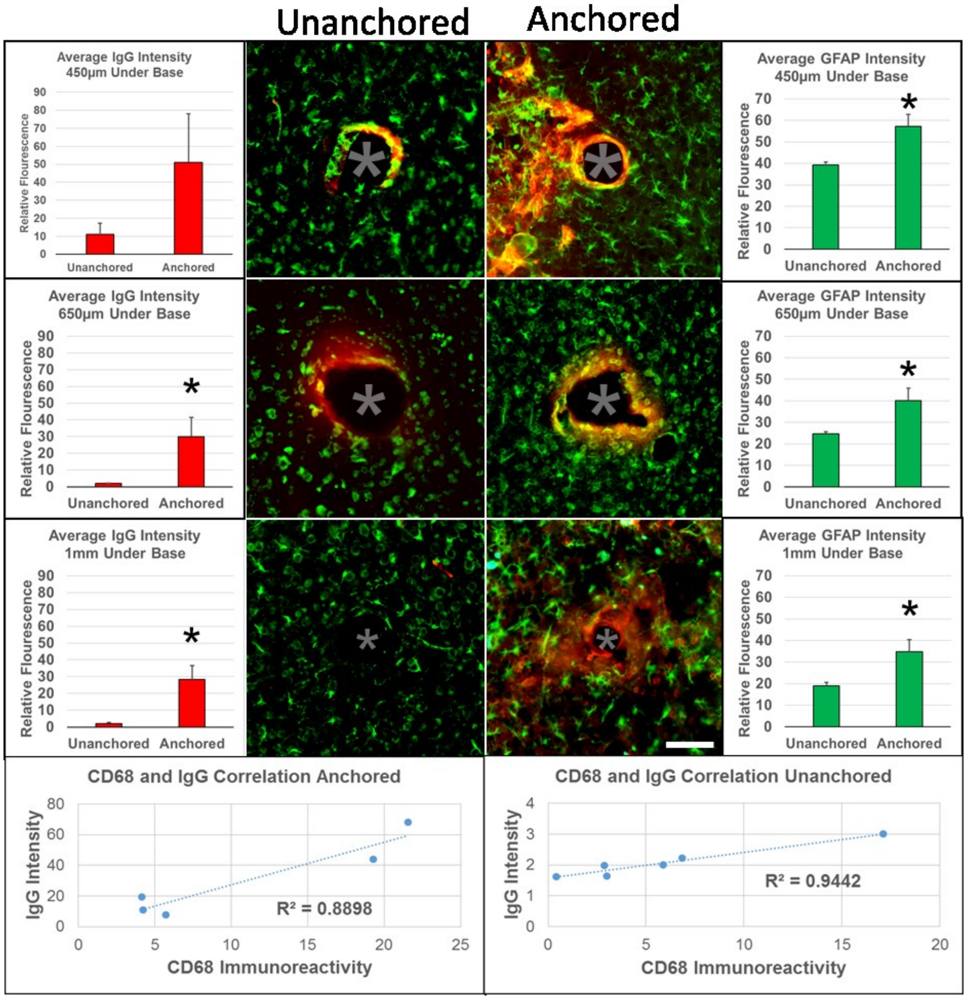

Figure 3.6 Relationship between IgG, CD68 and GFAP distribution. (1st Column) IgG intensity in brain tissue was compared at 3 depths and showed increases in the anchored cohort at all depths (*, $p < 0.05$). (2nd & 3rd Column) Qualitative images showing plasma protein leakage stemming from electrode tracts (IgG, red). Microglia/macrophages (IBA1, green) in the vicinity of implanted electrodes were observed to show a rounded morphology, indicating activation. Scale bar 100 µm. (2nd Column) Unanchored animals showed IgG labeling at the electrode interface, but rarely showed diffusion of IgG into cortical parenchyma. (3rd Column) Anchored electrodes had increased IgG intensity in brain tissue and IgG was observed to diffuse into the surrounding cortical parenchyma. (4th Column) GFAP intensity in brain tissue was statistically increased when compared across cohorts at all three depths (*, $p < 0.05$). (Bottom Row) At a depth of 650 µm under the base a correlation coefficient (R^2) between number of CD68+ cells and IgG intensity in brain tissue was calculated for each cohort and showed a strong correlation.

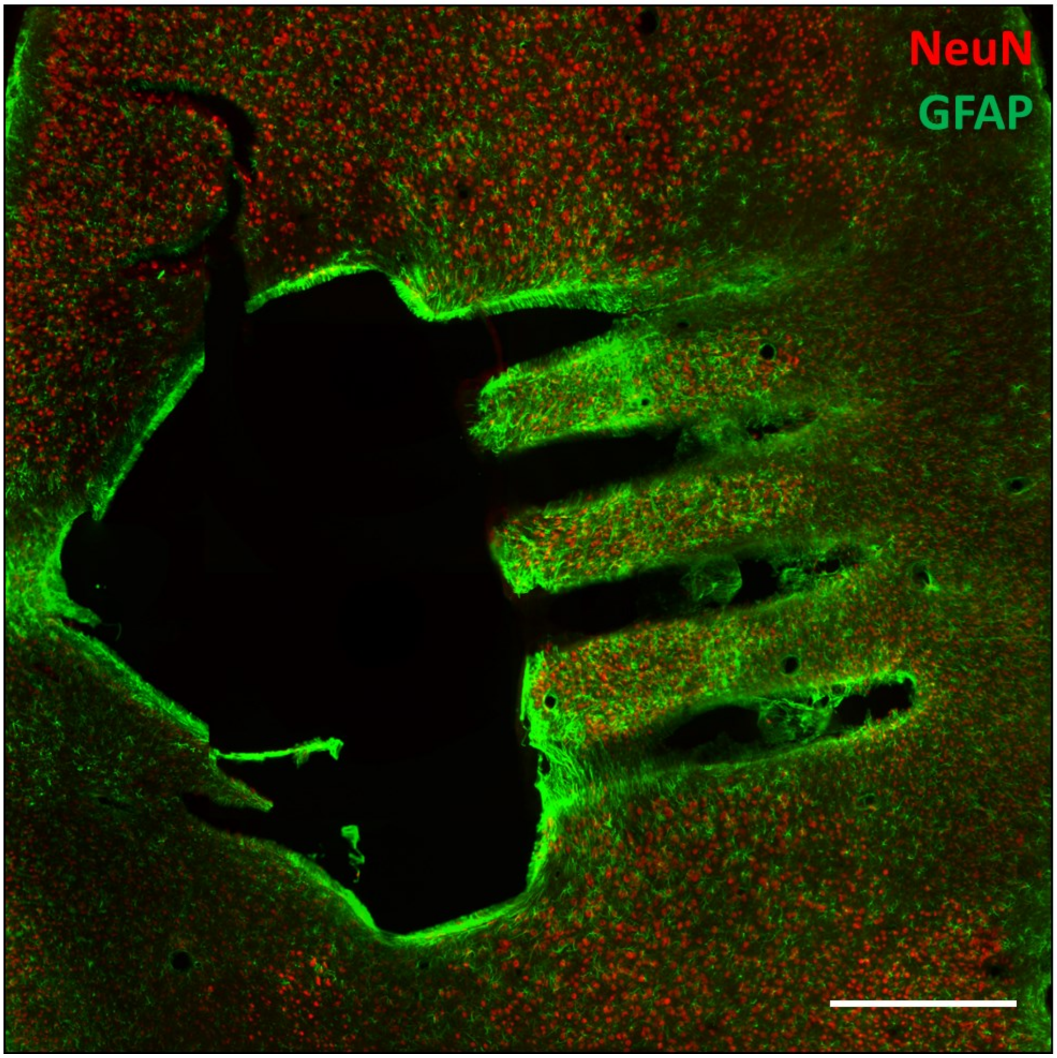

Figure 3.7 Horizontal section showing a high degree device of tilting. This unanchored device was so tilted that horizontal sections parallel to the cortical surface showed the side-profile of the device. Gliosis (GFAP, green) is observed surrounding the entire surface area of the device. Neuronal loss (NeuN, red) is observed in the vicinity of the implanted device. Scale bar 250 μm.

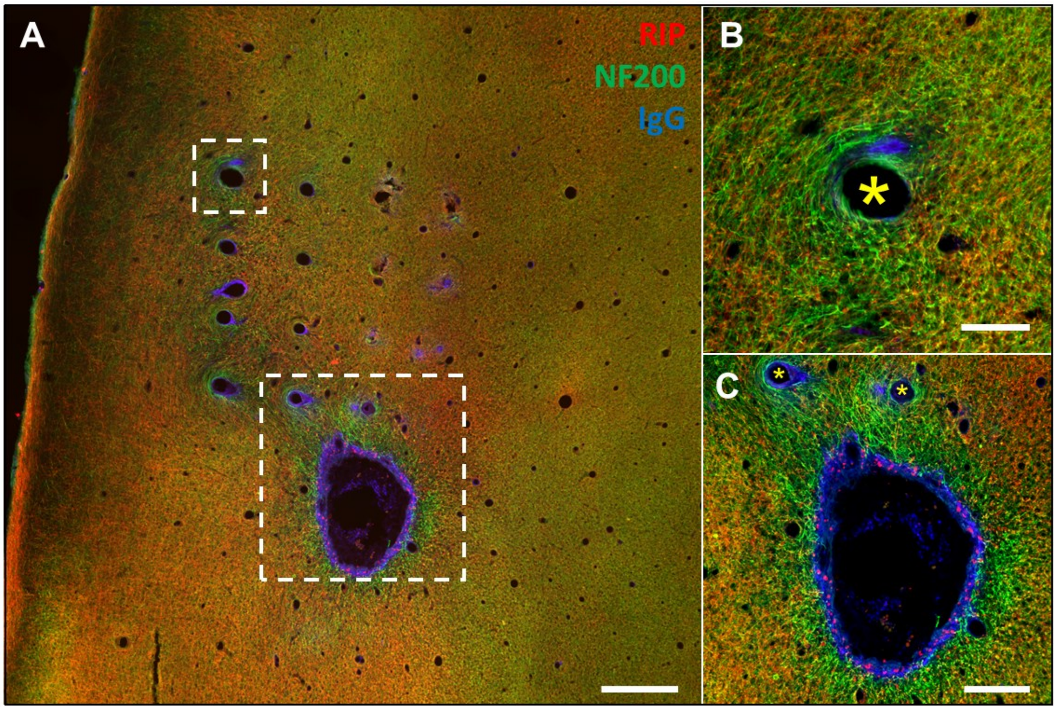

Figure 3.8 Demyelination observed near electrode shafts and in perilesion perimeter. A) Section from an anchored animal located 1mm below base of device showing the relationship of BBB breach (IgG, Blue), neuronal axons (NF200, Green) and myelination (RIP, red). Scale bar 500 µm. B) Inset shows IgG seepage into cortical parenchyma and demyelination surrounding the electrode shaft (yellow asterisk). Scale bar 100 µm. C) This lesion cavity started under the base in higher sections and tapered down in area with depth into cortex. Near the tips this lesion is located just caudal of the bottom row of electrodes (yellow asterisks). Demyelination is observed in the perilesion perimeter. Scale bar 250 µm.

Table 3.1 Antibodies Utilized.

Each primary and secondary incubation step was performed for 12 hours, followed by 4 x 3 h rinses in PBS. Gt=goat Rb=rabbit Dk=donkey Ms=mouse Ck=chicken IgG=immunoglobulin G IgY=polyclonal immunoglobulin. All labeling steps performed in 4 % goat block in PBS, except when noted otherwise.

Label	**Primary**	**Secondary**
NeuN Neurons	CkαNeuN @ 1:1000 in Dk Block (EMD Millipore ABN91)	594-DkαCkIgY @ 1:1000 in Dk Block (Jackson 703-585-155)
CD68 Phagocytosis	RbαCD68 @ 1:500 (Ab Cam AB125212)	488-GtαRb @ 1:250 (Thermo A11034)
GFAP Astrocytes	RbαGFAP @ 1:1000 (Agilent Z0334)	488-GtαRbIgG @ 1:1000 (Thermo A11034)
IBA-1 Microglia/ Macrophages	RbαIBA-1 @ 1:500 (Wako 019-19741)	594-GtαRb @ 1:1000 (Thermo A11037)
IgG Blood in Brain	647-GtαRtIgG @ 1:250 (Thermo A21247)	N/A
NF200 Axons	RbαNF200 @ 1:1000 (Sigma N4142)	488- GtαRb @ 1:1000 (Thermo A11034)
RIP Myelin	MsIgG1αRIP @ 1:2000 (EMD Millipore AB1586)	TxRed-GtαMsIgG1 @ 1:2000 (Southern Biotech 1070-07)

CHAPTER 4

A COATING FOR THE UTAH ELECTRODE ARRAY TO CONTROL HEMORRHAGE AND MODULATE THE FBR

4.1 Abstract

Extracellular matrix (ECM) was investigated for its potential as a hemostatic and immunomodulatory coating to improve biocompatibility of chronically implanted high density microelectrode arrays, such as the Utah Electrode Array (UEA). The UEA suffers from biocompatibility concerns where implantation associated hemorrhage and persistent macrophage activation on the device surface lead to compromised neural tissue health in the vicinity of implanted devices. Previous work has failed to address hemorrhagic injury associated with implantation, largely because the majority of work has focused on single shank devices where implantation injury and exposed surface area are minimal in comparison to high density devices with as many as 100 closely spaced penetrating shafts. We explored *in vitro* assays to determine if ECM could serve as a surface-adsorbed device coating that limits hemorrhage and controls activation state of device-adherent macrophages. In order to do this, we developed protocol for isolation of cell-type specific ECM, performed *in vitro* assays of hemostasis and immunomodulation and developed an apparatus to coat proteins onto the complex surface geometry of the

UEA. These tests laid the fundamental groundwork for ongoing studies of ECM as a surface-adsorbed device coating to improve biocompatibility of chronically implanted high density penetrating devices.

4.2 Introduction

The Utah Electrode Array (UEA) is currently being evaluated clinically as a brain-machine interface to allow para- and tetraplegic patients to control robotic prosthetics (**Table 1.1**). Unfortunately, the UEA does not record signals for a clinically relevant timeframe, and one noted failure mechanism is the foreign body response (FBR) [1], [7], [12], [14], [15], [19]. A number of histological evaluations of chronically implanted UEAs have noted the loss of neuronal tissue under high density devices, where devices are often found recessed into cortical depressions and surface cavities [1], [7], [12], [13], [16], [20], [119].

Due to the highly vascularized nature of the cortical parenchyma, the implantation of UEAs results in notable vascular damage along electrode tracts and petechial hemorrhage in areas adjacent to implant [7], [10], [11]. In experimental intracerebral hemorrhage in rodents, blood products injected in the brain parenchyma lead to enhanced areas of neuronal tissue loss compared to saline injection [156]. Indeed, when UEAs are only briefly stabbed into the cortex, bleeding is noted and a pyramidal shaped lesion cavity forms as soon as 4 weeks after injury [7]. It is believed that this vascular damage from implantation and associated intracerebral hemorrhage leads to localized areas of tissue loss under the base of UEAs. It remains unclear how limiting implantation-associated hemorrhage could lead to improved device outcomes.

The extracellular matrix (ECM) is a complex combination of proteins, growth factors and cytokines and also contains a number of platelet-binding motifs that signal hemostasis upon vascular injury [84]. In the case of single-shank penetrating microelectrodes, coating the device surface with extracellular matrix (ECM) proteins has proven to be a successful strategy to reduce some aspects of the foreign body response (FBR) [37]–[40]. Recently, it has been shown that injection of ECM hydrogels can attenuate lesion formation in experimental models of traumatic brain injury and stroke in rats [35], [36]. It is speculated that such strategies work by altering macrophage activation state from a proinflammatory phenotype to a more proregenerative phenotype that supports wound healing [93], [112], [210]–[213]. While ECM has shown potential to improve integration of implanted materials, no study to date has attempted to utilize ECM as a hemostatic and immunomodulatory device coating to improve the biocompatibility of high density penetrating microelectrode arrays.

To facilitate study of ECM as a device coating, this work investigates methods to collect and characterize a number of cell-type specific ECMs, assay *in vitro* immunomodulatory and hemostatic capability, and describe an apparatus to coat such ECMs onto the surface of a UEA. Results from hemostasis assay indicated that no ECM tested was more effective than the already FDA-approved neurosurgical hemostat, Avitene™. Immunomodulation assay showed that all ECMs studies showed a variable ability to downregulate the activation state of serum-exposed primary rat microglia. In order to facilitate rapid clinical translation, Avitene™ was selected as a candidate ECM and investigated as a device coating. A dip coating apparatus was developed and optimum parameters were empirically derived with an end goal of uniform protein deposition across the complex geometry of the Utah Electrode Array (UEA).

Microscopic observation and indirect immunohistochemistry confirmed the presence of Avitene™ on the surface of coated devices. The apparatus developed showed satisfactory coating of devices and will facilitate the study of ECM as a device coating to improve biocompatibility of implanted high density microelectrode arrays.

4.3 Methods

4.3.1 ECM Collection

Primary astrocytes, meningeal fibroblasts, glial restricted precursors and mesenchymal stem cells were isolated from p1-7 male Sprague Dawley pups using established cell-isolation protocols [214]–[216]. After an initial grow up phase in DMEM/F-12 with 10 % FBS, cells were plated into T-75 flask (Cellstar, Sigma) for 7 days. Upon reaching confluence, growth media was supplemented with 1mM ascorbic acid and 2mM calcium chloride, as previous experience has shown these conditions enhance ECM production [217]. Cells were cultured for 2 weeks postconfluence.

At the end of this period cells were lysed by repetitive exposure to ice-cold hypotonic phosphate buffered saline (0.1x PBS, 1 mM) at pH 7.4, followed by 1 hour of DNAse (Sigma) treatment to remove nuclear remnants, followed by 3x rinses in 0.1x PBS. Remaining material was removed from the flask surface by gently using a cell scraper to dislodge the remaining film layer, frozen at -80 °C and lyophilized. The collected ECM was weighted on a microbalance and suspended in solution to facilitate the transfer of material from a fluffy powder to an intact surface coating. Specifically, low concentration (0.25 M) weak acid (acetic acid) was used to disaggregate bulk ECMs with 48 hours of continuous stirring on a stir plate at room temperature. ECMs were suspended at 1mg/mL and resulted in a milky solution that was further refined by passing through a 40 μm cell strainer, resulting in a homogenous suspension that does not settle out and can be used for dipping, spraying or dripping as necessary.

4.3.2 Tandem Mass Spectroscopy

To identify protein components within the coatings that may influence the FBR, samples of Avitene™ and Astrocyte ECM were analyzed with tandem mass spectroscopy (MS/MS) as previously described [217]. Samples were washed with 50 mM ammonium bicarbonate, denatured (ProteaseMAX™ Trypsin Enhancer, Promega, Madison, WI) for 30 min at room temperature, then trypsin (20 ng/ml) digested overnight at 37 C, and purified (Ziptip, Milipore, Billerica, MA). The MS/MS analysis was performed by the University of Utah Mass Spectroscopy & Proteomic Core Facility using a hybrid massspectrometer (LTQ-FT, Thermo Scientific, Waltham, MA). The primary peptide molecular mass spectra were acquired by Fourier transform ion cyclotron resonance. The sequencing of individual peptide spectra were performed by collision-induced dissociation in a linear ion trap. Sample proteins were identified by comparison of MS/MS measured peptide sequences in the Mascot trypsin-cut specific protein database (Matrix Science Inc., Boston, MA).

4.3.3 *In Vitro* Hemostasis Assay

To test the hemostatic capability of ECM coated surfaces, the Lee-White clotting time assay was utilized. Briefly, 1.5 mL polypropylene centrifuge vials were coated with 100 μL of ECM suspension (1 mg/mL in 0.25 M acetic acid) and dried under air flow in a sterile field. Whole blood obtained from Sprague Dawley rats (*n* = 4) via cardiac puncture was collected into syringes pre filled with sodium citrate (100 mM) at a 1:9 ratio. 450 μL of blood was gently pipetted into coated and uncoated vials and 50 μL of calcium chloride solution (100 mM) was added to precipitate coagulation. Vials were placed in a 37 °C water bath and gently tilted every 15 seconds to observe clot formation. Upon complete coagulation, when the vial can be fully inverted with the blood clot adhered to the bottom of the tube, time-to-clot was recorded for each protein coating. Samples were tested in triplicate and data was normalized to uncoated control vials and expressed as percent relative clotting time.

4.3.4 *In Vitro* Microglial Activation Assay

Microglia were collected from postnatal (p 0 - 3) Sprague Dawley rat pups by cortical dissection [218]. After a 10-day grow-up in a mixed cortical culture, microglia were isolated by shaking at 180 RPM for 6 hours in an incubator. The collected cells were plated onto glass coverslips, or coverslips on which ECM had been dehydration adsorbed, at 8,000 cells/mm^2 and allowed to grow in DMEM/F12 with 10 % fetal bovine serum. After 48-hour incubation, cells were fixed with 4 % paraformaldehyde (PFA) in saline. Antibodies for IBA-1, a pan macrophage marker, and CD68, a lysosome-associated marker for phagocytosis, were applied, followed by appropriate secondary fluorescently tagged immunomarkers. Random fields of view were imaged at 20x on an upright fluorescent microscope (Nikon, E600) and IBA1+ cells were classified as either ramified or amoeboid, indicating resting or activated states respectively. In brief, ramified cells are defined as those with 2 or more processes that extend > 0.5 x the cell diameter with high branching seen in at least one process [112]. Amoeboid cells show a distinct morphology, typically either rounded or with one trailing process with no branching on it. Each coverslip was considered a sample (n = 6) with 5 random fields-of-view counted per coverslip. Cohort means were calculated as a percentage of all cells counted that were ramified.

4.3.5 ECM Dip Coating

All coating steps were performed in a sterile cell-culture hood using sterile solutions and tools to ensure a pathogen free implant that needs no further chemical or ultraviolet sterilization. UEAs were cleaned with alconox (1 %), DI water, ethanol (95 %) and EtO treatment. UEAs were affixed to a handling wire with a UV-curable glue (Dymax, 1187-m) and the handling wire was stuck into a piece of silicone tubing glued to the syringe end. A second syringe and syringe pump pneumatically controlled the dipping of the UEA into a small volume of ECM suspension. The programmable syringe pump allowed control of the dip speed, time spent in solution, retraction speed and number of dips, all of which appeared to influence the assembly of ECM on the surface of the device. Sterile nitrogen streams pushed from under the electrode tips, to rapidly dry proteins directly to the surface. Manipulation of the large number of design input parameters (protein concentration, insertion speed, dip time, retraction speed, nitrogen flow rate, nitrogen flow direction, drying time, etc.) allowed fine tuning of this technique to control coating thickness and uniformity (data not shown).

4.3.6 Surface Characterization

Adsorption of protein to the surface of the UEA was confirmed with visual observation and immunohistochemistry. To aid in visualization and imaging, devices were incubated in Coomassie Brilliant Blue R250 (Sigma, St Louis, MO) a ubiquitous protein stain. First, an uncoated electrode was incubated with the dye for 10 minutes, then rinsed 3x in DI water. This device was imaged for a no-coating control. The same device was then subject to the dip coating process and again incubated in dye for 10 minutes, followed by 3 x 10 minute rinses, and then re-imaged.

Type 1 collagen immunohistochemistry was performed on dip coated devices to confirm the presence of protein on the device surface. Coated devices were incubated in a 1:1000 dilution of mouse anticollagen type 1 (Sigma, C2456**)** for 1 hour, followed by 3 x 15 minutes rinsing, following by incubation in a 488 nm labeled antimouse secondary. Other coated devices were incubated only in secondary antibody to confirm label specificity.

In order to visually observe devices that were coated for implantation studies, adsorbed ECM was viewed under dark field 10x stereoscopic observation as a thin-film; this approach was used to examine sterile devices, stored in optically clear petri dishes, to confirm uniform deposition. Any device that showed irregularities in the surface coating, was rejected for implantation studies; such irregularities included: the formation of large (1 mm diameter) fibrils, adsorption of larger agglomerates of protein or the formation of collagen sheets between electrode shafts.

4.3.7 Statistical Analysis

Coagulation times were normalized to an animal's average uncoated vial coagulation time and these normalized results were averaged across cohorts, using a pooled standard deviation to include the variability observed within each tested ECM. For microglial activation assay the total number of ramified cells in acquired randomized images was counted and expressed as a percent of total cells counted. Cohort means were compared using one-way ANOVA and Tukey post hoc analysis using the SPSS software package (IBM, Somers NY), with $p < 0.05$ considered significant. All results and bar graphs are reported as average ± standard deviation.

4.4 Results

4.4.1 ECM Collection

Cell-type specific ECM was isolated from primary astrocytes, meningeal fibroblasts, human mesenchymal stem cells (hMSCs) and glial-restricted precursors (GRPs). After lyophilization a white, lacy material was retrieved at a yield of roughly 2 milligrams of material per cultured T-75 cell culture flask, with the exception of GRP-derived ECM, which required 4 T-75's to obtain a similar yield. **Figure 4.1** shows this material after decellularization and lyophilization. All ECM types were capable of being suspended in 0.25M acetic acid at 1 mg/mL and after straining with a 40 µm cell strainer, and did not precipitate out of solution.

4.4.2 Tandem Mass Spectroscopy

MS/MS results showed that harvested cell-type specific ECM contained a number of extracellular proteins associated with hemostasis and wound healing. Analysis of Avitene™ with MS/MS showed that the material consisted of collagen type I but also contained of collagen type II and III, as well as the fibril organizing proteoglycan lumican (**Table 4.1**). The collagenous components have been shown to have hemostatic activity [219], [220]. Analysis of the astrocyte-derived ECM with MS/MS identified a variety of extracellular proteoglycans and glycoproteins that influence the coagulation cascade, wound healing and the FBR (**Table 4.2**).

4.4.3 Hemostasis Assay

Lee-White clotting time was found to be consistent with previously established clotting times for Sprague Dawley rat blood (2 - 5 minutes) in the uncoated group [221]. All ECM coatings tested showed the ability to significantly decrease the clotting time of rat blood compared to control ($p < 0.05$), but no difference was noted between tested ECMs (**Figure 4.2**).

4.4.4 Microglial Activation Assay

Microglia cultured in the presence of serum take on an amoeboid, or activated state, while resting or unactivated microglia show a ramified morphology [112]. On uncoated coverslips the percentage of ramified microglia was 5.5 ± 2.5 %, which was significantly less than observed when microglia were cultured in presence of ECM proteins (**Figure 4.3**). Astrocyte ECM showed the most pronounced increase in percentage of ramified cells (37.4 ± 12.9 %), and was significantly increased in comparison to both uncoated and Avitene™ coated coverslips, but not in comparison to other ECM types. Fibroblast, hMSC and GRP ECM showed the ability to statistically increase the amount of ramified cells in comparison to control, but no difference was noted between these ECM types.

4.4.5 ECM Coating

Figure 4.4 demonstrates the operation of the dip coating apparatus. The electrode is attached to the end of a syringe that lowers the device into and out of (red arrow) the protein solution, sterile nitrogen (yellow arrows) flows under the device and rapidly dries protein to the surface. Dip and retraction speed was set at 2 cm / minute, with a 5 second pause when device was fully submerged in coating solution. Sterile nitrogen streams pushed up from the bottom at an inlet pressure of 10 PSI. Four minutes of drying was required between dip coating cycles to prevent formation of self-assembled collagen fibrils that spanned multiple electrodes. Each device was dipped 8 times, as more dips resulted in the formation of fibrils, and less dips resulting in a coating that appeared irregular and had microscopically visible gaps.

4.4.6 Surface Characterization

Coomassie brilliant blue bound weakly to uncoated UEAs, but showed a bright blue color on Avitene™ coated UEAs. **Figure 4.5** shows a comparison between an uncoated device dipped in coomassie blue, and that same device dipped in Coomassie blue after 8 cycles of dip coating. A minor amount of blue color can be observed on the uncoated device; due to the apolar ring structure of the chemical, noncovalent adsorption onto the hydrophobic surface of Parylene-C is likely. After dip coating with Avitene™, Coomassie blue staining produces a distinctly stronger blue color than can be used to confirm the presence of a protein coating. This technique allowed optimization of dip coating parameters, as it made surface irregularities easily visible.

Type I collagen immunohistochemistry confirmed the presence of fibrillar collagen strands adhered to the device surface (**Figure 4.6**). These fibrils ranged in length from tens to hundreds of micrometers and showed a relatively even distribution across the device surface.

Dip coating apparatus was used to coat a number of devices for implantation studies. Specifically, 36 devices were coated for various animal implant studies. Of these 36 UEAs, only three met exclusion criteria under dark-field stereoscopic observation. Two devices showed formation of long (> 1 mm) collagen fibrils and one had a sheet of collagen spanning multiple electrode shafts. All unsatisfactory devices were towards the end of batch runs, indicating that the 1 mg/mL protein solution may have become dehydrated and increased in protein concentration.

4.5 Discussion

Results from this study showed that surface adsorbed ECM retains its hemostatic and immunomodulatory potential and can be coated uniformly onto the complex geometry of a UEA. *In vitro* assays showed that ECM has the ability to modulate microglial activation state towards a regenerative phenotype and has the ability to accelerate hemostasis in rat blood. Avitene™ was utilized to show that, with optimized parameters, the developed dip coating apparatus can coat proteins in a consistent and uniform manner. Taken together this highlights a useful approach for investigating the potential of ECM proteins to decrease the FBR to implanted high density penetrating microelectrode arrays.

A variety of ECM-based products are utilized commercially to control neurosurgical bleeding by utilizing intact platelet binding motifs to accelerate hemostasis [219], [222]–[224]. Platelet adhesion to collagen occurs in the presence of Von Willebrand Factor via Glycoprotein IV (GPIV) mediated contact and facilitates thrombus formation and platelet aggregation resulting in coagulation [225]. All ECMs tested showed the ability to be surface adsorbed and retain their ability to accelerate clotting time of whole blood compared to uncoated controls. This is possibly due to the presence of collagen in these ECMs. Tandem mass spectroscopy of astrocyte ECM showed that collagens are present in its ECMs and collagenase treatment of cell-type specific fibroblast, hMSC and astrocyte derived ECM has shown that collagen is a major component by mass [40], [217]. Avitene™ has been noted as a very strong inducer of hemostasis, and all other observed ECMs showed a comparable ability to accelerate coagulation, indicating that cell type specific ECM retains the ability to induce hemostasis after decellularization and processing steps.

In regards to the decellularization and ECM collection methods described here, we believe that the described platform offers numerous advantages over current approaches to collecting ECM for tissue engineering and research purposes. The bulk majority of clinically utilized and investigated ECMs are sourced from *ex vivo* decellularized organs, typically of porcine or bovine origin [226]. For use in humans, these tissue must be decellularized, rinsed of enzymatic, nucleic and cell membrane residue and terminally sterilized, introducing various harsh factors that alter the ultrastructure of ECM, remove components and denature proteins [227], [228]. The methods described here offer the ability to collect cell-type specific ECM in milligram quantities that has not been exposed to detergents, solvents or sterilization processes, likely offering a more natural and intact ECM. Platforms to collect ECM from individual cell-types offer researchers the potential to deconstruct the complex role of ECM in influencing the host response to implanted biomaterials. A number of recent studies have highlighted that homologous ECM (i.e., ECM derived from the same source tissue it will be implanted) is preferable and maintains tissue-specific cellular responses [189]–[192], [229]–[231].

Towards the goal of studying hemostasis at the device interface, we selected Avitene™ as a candidate ECM to explore the dip coating apparatus due to the fact that it is a clinically utilized neurosurgical hemostat comprised of collagen, the most basic building block of all ECMs [220], [232]. Additionally, Avitene™ is a FDA-approved ECM product readily available world-wide, which would facilitate rapid clinical adoption in comparison to cell-type specific ECMs, which have yet to gain regulatory classification.

4.6 Conclusions

In this study, various ECM proteins were isolated using novel techniques and *in vitro* testing confirmed that such ECMs could potentially be useful as a surface-adsorbed device coating to limit intracranial hemorrhage and the FBR following device implantation. All ECMs tested were observed to show inherent hemostatic capability, similar in effect to the FDA-approved neurosurgical hemostat Avitene™, which was selected as an investigational device coating due to long-standing FDA approval. A dip coating apparatus was developed to deposit ECM on the surface of a high density penetrating microelectrode array. In summary, the methods developed will provide a platform where multiple ECM types can be investigated both *in vitro* and *in vivo* as surface-adsorbed device coatings that modulate the FBR to UEAs.

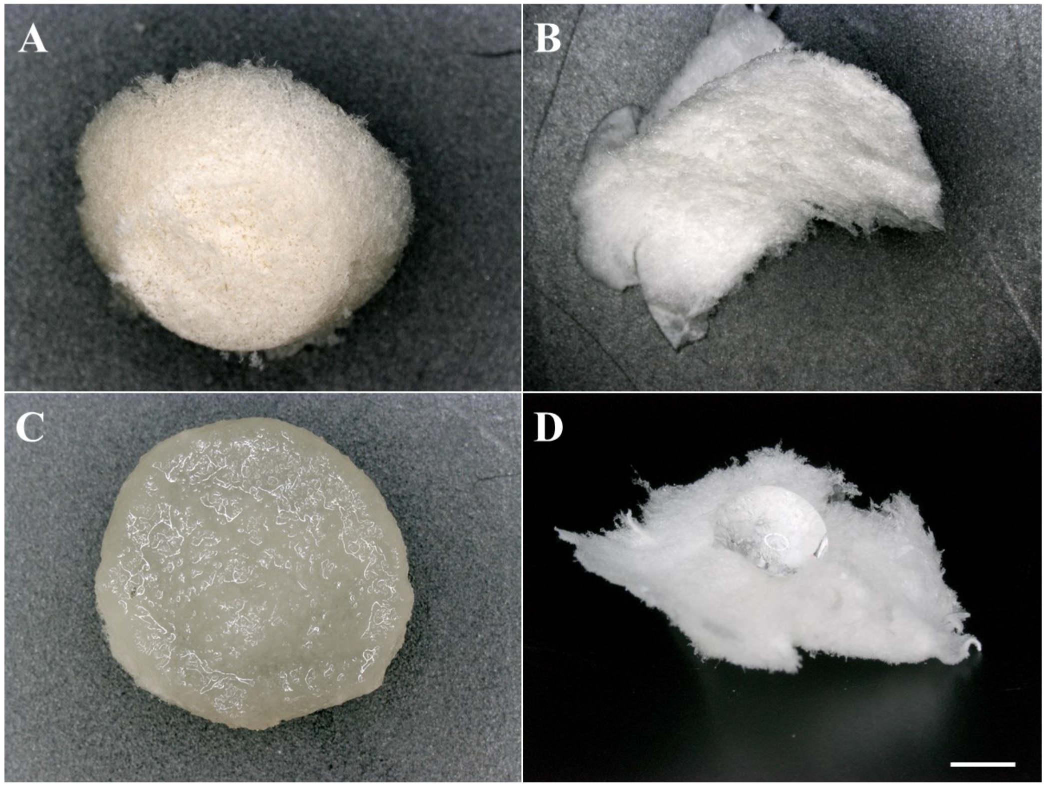

Figure 4.1 Collected ECM. After decellularization and DNAse treatment ECM was scraped from the bottom of culture flasks and lyophilized. A) Representative sample of fibroblast ECM weighing 6.1 mg obtained from 3 T-75 flasks. B) Sample of hMSC ECM obtained from 1 T-75 flask weighing 2.6 mg. C) Fibroblast ECM (same sample as A) readily adsorbed PBS. D) hMSC ECM was hydrophobic and did not adsorb PBS.

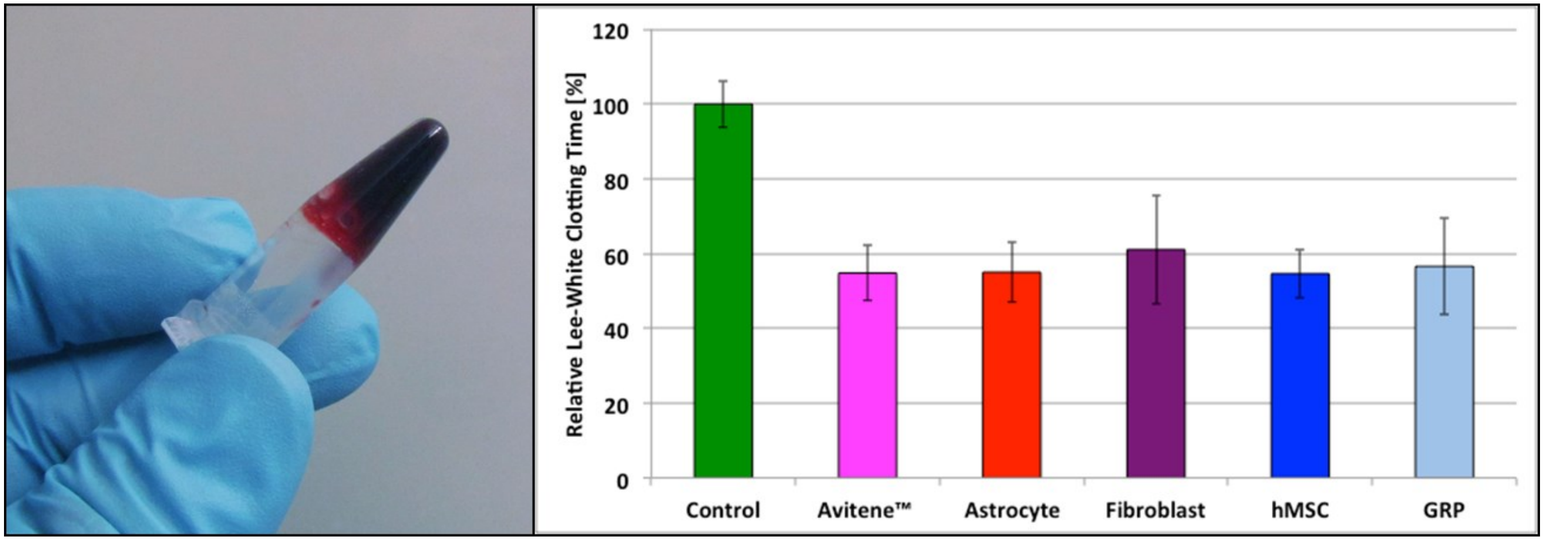

Figure 4.2 Hemostasis Assay. A) Example of a fully coagulated vial, where the blot clot does not dislodge upon inverting centrifuge vial. B) All ECMs tested showed a similar ability to clot recalcified, citrated whole rat blood when tubes were coated with Avitene^{TM}, astrocyte ECM, fibroblast ECM, human mesenchymal stem cell (hMSC) ECM and glial restricted precursor (GRP) ECM.

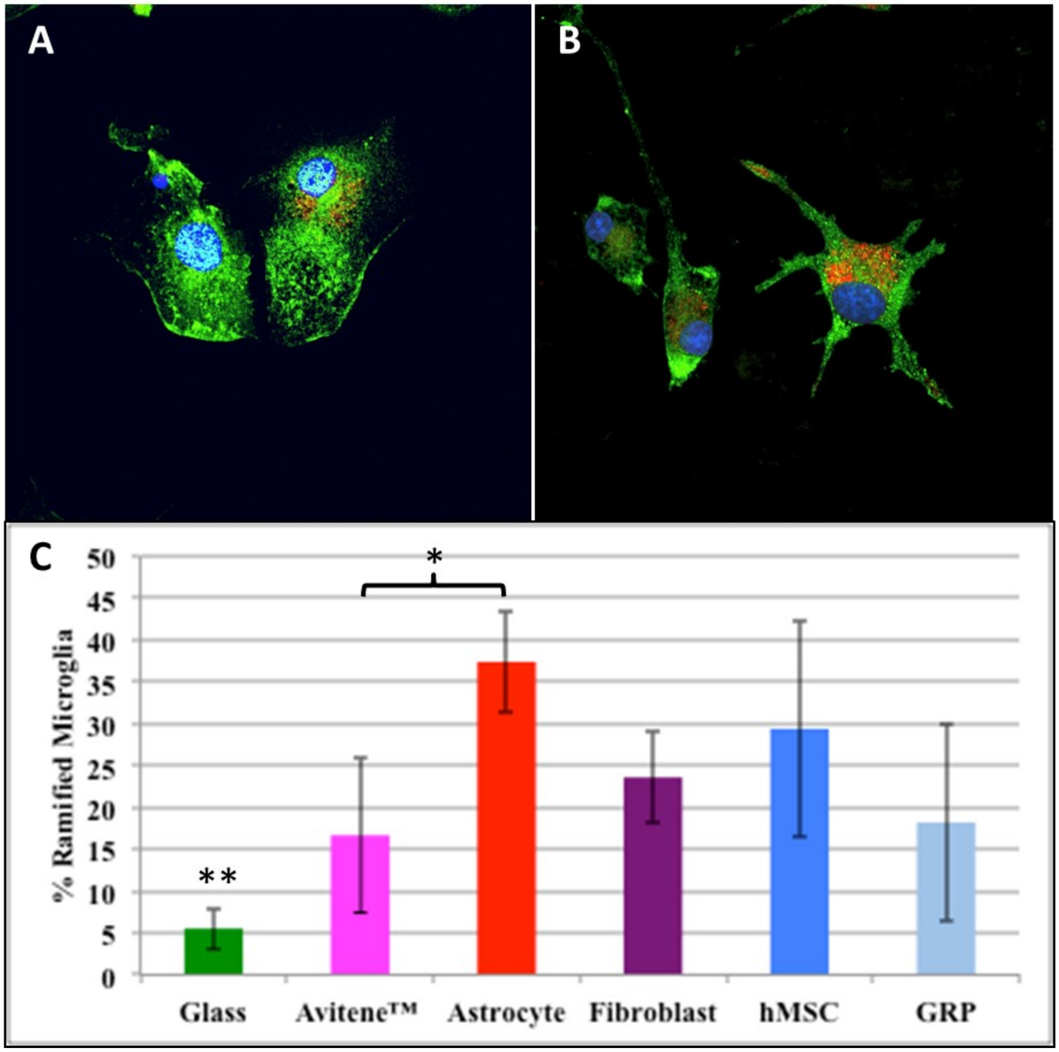

Figure 4.3 Microglia Activation Assay. A) Representative primary rat microglia showing a rounded, or amoeboid, morphology cultured on uncoated glass or B) a ramified morphology on an astrocyte ECM coated glass coverslip. Immunohistochemistry identified IBA-1 (green), CD68 (red) and DAPI (blue). C) Quantification of results expressed as total percent of counted cells that were ramified. (*, denotes a significance difference with $p < 0.05$) (**, denotes a significant difference from all other tested coating with a $p < 0.05$).

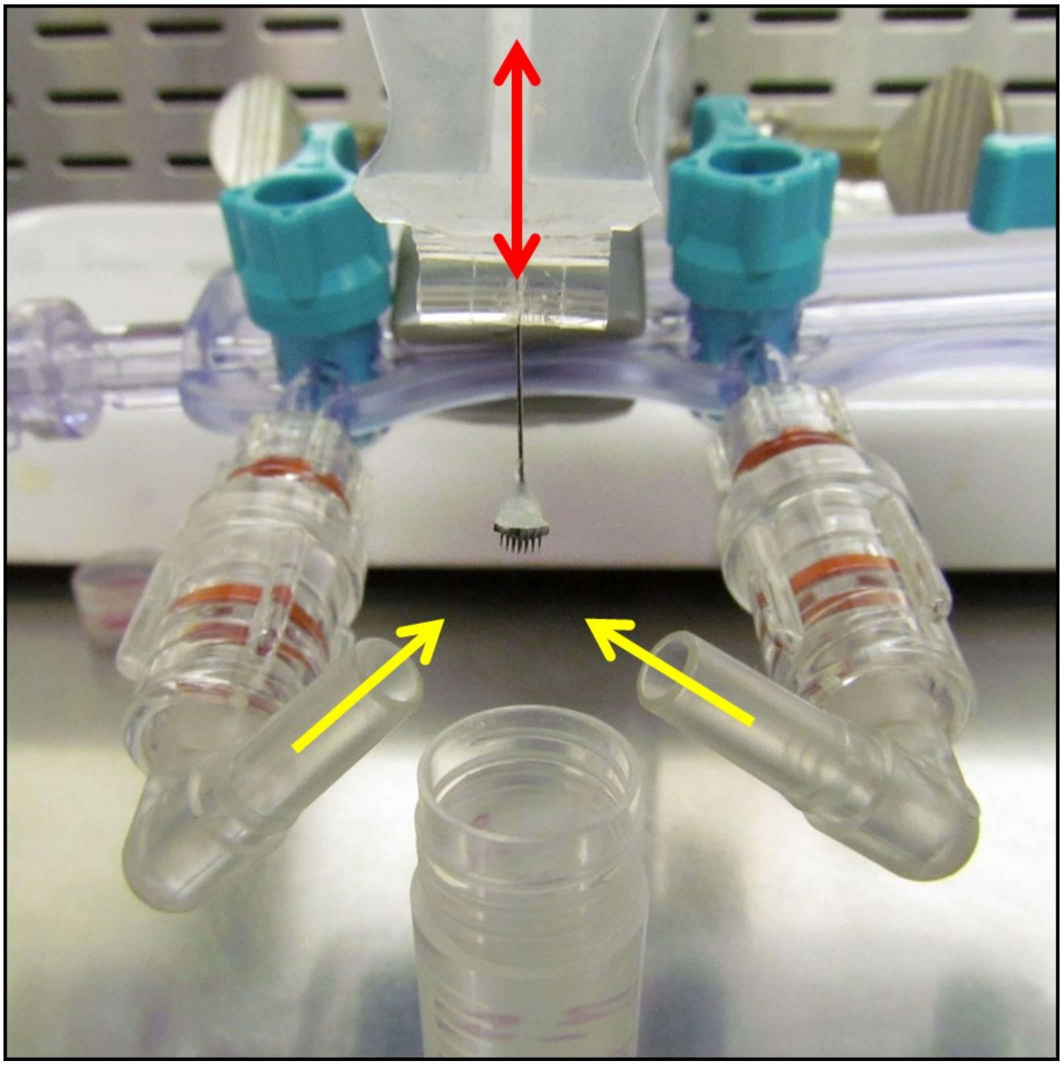

Figure 4.4 Dip coating apparatus. Utah electrode arrays were dip coated in a sterile cell culture hood using a computer-controlled pneumatic syringe (red arrow) to lower device into a protein solution. Sterile nitrogen was blown on the underside of the device (yellow arrows) to ensure uniform drying of the protein suspension onto the surface.

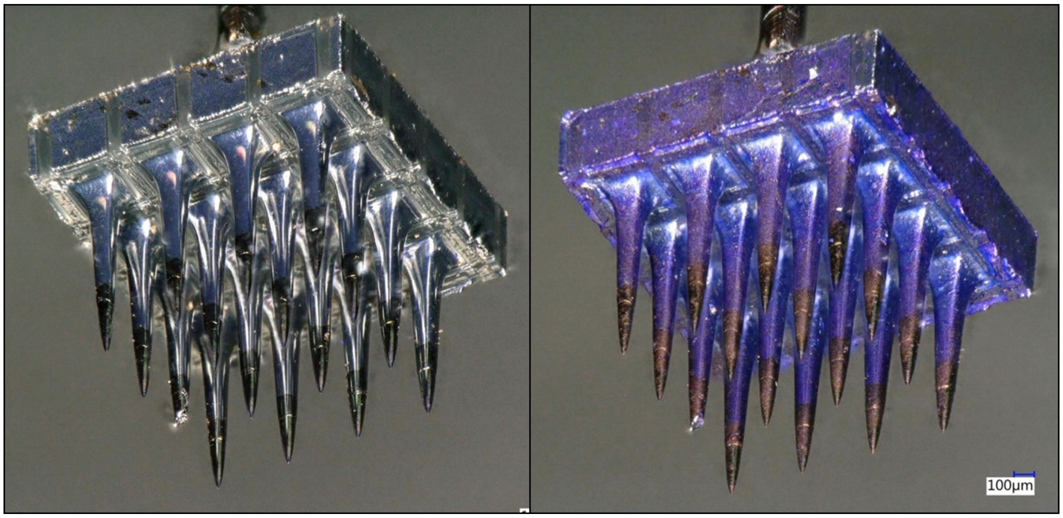

Figure 4.5 Avitene™ coated device. A) To discern from nonspecific adsorption of coomassie blue a cleaned device was first incubated in the ubiquitous protein stain and rinsed 3x and imaged. B) The same device stained after 8 layers of dip coating in Avitene™, and then stained with commassie blue, showing the accumulation of a robust protein layer that conformed to the device geometry. Scale bar 100 µm.

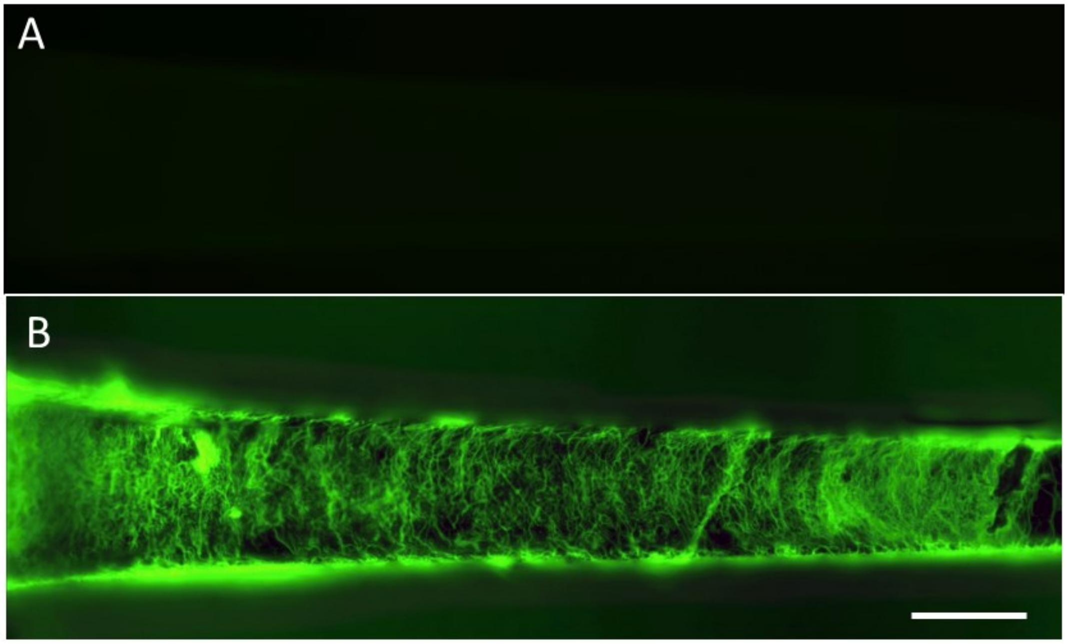

Figure 4.6 Avitene™ immunohistochemistry. A) a coated device was incubated with secondary immunolabel only and showed no unspecific staining. B) a coated device incubated with a primary antibody for type 1 collagen followed by appropriate secondary antibody incubation resulted in specific labeling of device adhered collagen fibrils. Scale bar 100 μm.

Table 4.1 Examples of Avitene™ ECM Components Identified with MS/MS

Component	Description & Role(s) In Wound Healing	Refs
Collagen I • Collagen Alpha-1(I) • Collagen Alpha-2(I)	A fibrillar structural collagen. Supports platelet adhesion from low-to-relatively high shear conditions. Major binding site for Von Willebrand factor. Major ECM component of the glial scar.	[219], [220], [233]
Collagen III	A fibrillar structural collagen closely associated with collagen type I. Supports platelet adhesion from low-to-relatively high shear conditions. Major binding site for Von Willebrand factor. Major ECM component of the glial scar.	[233]
Collagen Alpha-3 (VI)	Largest of the three alpha chains of Collagen VI. Promotes platelet adhesion and thrombosis under low shear conditions. Major binding site for Von Willebrand factor.	[233]
Lumican	A keratan sulfate, small leucine-rich repeat (SLRP) proteoglycan that regulates collagen fibril assembly. Overexpression reduces proliferation of fibroblasts as well as a number of cancer cell lines. Mediates fibroblast contraction during the later stages of wound healing via α2/β1 integrins.	[234]–[236]

Table 4.2 Examples of Astrocyte ECM Components Identified with MS/MS

Component	**Description & Role(s) In Wound Healing**	**Refs**
Collagen VI	A beaded filament forming collagen that promotes platelet adhesion and thrombosis under low shear conditions. Major binding site for Von Willebrand factor.	[225], [237]
Collagen XII	A fibril associated proteoglycan important for proper matrix assembly and mechanotransduction. Also promotes platelet adhesion and thrombosis under low shear conditions.	[225]
Tenascin N & W	Promotes neurite outgrowth and directs neuronal pathfinding. Regulates inflammatory cell migration & activity. Promotes glial proliferation & differentiation.	[238], [239]
Perlecan	A basement membrane-specific heparan sulfate proteoglycan participating in the blood brain barrier. Also promotes tissue regeneration by activating various growth factors.	[240]
Thromobospondin-1	An adhesive glycoprotein that promotes platelet adhesion. Binds to fibrinogen, fibronectin, laminin, and various collagens. Inhibiting neoangiogenesis. Major activator of TGFβ-1.	[241]
Fetuin-A	Plasma-binding protein that is heavily expressed during early brain development. Plays anti-inflammatory and neuroprotective roles in a variety of neurodegenerative disease and injury models. Fetuin can bind TGF-β1 and prevent TGF-β1-mediated signaling and fibrosis.	[242], [243]

CHAPTER 5

IN VIVO INVESTIGATION OF A HEMOSTATIC DEVICE COATING TO LIMIT TISSUE LOSS SURROUNDING CHRONICALLY IMPLANTED MEAS

5.1 Abstract

Cortically implanted UEAs suffer from a limited functional lifespan due, in part, to an aggressive FBR coupled with implantation associated vascular damage that results in lesion cavity formation under implanted devices. It remains unknown how controlling intracerebral hemorrhage after implantation can influence cortical tissue loss following UEA implantation. In this study, we investigate the chronic FBR in Sprague Dawley rats to 4 x 4 UEAs in coated with the FDA approved neurosurgical hemostat, Avitene™, utilized as a surface-adsorbed device coating to limited hemorrhage after implantation. We found that, compared to uncoated control devices, Avitene™ coated UEAs exacerbated all measured metrics of the FBR and resulted in aggressive encapsulation of devices with nonneuronal tissue that entirely excluded devices from cortical contact. The results suggest that xenogeneic type 1 collagen elicited an aggressive FBR in the rat cortex, presumably by activating macrophages, which were found both adhered to device surface, and palisading around implanted electrode shafts. These results imply that tissue source and composition are important considerations when selecting ECM-based strategies for tissue engineering.

5.2 Introduction

Cortically implanted microelectrode arrays are currently utilized in 10 ongoing clinical investigations to provide paraplegic patients with the ability to volitionally control devices such as computers and robotic prosthetics (**Table 1.1**) [2], [66], [67], [71], [72], [202]. Unfortunately these devices do not remain functional for a clinically relevant timeframe and suffer from variable and inconsistent recording [1], [6], [18], [69]. In addition to mechanical failure modes, the foreign body response (FBR) and associated neural tissue remodeling surrounding implanted electrodes has been associated with recording performance deficits [7]. Specifically, it was shown that cortical tissue loss, blood-brain barrier (BBB) dysfunction and astrogliosis occurs under chronically implanted high density penetrating microelectrode arrays implanted in rat cortex and that these metrics correlated with declining recording performance [7]. As such, improving the tissue health surrounding chronically implanted high density MEAs remains a goal in the field of neural engineering.

Acute studies of the histological response to implanted UEAs have indicated that insertion of penetrating microelectrodes causes notable vascular rupture and associated intracerebral hemorrhage (ICH) along electrode shafts and in adjacent cortical tissue [7], [10], [11], [121]. In experimental ICH, injection of minute amounts of blood in the rodent cortex results in vast areas of cortical tissue loss compared to equivalent saline injections [29], [244], [245]. Blood in the brain has been shown to activate brain-resident microglia toward neurodegenerative states [27], [93], [113]–[115], and BBB dysfunction has been implicated in a number of neurodegenerative pathologies [138].

After focal insults such as experimental cortical stab, both meningeal and glial cell types react to clear apoptotic cells, reestablish the blood brain barrier and restore homeostasis in the neural parenchyma. These injuries typically results in the formation of a nonneuronal lesion surrounded by an areas of tapering reactive gliosis and decreased neuronal density [30]–[32], [172], [233]. When studied at 12 weeks postimplant, chronically implanted UEAs also show localized areas of tissue loss under the device. These lesion cavities span multiple electrode shafts and show characteristics of stroke-like lesion cavities including a nonneuronal lesion core that is rich in fibroblasts and activated macrophages and associated collagen deposition, BBB dysfunction, tapering reactive gliosis, and demyelination in surrounding cortical parenchyma (**Figure 3.8**). Earlier studies from our group showed that these lesions form as a result of implant-associated injury, as demonstrated by a stab wound model, where lesion cavity formation was observed 4 weeks implantation and then removal of a 4 x 4 UEA in rat cortex [7]. These studies suggested that strategies that decrease vascular damage from insertion and associated hemorrhage along electrode tracts may positively influence tissue remodeling outcomes and reduce lesion formation surrounding chronically implanted UEAs.

Recently, it has been shown that ECM based hydrogels can attenuate brain tissue loss following cortical contusion models in rodents [36]. Additionally, a number of investigators have used ECM to alter the FBR to cortically implanted single-shank microelectrodes [37]–[40]. To address the issue of intracerebral hemorrhage following implantation we chose to explore an ECM that has already shown clinical utility in the neurosurgical suite as a hemostatic agent. Avitene™ is a bovine-derived primarily type 1 collagen ECM hemostat that is a strong inducer of hemostasis and does so by interacting with platelets via GPVI mediated cell signaling [219], [222], [225]. In remains largely unknown how accelerating hemostasis after device implantation may lead to reduced cystic cavity formation or alter the chronic FBR.

To address this issue, we implanted rats with 4 x 4 UEAs either dip coated with Avitene™ or uncoated control devices and compared the reaction 3 months after implantation. Our results indicate that Avitene™ elicited a severe inflammatory response, characterized by encapsulation of the entire device with granular, inflamed tissue, associated cortical tissue loss and increased in neuroinflammatory FBR biomarkers in the cortex. Control devices also showed cortical tissue loss, FBR biomarkers near the implant and meningeal encapsulation of the device base. In contrast, the majority of uncoated electrode recording sites were located in intact neural tissue. These results show that an adsorbed ECM device coating does indeed influence chronic tissue remodeling outcomes, although in this example we observed the collagen coating to exacerbate surface-adhered macrophage activation state and result in encapsulation of the device in meningeal tissue. Insights gained from this study may prove enlightening to physicians considering the use of Avitene™ in chronic applications, and additionally describe methods to test the ability of future ECM-based device coatings to influence the FBR to many types of devices implanted in the CNS.

5.3 Methods

5.3.1 Microelectrodes

Unwired silicon 4 x 4 UEAs were custom fabricated by the University of Utah Nanofab for this study, as described in Section 3.3. Devices were cleaned and sterilized with ethylene oxide and allowed to out-gas 48 hours before dip coating.

5.3.2 Avitene™ Dip Coating

Avitene™ microfibrillar collagen flour was coated onto device surface using methods described in Section 4.3 (**Figure 5.1**). Devices were observed in sterile packaging and any with aberrant protein assembly on the surface, such as clumps, large fibrils, or spots in coating, were rejected for implant studies.

5.3.3 Animal Surgery

All animal studies were conducted in accordance with the University of Utah Institutional Animal Care and Use Committee. Implantation procedure was identical to the anchored preparation described in Section 3.3.

5.3.4 Tissue Processing and Quantification

All tissue processing and quantification was performed exactly as described in Section 3.3: Methods. In brief, animals were euthanized at 12-weeks postimplant and brains were carefully dissected. Brains and explanted devices were imaged and then brains were cryosectioned and immunolabeled with the antibodies listed in **Table 3.1**. Quantification of neuronal loss area, cystic cavity area, CD68 immunoreactivity and IgG intensity was performed on matched-depth sections and compared statistically across cohorts at each depth. A student's t-test was used to compare means with $p < 0.05$ considered significant.

5.4 Results

5.4.1 Failure Analysis

As is common with the complex requirements of long-term stability in neural recording [1], [7], failure of head stage hardware was an issue noted in both studied cohorts. On average head stages lasted 10.9 ± 0.1 weeks before failure, with no difference between cohorts, and in all cases failure was due to loosening of head stage screws accompanied by osteolysis of cranial bone surrounding screw tips. Removed head stages were often accompanied by removal of the device (except in one control case where the device separated from headstage and remained in neural contact until study endpoint) and rapid recovery of the wound site including skin and fur growth by 7 days after removal of the device. All animals were euthanized at a chronic 12-week time point. In the control cohort, 5 of 7 animals retained their device until the study endpoint, compared to 3 of 7 in the Avitene™ cohort.

5.4.2 Dissection and Gross Observations

At dissection all animals with intact head stages had retained the UEA in its original implantation location. In the control cohort, all devices left in place until study endpoint were observed contacting some degree of cortical tissue. Cortical depression was observed under the device with an average cystic cavity volume of 1.1 ± 0.5 mm^3 as measured from the surface with the Keyence VHX-5000 digital 3D microscope.

In contrast, all Avitene™ coated devices that remained until the study endpoint were not in contact with neural tissue. These devices had fibrotic growth encapsulating the entire device and underside of the head stage. This reaction was accompanied by a large cystic cavity with a volume of 3.4 ± 5.5 mm^3 as measured with the Keyence VXH-3000 3D digital microscope, statistically increased from control ($p < 0.05$) **(Figure 5.2)**.

5.4.3 Explanted Arrays

Upon gross observation, it was observed that both coated and uncoated devices had become integrated with the meninges, with connective tissue continuous with the dura that spanned underneath the base of the device (**Figure 5.3**). In control cases, this encapsulation tissue occupied the upper 1/2 to 1/3 of the electrode shaft, and had a shape that matched the underlying cortical surface depression. Avitene™ coated devices had encapsulation material that extended ~1mm from the surface of the device, entirely embedding devices in encapsulation material. Encapsulation material around Avitene™ devices was more loose and granular than the dense, fibrotic tissue surrounding control devices and often flaked off easily during dissection. In some cases, Avitene™ encapsulation material stayed in the cortical surface depression and was sectioned with tissue.

In the control cohort, encapsulation tissue was highly reactive for IBA-1 and CD68 and showed a majority of DAPI+ cells that were not immunoreactive for either label. Avitene™ encapsulation material had a higher degree of IBA-1 and CD68 labeling and was rich in macrophages that were rounded and appeared to cluster near electrode shafts.

Encapsulation material was dissected to observe cellular attachment to the microelectrode array surface (**Figure 5.4)**. The majority of attached cells in both cases were IBA-1+/CD68+ and in some cases had multiple DAPI+ nuclei, indicating the presence of both activated macrophages and foreign body giant cells (FBGCs). Nearly all IBA-1 cells were immunoreactive for CD68 as well, indicating that the surface of both devices were covered with activated macrophages. It appeared the density of attached cells was higher in the Avitene™ coated devices, but no quantification was performed, as we have observed that device-adherent macrophages can slough off the electrode surface during explant.

5.4.4 Histological Description of FBR

GFAP+ hypertrophic astrocytes create a perilesion perimeter surrounding cystic cavities and lesions [32], and also form tight bands around electrode tracks in neural tissue [3]. Sections were observed at a depth of 450 µm, 650 µm and 1 mm under the base of the device (**Figure 5.5**). The area of lesion tissue was compared at these depths in all animals that had a device until study endpoint. Control animals had significantly smaller lesion cavity area at all three compared depths. Additionally, control animals had visible electrode tracks outside of these cavities and in cortical tissue at a depth of 650 µm and 1 mm, compared to visible cortical contact with any Avitene™ coated electrode shafts.

NeuN loss was compared at a depth of 450 µm, 650 µm and 1 mm under the base of the device. At all compared depths animals with Avitene™ coated devices had a significantly increased area of neuronal loss.

Encapsulation tissue captured within the lesion core was highly immunoreactive for IgG and showed a large number of CD68+/IBA1+ activated macrophages. Around Avitene™ coated electrode shafts, rounded macrophages were observed palisading around indwelling electrode shafts. CD68 and IgG immunoreactivity were increased in the Avitene™ coated cohort at all three compared depths (**Figure 5.6**).

Vimentin immunolabeling was observed within the hypercellular lesion core with higher density towards the lesion border (**Figure 5.7**). SHG imaging showed fibrillar collagen within the lesion core tissue, but not in the cortical parenchyma.

5.5 Discussion

In this study we provide evidence that 4 x 4 UEAs coated with Avitene™ show a pattern of changes in cortical and meningeal tissues after implantation that is different than that observed for the same devices that are uncoated. These changes include increased levels of fibrotic encapsulation, increased cortical surface tissue loss, a larger surface cavity under the device, increased BBB disruption and neuronal loss at all compared depths. Similar to a previous study with single-shank microelectrodes [40], Avitene™ as a surface-adsorbed device coating did not improve the biological response and elevated markers of neuroinflammation.

A number of studies have identified intracerebral hemorrhage (ICH) as a consequence of acute implantation of UEAs in the highly vascularized cortex [7], [10], [11], [98]. Studies of IHC in rodents have shown that secondary to experimental IHC caused by injection of whole blood into the brain, brain tissue loss is increased an order of magnitude compared to equivalent saline injections [29]. In this study, we observed cortical tissue loss under uncoated devices, consistent in shape and size with what has been reported previously under 4 x 4 UEAs in rat cortex [7]. Although Avitene™ showed utility to accelerate hemostasis in an *in vitro* model (**Figure 4.2**), cortical tissue loss was greatly exacerbated in the Avitene™ cohort at the chronic time point observed (**Figure 5.2**). This indicated that Avitene™ may have more diverse biological effects than previously speculated.

GFAP immunolabeling identified regions of cortical tissue loss, as GFAP+ hypertrophic astrocytes are known to form a tight band around the edges of lesions [151]. In control animals, these cavities had a similar pyramidal shape to those observed by Nolta *et al.* [7], with the area of the cavity decreasing with increasing depth into the cortex. Avitene™ coated devices resulted in significantly larger lesion cavities that were more spherical in appearance and extended both wider and deeper into the cortical tissue. Lesions were accompanied by an equivalent size mass of fibrotic tissue that entirely encapsulated the device.

IgG is a plasma protein that is normally excluded from the brain by the BBB, positive immunolabeling in cortical tissue indicates a leaky BBB and persistent, ongoing inflammation [246] and is often observed around chronically implanted devices [7], [90], [91], [106]. CD68 is a lysosomal protein utilized to indicate macrophage activation, associated with proinflammatory cytokine secretion and persistent neuroinflammation [93], [247]. Elevated levels of both labels under the Avitene™ coated devices are indicative of an enhanced inflammatory reaction in response to the device coating. As the initial vascular insult was comparable in both cohorts, this data suggests that over the time course of implantation the Avitene™ surface recruited a larger number of macrophages and that their subsequent activation and recruitment induced a higher degree of BBB disruption. Indeed, a number of emerging studies point toward macrophage trafficking and activation as contributors to BBB breakdown following injury [27], [115], [116]. These results are also in line with a recent study where Avitene™ coated single-shank microelectrodes were compared to uncoated and showed statistically elevated IgG in the Avitene™ coated devices at 12-weeks post implant [40].

When observing explanted MEAs in rodents, felines and primates it has been noted that the base of the device becomes encapsulated in fibrotic material and it has been speculated that this reaction leads to separation of the device from cortical contact [1], [7], [12]–[14], [121]. This was also observed in our study, where all control devices had a layer of fibrotic material adhered to the base. Furthermore, when coated with Avitene™ the amount of fibrotic encapsulation was significantly increased, resulting in complete encapsulation of the device that excluded any Avitene™ coated devices from obtaining cortical contact at the study endpoint. While this tissue was continuous with the dura, it had a much more loosely associated than control encapsulation material and had an inflamed appearance, rich in activated macrophages. A number of short-term studies of implanted ECM in the CNS to treat focal cerebral insults have shown that macrophages extensively infiltrate implanted ECM [188], [248]–[250]. It has also been shown that homologous ECM is preferable to maintain tissue-specific cellular phenotypes and wound healing responses [189], [190], [192], [230], [231], [251]. Additionally, a number of studies have shown that macrophage phenotype is an important predictor of the tissue response to implanted biomaterials [192], [210], [212], [213], [248], [252]–[254]. Collectively, these results suggest that Avitene™ ECM signaled a fibrotic wound healing response that resulted in persistent macrophage activation and deposition of nonneuronal tissue around the implanted devices.

This encapsulation material stained positively for vimentin, and collagen deposition was noted, presumably indicating the presence of fibroblasts in encapsulation material. This could have been due to the fact that Avitene™ is comprised of collagen, which is normally present in the meninges, but absent in cortical tissue [31]. While the exact nature of this tissue is difficult to determine, this evidence suggests that an aggressive meningeal-origin FBR was directed toward the Avitene™ coating.

Supporting evidence for these findings can be found in clinical literature describing the FBR to chronically implanted Avitene™. In spite of FDA approval as a neurosurgical hemostat, clinical case reports have reported severe necrotizing granulatomous inflammation in response to Avitene™ left in the brain chronically [255]–[261]. Case studies have shown that, in some patients, Avitene™ elicits a strong inflammatory response, including palisading macrophages, hypercellarity, fibrotic masses and an “exuberant inflammatory reaction directed against the foreign material [that] sometimes creates a space-occupying mass [256].” Product inserts that accompany Avitene™ packaging warn against a FBR reaction to Avitene™ left in the brain, and indicate that excess material should be rinsed away from application site with saline after hemostasis has been achieved. While this reaction has been noted, it is important to note that all of these papers indicate that a FBR (or textiloma as this response is referred to clinically) in response to Avitene™ is a very infrequent occurrence, likely dependent on a subject-specific immune response. Studies of hypersensitivity to injected subcutaneous bovine collagen have showed that immunogenicity to bovine collagen exists in 3 – 5 % of the general population [262]–[265]. Whether this response was strain-specific to SD rats utilized in this study, remains unknown.

5.6 Conclusion

In this study we provide evidence that Avitene™ coated MEAs induced a heightened foreign body response (FBR) compared to uncoated control devices. When the coated device was left in place, a severe inflammatory reaction was observed as indicated by larger cavities, enhanced fibrotic growth, decreased neural density under device, elevated levels of activated macrophages and enhanced BBB leakiness. These characteristics would indicate that the Avitene™ device coating served to exacerbate the negative characteristics of the known FBR to implanted UEAs. We show that Avitene™

aggravates macrophages at the device surface and that this reaction drives an aggressive meningeal encapsulation response that entirely excludes devices from neural contact. These results suggest that surface bound macrophages and their activation state may be responsible for meningeal encapsulation that drives device rejection. Although Avitene™ negatively impacted the FBR, this study provides evidence that a surface bound ECM coating is sufficient to significantly alter the FBR to chronically implanted UEAs.

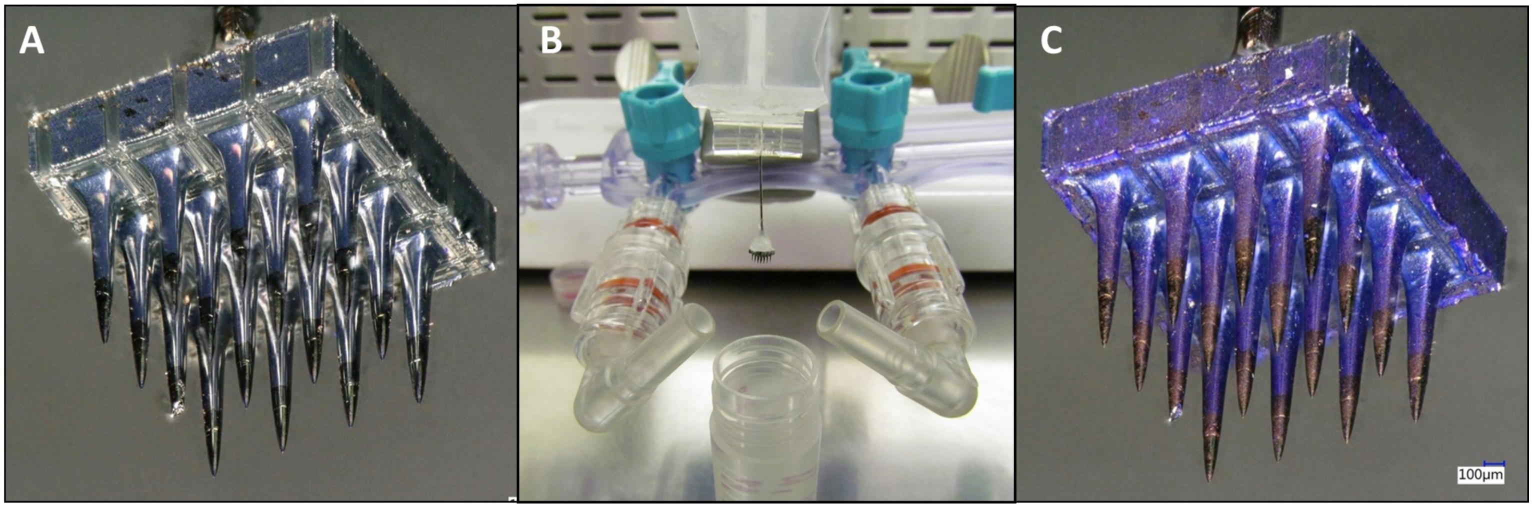

Figure 5.1 Avitene™ dip coating process. A) An uncoated device that has been incubated in coomassie blue, showing no protein attachment. B) A dip coating apparatus worked by pneumatically lowering electrode into a sterile solution of suspended Avitene™ (1 mg/mL) and then uniformly drying protein to the surface with sterile nitrogen streams from below the device. C) After 8 repetitive dip coats, comassie blue staining was repeated and showed the presence of a continuous protein layer on the surface of the device. Scale bar A & C - 100 µm.

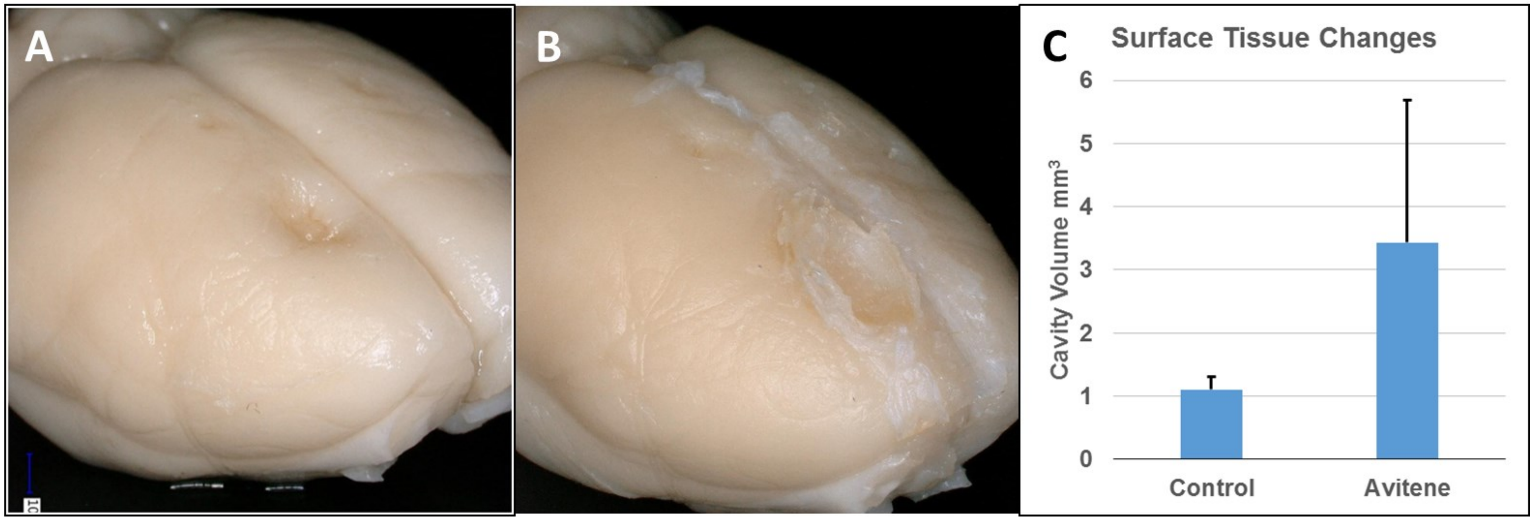

Figure 5.2 Surface tissue changes measured by 3D surface topology. A&B) Representative images of brain surface after explant or device. A) Animals implanted with control devices showed a loss of cortical tissue under the device. B) Animals implanted with Avitene™ coated devices also had large cortical surface depressions that were filled in with dural material. C) After removal of this dural material surface tissue changes were calculated by 3D surface topology and showed a larger loss of surface tissue in Avitene™ coated animals.

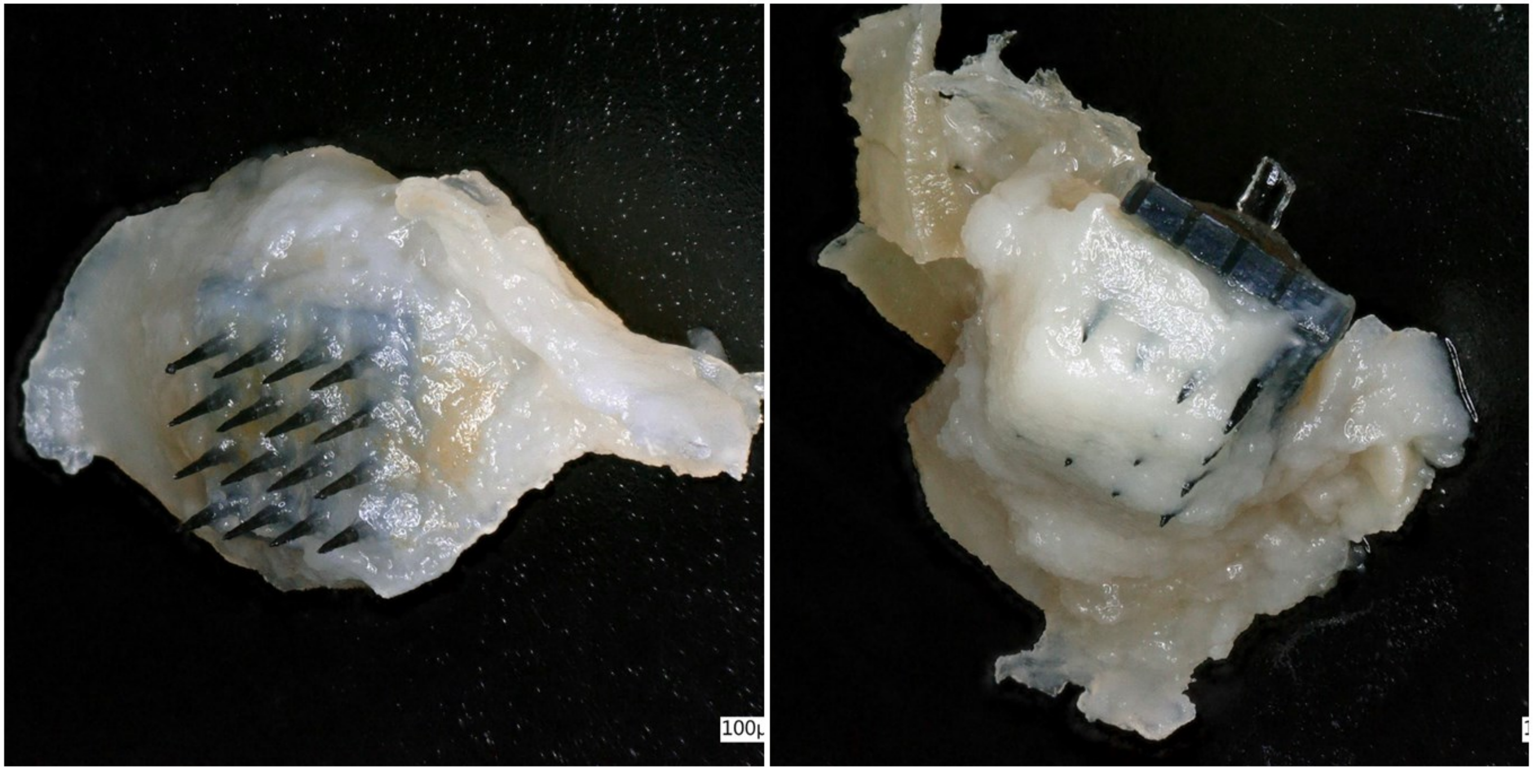

.

Figure 5.3 Explanted devices. Left) Upon explant, control devices were found firmly integrated with connective tissue that spanned the base of the device, often occupying the upper third to half of the electrode shaft. Right) All Avitene™ coated devices were entirely encapsulated with connective tissue that was continuous with the dura, but had a more granular appearance than the encapsulation material observed around the base of control devices. Scale bar 500 µm.

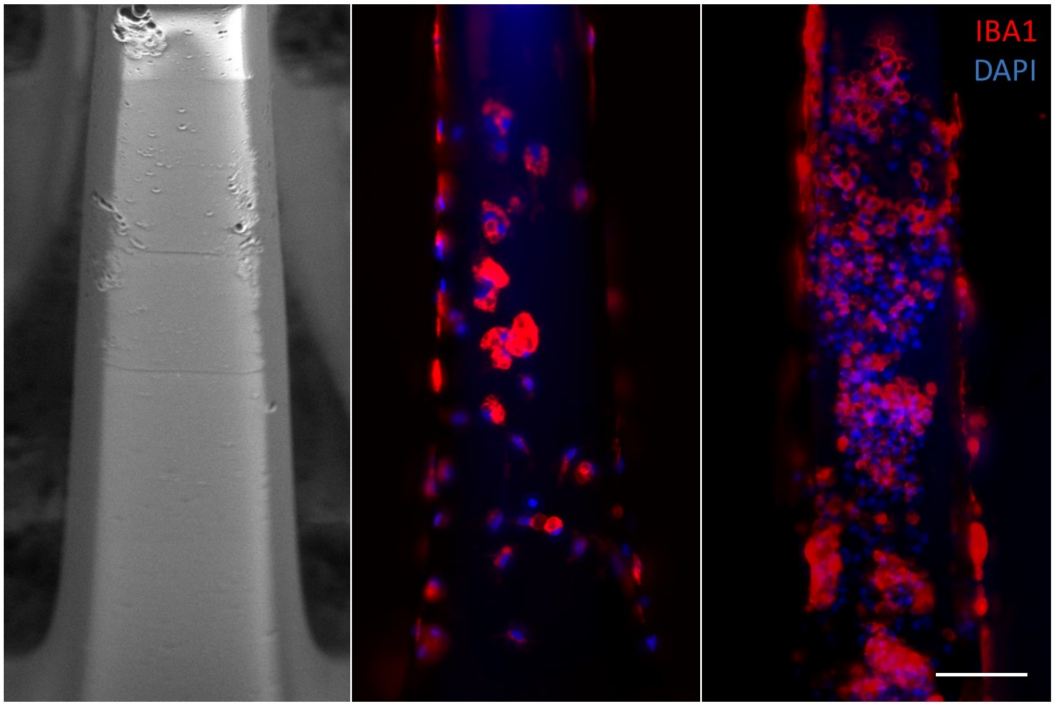

Figure 5.4 Cellular attachment to microelectrode shafts. Left) SEM image of a control, unimplanted microelectrode shaft, small ripples in the Parylene-C coating can be observed. Encapsulation material was removed from the device to observe cells on the surface, labeled with NeuN (red) and DAPI (blue). Scale bar 50 µm. Middle) An uncoated electrode shaft after 12-week implant, showing rounded IBA1+ cells attached to the surface. Right) An Avitene™ coated electrode shaft with a much higher degree of cellular attachment and multinucleate FBGCs towards the bottom of the shaft. Scale bar 50 µm.

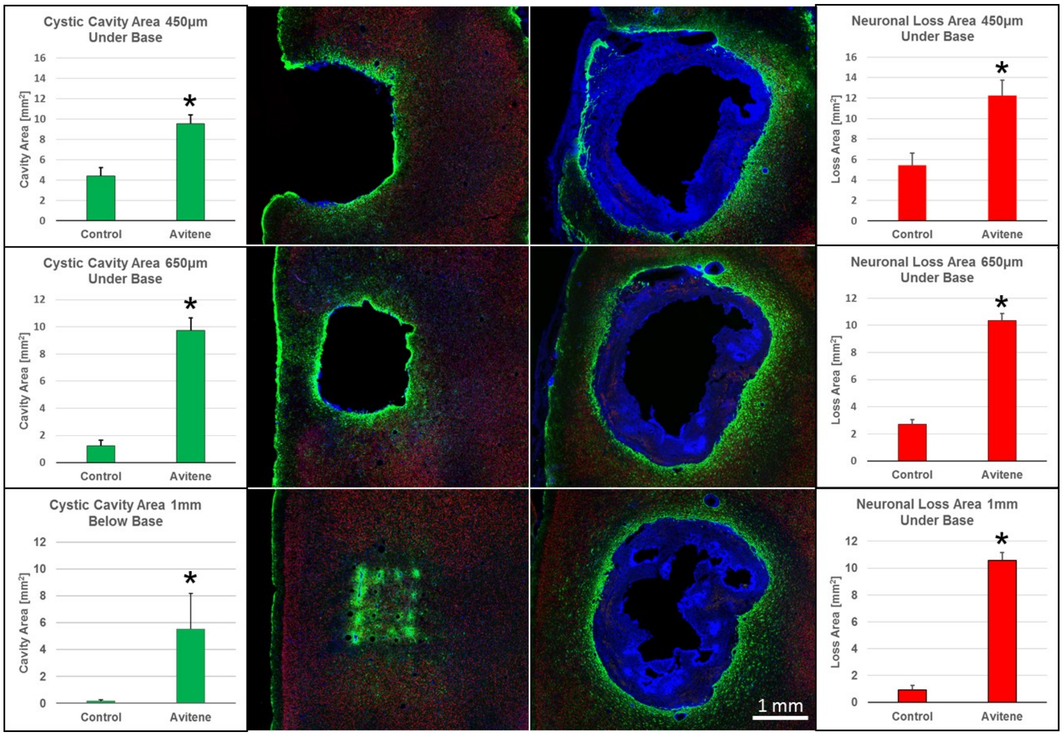

Figure 5.5 Cavity area and neuronal loss compared at 3 depths. (1st Column) Cystic cavity area was compared at depths of 450 µm, 650 µm and 1 mm under the base of implanted devices, and was significantly increased at all depths in the Avitene™ coated cohort. (2nd Column) Representative histology showing DAPI (blue), GFAP (green) and NeuN (red) from animals implanted with (2nd Column) Control or (3rd Column) Avitene™ coated devices. In the Avitene™ coated device it is observed that the cavity is mostly filled with hypercellular tissue that does not label for GFAP or NeuN, indicating the nonneuronal nature of this tissue. (4th column) Neuronal loss was compared at all three depths and showed a significant increase in Avitene™ cohort at all measured depths (*, $p < 0.05$). Scale bar 1 mm.

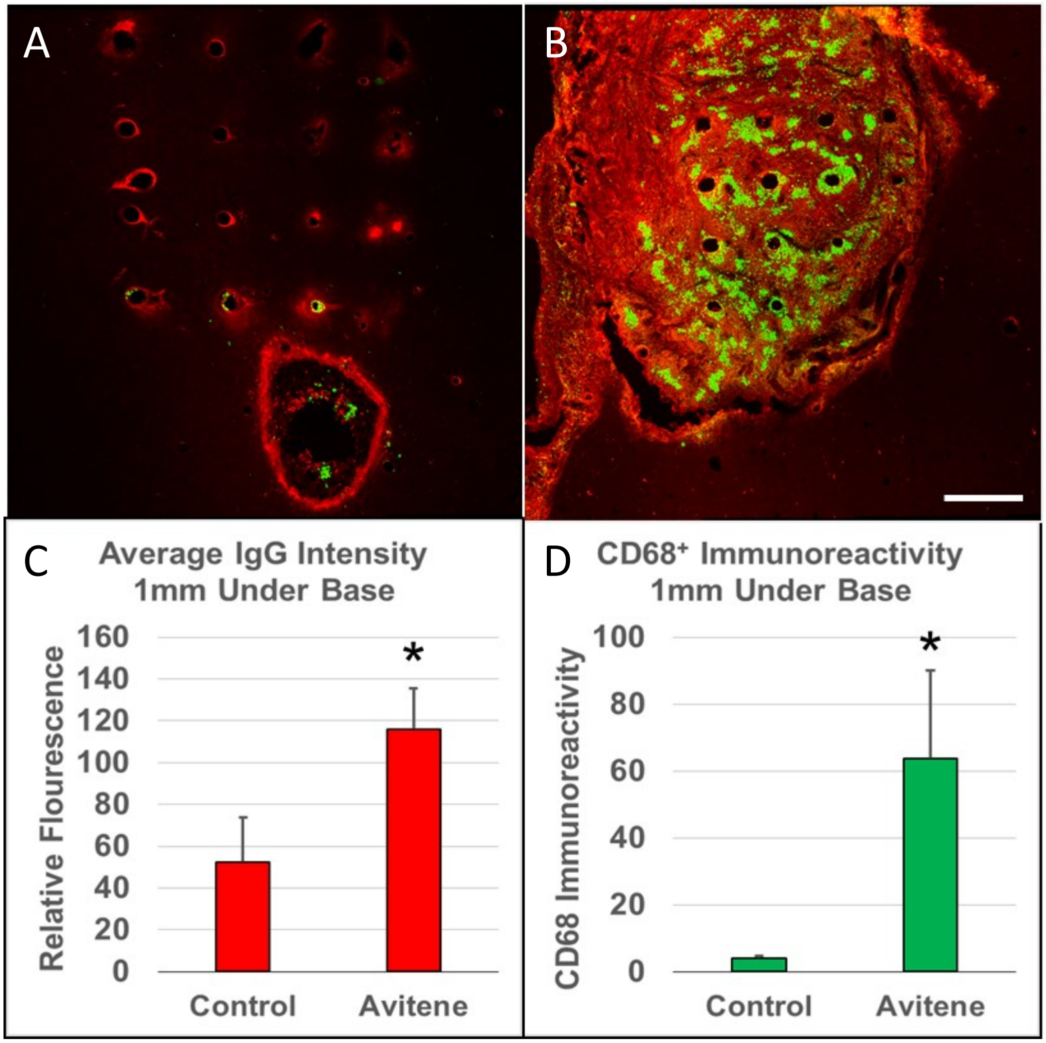

Figure 5.6 Blood brain barrier dysfunction and macrophage activation. A&B) Representative images showing IgG (red) and CD68 (green) at a depth of 1mm below the base, near the recording tips. A) Control implanted animals showed IgG accumulation near the electrode tips and lining the lesion cavity. B) When implanted with Avitene™ coated devices, the cavity filled in with fibrous tissue that was IgG positive. Activated macrophages can be seen palisading around electrode shafts with a particularly high density within lesion core tissue. C&D) Quantification showed that immunoreactivity was increased for both markers in animals that received Avitene™ coated implant (*, $p < 0.05$). Scale bar 500 μm.

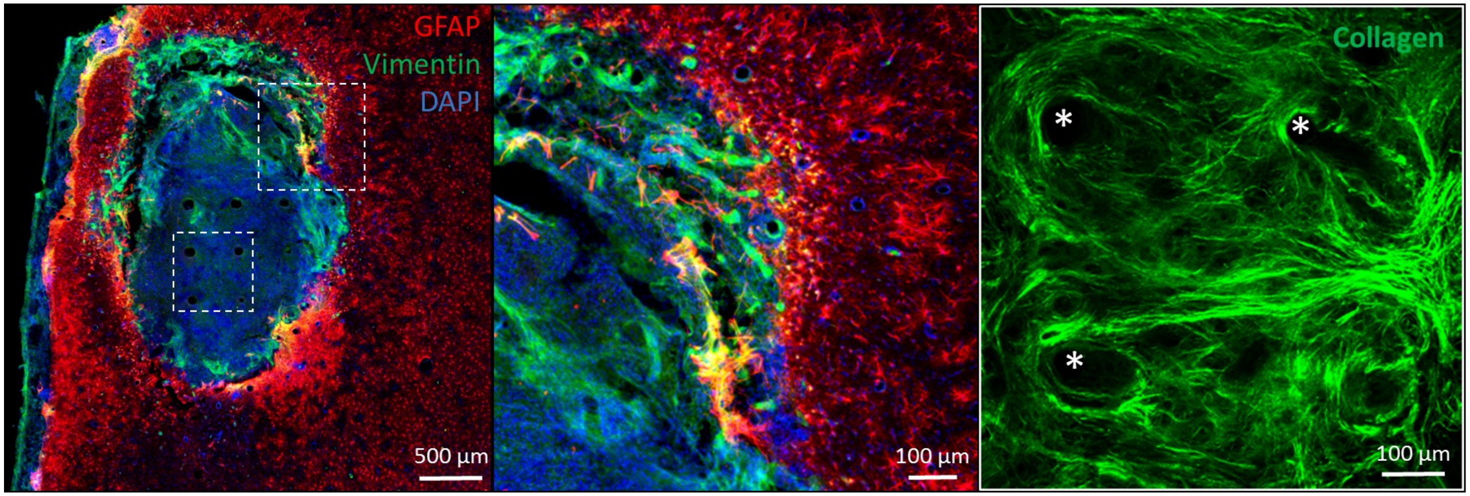

Figure 5.7 Presumptive fibroblasts line lesion cavity. Left) Section located near the tips of an Avitene™ coated device showing GFAP (red), Vimentin (green) and DAPI (blue). Scale bar 500 µm. Middle) Close up shows that Vimentin+/GFAP- cells line the lesion cavity and interact at the lesion border with GFAP+ astrocytes. Right) Second harmonic generation imaging confirms the presence of fibrillar collagen within this lesion cavity (* indicates presumed electrode locations). Scale bar 100 µm.

CHAPTER 6

CONCLUSIONS, LIMITATIONS AND FUTURE WORK

This dissertation set out to address the hypothesis that strategies that minimize the FBR, device movement and tissue loss will lead to improved biocompatibility of implanted UEAs. The hypothesis was addressed with 2 animal studies that have each enhanced our knowledge of the FBR's effect on implanted UEAs. Additionally, insights generated from this work will facilitate the further study of methods to improve the biocompatibility of UEAs, as discussed in the future work section. While a long road remains for seamless integration of high density intracortical microelectrodes, this work will inform the design of next generation recording devices that may one day change the standard of care for motor control disabilities.

6.1 Conclusions

Collectively, these independent studies enhanced our knowledge about ways to influence the FBR to implanted high density recording devices. Of the available studies of the FBR to UEAs, these are of the first to focus on altering aspects of the FBR with a goal of enhancing device integration, and thus, biocompatibility. This dissertation questioned whether simple improvements in device anchoring or application of a neurosurgical hemostat could decrease the FBR to UEAs. Additionally, a number of *in vitro* techniques were developed that will further facilitate development of ECM-based strategies to reduce the FBR.

In Chapter 3, we investigated the effects of anchoring strategies on the FBR to UEAs. We concluded that unanchored UEAs do have a decreased FBR, but at the expense of device movement away from implantation target. This study highlights device movement as an important variable that would not allow freely floating UEAs to record from stable populations of neurons over time. It was concluded that implantation associated tissue remodeling around a chronically implanted, unanchored, UEA is sufficient to change its orientation, even in the absence of meningeal encapsulation. This study highlighted a need for strategies that can limit implantation associated damage and subsequent cortical tissue remodeling in order to improve limit device migration.

Chapter 4 explored ECM based device coatings as a means to modulate implantation associated injury and the FBR to high density devices like the UEA. While ECM has shown utility as a surface adsorbed device coating in numerous soft tissues, very limited studies have investigated such an approach to improve biocompatibility of devices implanted in the CNS. This study concluded that single cell sourced ECM could be reliably obtained using a simple, repeatable process, allowing exploration of intact ECMs derived from a variety of single-cell sources. This technique may prove invaluable in future studies of ECM-based tissue engineering by allowing investigation of ECM from a homogenous cell population. Such an approach for ECM isolation may help elucidate mechanism of action behind ECM's proven regenerative potential. *In vitro* assays demonstrated that ECMs were capable of influencing coagulation and macrophage activation, indicating that surface-adsorbed ECM may have potential as a bioactive device coating. Exploration of ECM as a device coating to improve the FBR was facilitated by designing a dip coating apparatus that will enable further studies of ECM as a device coating.

Chapter 5 is the first ever study of ECM as a device coating for UEAs. We found that xenogeneic type I collagen is not an ideal candidate for improving biocompatibility of CNS devices. While a large body of literature has indicated that ECM improves the host response to implanted materials, this study showed xenogeneic, collagen-based ECM has the potential to exacerbate the FBR. Avitene™ coated electrodes enhanced the meningeal aspect of the foreign body response, allowing exploration of aggressive meningeal encapsulation as has been reported in larger primates. Avitene™ coated devices were surrounded by large fibrotic masses that displaced all cortical tissue surrounding the device. This response was likely exacerbated by the large number of device adherent and palisading activated macrophages, again highlighting the importance of controlling activation state of such cells. It remains to be determined if other ECM-based device coatings can positively influence the FBR. However, this study shows that surface adsorbed ECM device coatings are capable of influencing the chronic response to implanted devices.

6.2 Limitations

The contribution of these studies can only be fully appreciated by understanding their limitations as well. One important limitation is the size disparity between rodents and humans; understanding the species specific differences in cortical architecture can improve interpretation of results. Chapter 3 explored the difference between anchored and unanchored arrays, but the presence of a headstage in anchored animals could have complicated understanding. Chapter 4 explored ECM-based device coatings, but further steps could be taken to assure safety and efficacy of such coatings, as would be required by the FDA. Chapter 5 investigated is a hemostatic ECM could improve the chronic FBR, but it would be useful to determine if the ECM coating was in fact hemostatic in the acute setting. These limitations are expanded below and, in the next section, experiments are designed to address these limitations.

The 4 x 4 UEAs studied are 16 % the implanted volume of those utilized in human studies, while the rodent brain is 0.2 % the volume of a human brain. This means the device occupies 80 times more of the total brain volume in a rodent than it would in a human, which would very likely lead to a comparatively much more severe inflammatory response due to limited space for diffusion of inflammatory signals generated at the device interface. Studies in feline and NHP models typically report lesion cavity formation less frequently, although granular, friable tissue near the center electrodes has been reported in both models [14], [120]. Remarkably, cortical depth and vascular density are relatively conserved across species (See **Table 2.4** and Section 2.4 for a summary of similarities), and so are the hallmark characteristics of the CNS FBR (Section 2.3). These similarities indicate that the rodent cortex could be a viable test bed for exploring methods to alter the CNS FBR to UEAs

In Chapter 3, unanchored devices were compared to those anchored to the skull, but contributions of the FBR to headstage components was not controlled for. In the anchored preparation 4 cranial bone screws were placed in the rodent skull, while unanchored devices had no such securement. Upon explant it was noted that 70 % of these screws protruded through the skull and caused a cortical surface depression. This indicates that a FBR to screws may have been acting in concert with the FBR to implanted UEAs. In support of our chosen experimental setup, it has been reported that implants separated by > 1 mm in the rodent cortex do not affect each other [266]. The screws utilized in this study were all located > 10 mm from the implant, so it is likely that they did not affect the FBR observed at the device interface. In order to understand how anchoring affects the FBR to UEAs in the absence of headstage components, an experiment has been designed in Future Work Aim 1 to explore how the meninges could be utilized to anchor devices using a less evasive approach.

In Chapter 4, a device coating approach was developed where cell type specific ECM was harvested and explored for hemostatic and immunomodulatory potential. While these tests provide useful information on the bioactivity of such coatings, basic biocompatibility testing was not explored. In order to create a translatable device coating, FDA regulations are important to consider. Primarily, it would be important to perform some basic *in vitro* tests as outlined in "ISO 10993: Biological Evaluation of Medical Devices". Although many of these tests are applicable, it would be prudent to start with test that, if failed, would determine that ECM was not safe for use in humans. In particular, an important first step would be cytotoxicity testing against human fibroblasts, as outlined in ISO 10993-5: Tests for *In Vitro* Cytotoxicity. Two such test are outlined in Future Work Aim 2.

In Chapter 5, a hemostatic ECM was used to address concerns of intracranial hemorrhage associated with device insertion. While we determined that Avitene™ did not improve the FBR at chronic time points, it remains unknown if the hemostatic coating actually did serve its intended purpose of accelerating hemostasis at the device interface. The focus of these studies was on improving the long term stability of recording interfaces, so short-term improvements in the response were not assessed. Towards the goal of studying other ECM-based device coatings, it would be helpful to understand if a surface adsorbed ECM can accelerate hemostasis in the acute setting. The question as to whether Avitene™ accelerated hemostasis at the device interface and has been addressed with a 24-hour implantation study, outlined in Future Work Aim 3.

6.3 Future Work

In this future work section, we address study limitations using a hypothesis based approach to design experiments that could further improve our understanding of the unaddressed questions highlighted in the limitations section. Proposed work is outlined in a fashion similar to a NIH R01 application, where background, methods and expected outcomes are discussed. In Section 6.6 preliminary experimental work has been completed and is presented as preliminary data to prove the feasibility the approach. The goal of this section is to inspire further work by providing rationale and methods to carry out continued investigation of ways to improve the biocompatibility of chronically implanted high density penetrating microelectrode arrays.

6.4 Future Work Aim 1: Determine if the Meningeal FBR Can Be Utilized to Stabilize Device Movement

6.4.1 Background

This dissertation indicated that unanchored devices suffer from concerns of device movement from intended recording zones. Compared with UEAs rigidly affixed to the skull with cranial bone screws, such freely floating UEAs had a decreased FBR and also had significantly less meningeal encapsulation, but were also observed to move away from implantation site. These results indicate that UEAs could benefit from some sort of anchoring, ideally in a less evasive manner than the 4 cranial bone screws utilized to secure devices in these studies.

ECoG arrays, which sit on the dural layer and record electrical activity, also suffer from aggressive meningeal encapsulation which separates the device from cortical contact over chronic implant durations [267]–[269]. One strategy that has shown promise to reduce this fibrotic tissue buildup is with ECoG arrays that have a more open architecture, allowing fluid and tissue passage through openings in the flat substrate [270], [271]. One study in rats compared solid versus open architecture ECoG arrays and observed that EGoG arrays with a more open architecture allowed encapsulation tissue to grow up through the device. This open architecture resulted in fibrotic encapsulation, but with much less tissue buildup on the underside of the device compared to a planar device with no perforations [270]. These results indicate that a more open architecture of the UEA base may lead to improved integration of devices with meningeal tissue, and may provide a means for harnessing meningeal encapsulation to anchor devices in place.

In this aim, we explore how changes in the architecture of the UEA base could potential influence the FBR and device orientation. In particular, we intend to explore strategies to direct meningeal tissue growth in a constructive manner, ideally integrating devices with the meninges to maintain electrode position over a chronic implant duration.

6.4.2 Methods

UEAs will be custom fabricated at the University of Utah Nanofab. Electrodes will be manufactured as described in Chapters 3 and 5, with a 4 x 4 grid of 1 mm long microelectrode shafts. Open architecture UEAs will be fabricated by using the focused ion beam to tunnel a 3 x 3 grid of 100 μm diameter holes, centered between electrode shafts, which run from the base of the device to the backside. These holes will be created before devices are coated with Parylene, so as to keep surface chemistry matched in control and open architecture UEAs.

Implantation procedure will be carried out as described in Chapter 3, using the methods for unanchored preparation. After a 12-week indwelling period animals will be terminally perfused and brains carefully dissected so as to leave the electrodes in place. Using the device tilt measurement methods developed in Chapter 3, the tilt angle and device extraction will be measured for each group. Using Equation 4 in Chapter 3 these geometric measurements will be calculated to display the average absolute displacement from implantation target. Histological analysis will evaluate the distribution of FBR biomarkers, as described in Chapter 3 and 5. Means will be compared statistically using a student's t-test with $p < 0.05$ considered significant.

6.4.3 Expected Outcomes

The base of chronically implanted UEAs suffer from fibrotic encapsulation that, at times, is so thick that electrodes are entirely excluded from neural contact. When this meningeal encapsulation is thin, devices can function for periods out to years, indicating that reductions in this encapsulation thickness are desirable. ECoG arrays suffer from similar dural encapsulation that eventually moves electrode from cortical contact, and one approach that has mitigated this response is the introduction of an open architecture design that allows tissue growth through the array [270]. We expect that open architecture UEAs will integrate with meningeal tissue, likely in a similar fashion to open architecture ECoGs, where dural tissue grows on both sides of the device base.

It has been observed that connective tissue regrowth occurs as soon as 7 days post implant [270], so we expect these devices to be integrated with the dura before tissue remodeling (which occurs on a scale of weeks to months) moves devices from implantation target. We expect the unanchored cohort to migrate heavily from implantation target, as was observed in Chapter 3, but also to have little to no meningeal encapsulation. Compared to the meningeal encapsulation response typically seen around anchored devices, we predict that open architecture UEAs will have a thinner layer of encapsulation tissue under the base that does not extend as far down the shaft.

Because we are encouraging meningeal growth, we also expect that the FBR will be increased around open architecture devices. This is due to the observations made in this dissertation that devices with increased encapsulation tissue have larger areas of tissue loss and elevated markers of the FBR. However, in comparison to rigidly anchored devices, it is expected that dural anchoring may minimize micromotion induced tissue damage (see Section 2.7) by anchoring devices to a more compliant tissue than bone. We expect that similar strategies that can direct meningeal tissue growth will lead to improvements in long term stability of freely floating arrays.

6.5 Future Work Aim 2: *In Vitro* Cytotoxicity Testing of ECM

6.5.1 Background

In Chapter 4 we developed *in vitro* screening assays to quantify the hemostatic and immunomodulatory properties of commercially available and in-house harvested ECMs. Due to longstanding FDA approval of Avitene™ as a neurosurgical hemostat, it was selected in spite of evidence that astrocyte-derived ECM was more capable at modulating macrophage activation state towards a proregenerative phenotype. While cell-type specific ECM has shown tremendous potential to modulate the FBR as a surface adsorbed device coating, no studies to date have evaluated the basic biocompatibility of such coatings, a necessary step before moving forward with the development of a commercial medical device coating.

A number of studies have identified that ECM can have negative biological effects, in particular if decellularization is incomplete or if residual chemicals from decellularization process are left in ECM [227], [272]. It is, therefore, important to investigate the *in vitro* cytotoxicity of cell-derived ECM before moving forward with investigation in animal models. International Standards Organization (ISO) series 10993 explains standardized methods for stringent testing to ensure safety and biocompatibility of medical devices. In particular, a number of primary tests stand out that could assess the *in vitro* cytotoxicity of cell-type specific ECM, outlined in ISO 10993-5.

6.5.2 Methods

3T3/CCL-1 mouse fibroblast cells will be obtained frozen from a vendor and stored in liquid nitrogen with dimethylsulfoxide (DMSO) as a cryoprotectant. Cells will be seeded at a density of ~13,000 cell/cm^2 in cell culture polystyrene T-75 flasks. At confluence, as defined by > 95 % surface coverage, cells will be removed from culture plates with trypsin and reseeded at a density of 13,000 cells/cm^2 and grown to confluence again. 2nd passage or later cells will be used for all tests as specified by ISO 10993-5 Cytotoxicity Testing Requirements.

Once second passage cells are confluent, they will be subject to ECM exposure. Media will be swapped with media that has been supplemented with cell-type specific ECM at a concentration of 0.1 mg/mL, 1 mg/mL and 2 mg/mL and cells will be incubated in this media for 48 hours. After exposure to conditioned media, cells will be allowed to recover for 24 hours in standard DMEM/F12 media.

After a 24-hour recovery period, cells will be tested for viability using ISO 10993-5: Annex C – MTT Cytotoxicity Test. In brief, 24 hours after ECM exposure cell culture media will be substituted with media containing 5 mg/mL 3-(4,5-dimethylthiazol-2-yl)-2,5-diphenyltetrazolium bromide (MTT) and no phenol red. Cells metabolize MTT and store it internally as formazan, which has a punctate purple color. After 1-hour incubation, MTT media will be removed and replaced with 90 % isopropanol, which will lyse cells and solubilize formazan crystals. The light absorbance will be measured at 570 nm with a plate reader to quantify amount of formazan produced. Positive (no treatment) and negative (ethanol incubation) controls will serve to give baseline values for low cytotoxicity and high cytotoxicity. Percent cell viability will be calculated by diving optical density of treated cells by optical density of untreated cells; this will produce a % viability. If viability is reduced to < 70 % of blank, the ECMs have cytotoxic potential.

Treated cells will also be tested for viability using Calcein AM and Ethidium Bromide. Reagent will be used as per manufacturer's specifications to stain viable cells green and dead cells red. Briefly, 24 hours after incubation in ECM-treated media, growth media will be replaced with Hanks Balanced Salt Solution containing 2 μM Ethidium homodimer-1 and 1 μM Calcein AM. Cells will be incubated for 30 minutes and then imaged under a fluorescent inverted microscope. Dead cells fluoresce at 635 nm (red) and live cells fluoresce at 520 nm (green). Cells from 10 fields-of-view will be manually counted and live/dead percentage calculated. A decrease of greater than 80 % cell viability will be considered a fail condition.

All test will be performed with n = 24 per condition and compared using a student’s t-test. Experimental observations that fall outside of 1.5x the interquartile range (IQR) will be removed as outliers.

6.5.3 Expected Outcomes

It is not expected that any ECMs tested will have notable cytotoxic potential, but these tests are a necessary step to ensure safety of ECM as a surface adsorbed device coating. Cell-type specific ECM is secreted by viable, living cells, and as such presents minimal concern for cytotoxicity. The decellularization process utilized (see Chapter 4) is detergent free and also avoids the use of chemical crosslinkers or organic solvents to decellularize. One potential concern for cytotoxicity is residual DNA fragments, which can be cytotoxic to living cells. However, cell-type specific ECM has been incubated in DNAse for a sufficient time to enzymatically digest any free floating DNA, mitigating this concern. We expect these tests will add to the growing evidence that ECM as a surface adsorbed device coating can improve the biocompatibility of implanted medical devices.

6.6 Future Work Aim 3: Acute Implantation Study

6.6.1 Background

The implantation of a high density penetrating microelectrode invariably ruptures vasculature and creates areas of hemorrhage along electrode tracts and in adjacent tissue [10], [11]. Experimental intracerebral hemorrhage has shown that blood products accumulated in the brain parenchyma have deleterious effects on neuronal viability and lead to areas of tissue loss much larger that original damage area [29]. Limiting hemorrhage after iatrogenic injury is an approach that this dissertation pursued to improve the tissue response to implanted UEAs. While ECM showed utility in an *in vitro* assay, the acute biological response to UEAs coated with a hemostatic agent has not been explored.

ECM derived from animal tissue is utilized daily in the neurosurgical unit to manage negative impacts of cerebral hemorrhage due to its ability to mimic the normal hemostatic mechanisms that stabilize bleeding and limit neural cell death after vascular rupture [274]. Specific platelet binding motifs interact with platelets via glycoprotein VI receptor pathways to signal aggregation and degranulation, releasing factors that accelerate the coagulation cascade [225], [274], [275]. ECM has been utilized as a device coating for single shank devices, and high density penetrating devices like the UEA (this work), and has been shown to influence the FBR to implanted biomaterials. While ECMs role as a hemostat has been speculated as a mechanism of action, no work has focused on determining if ECM does, in fact, accelerate hemostasis at the device interface.

6.6.2 Methods

In order to determine if a hemostatic ECM can limit implant associated intracerebral hemorrhage cohorts of Sprague Dawley rats (n = 5, group) will be implanted with unmodified UEAs or UEAs dip coated with Avitene™, a strongly hemostatic ECM, and examined for blood product accumulation at 24 hours. Using coating and surgical approaches described in this dissertation, animals will be implanted and devices left freely floating using an unanchored approach. After a 24-hour indwelling period animals will be sacrificed via terminal perfusion and brains sectioned in the coronal plane in order to investigate tissue damage and blood product accumulation as a function of depth into cortex.

Using immunohistochemical techniques developed in this dissertation, coronal sections will be analyzed to assess the area of hemorrhage surrounding the implant site and compared statistically. IgG immunoreactivity will be compared by analyzing sections under the base and determining the IgG spread areas, as defined by IgG immunoreactivity above a set threshold intensity, from the implant site. The degree of microglial activation, as indicated by CD68 immunolabeling, will be quantified, as the activation of these cells is dependent on exposure to serum components [276]. Additionally, the presence of blood in the brain can be observed under light microscopy due to the red color of hemosiderin in red blood cells, allowing estimation of the volume of blood accumulated in the cortical parenchyma.

6.6.3 Progress/Expected Outcomes

Preliminary work has implanted 10 Male Sprague Dawley rats with coated and uncoated (n = 5/group) UEAs and investigated the response at 24 hours post injury. Immunohistological evaluation at this time point showed the tissue response to implanted UEAs to be highly variable within cohorts and no statistically significant differences were noted in any compared metrics. It was observed that implantation creates large areas of IgG immunoreactivity that extend millimeters away from implant site (**Figure 6.1**). Concurrent with this IgG immunoreactivity was microglial activation denoted by IBA-1+ cells with a high degree of CD68 expression. Microglia with an amoeboid morphology were more prevalent in the ipsilateral hemisphere and in particular near the implant location. IBA-1 expression also showed preferential elongation of microglia towards injury areas, with most cells with a 1mm radius extending a single, leading process in the direction of implant-associated damage. Light microscopy revealed the presence of blood product accumulation along the electrode shafts and into the cortical parenchyma. DAPI labeling showed that as soon as 24 hours after implant the surface of the devices were colonized with cells at a much higher density than is found in surrounding cortical parenchyma; these cells did not label positively for GFAP or IBA-1, and are possibly neutrophils.

Toward the goals of this investigation, the high variability in reaction observed within cohorts made statistical analysis inconclusive. While Avitene™ coated devices were qualitatively observed to have decreased areas of blood product accumulation and IgG spread area, the difference in means was not large enough to be captured with a student's t-test. Power analysis of the preliminary data indicates that in order to determine a 50 % reduction in means with the observed 50 % standard deviation at an 80 % power with 95 confidence, 16 animals per cohort would be needed.

6.7 Concluding Remarks

This dissertation aimed to improve functionality of a clinically utilized BMI with a goal of restoring sensation to paralyzed and amputated individuals. Improvements in the functionality of such devices could lead to drastic improvements in the standard of care, allowing these people to control their own world instead of relying on assistive in home care. At present, we rely heavily on such people to volunteer for clinical trials that explore device functionality. Their incredible sacrifices have proven that BMI technology is not science fiction, but rather an obtainable goal within this century. As device designers and investigators, we work fervently to make incremental improvements in device functionality, towards an end goal of reconnecting these patients with the outside world and providing them a degree of independence not previously available.

The goal of this work was to identify a number of strategies that could improve the tissue response and long-term functionality of such devices, with a goal of moving BMI technology closer to clinical acceptance. It is my hope that this body of work will inspire device designers to use biologically informed approaches when designing the next generation of implantable microelectrode arrays.

In particular, it seems necessary that design changes are implemented that take into effect the high vascular density of the cortex. This dissertation has shown that implantation of a high density device creates a significant focal cerebral insult that, independent of the FBR, causes a loss of neural tissue in the vicinity of recording electrodes. These lesion cavities are filled in with fibrous connective tissue that is rich in activated macrophages that likely exacerbate tissue remodeling and the ensuing FBR. Steps to address this meningeal encapsulation response and minimize connective tissue growth under the array will greatly benefit the field of Neural Engineering. Parallel improvements in device and hardware design, implantation strategies and inline signal processing will be required to move BMI technology towards clinical acceptance. It is my hope that one day paralyzed individuals can interact more easily with their world; this will be culmination of decades of research that have sought to make BMI technology a tangible reality.

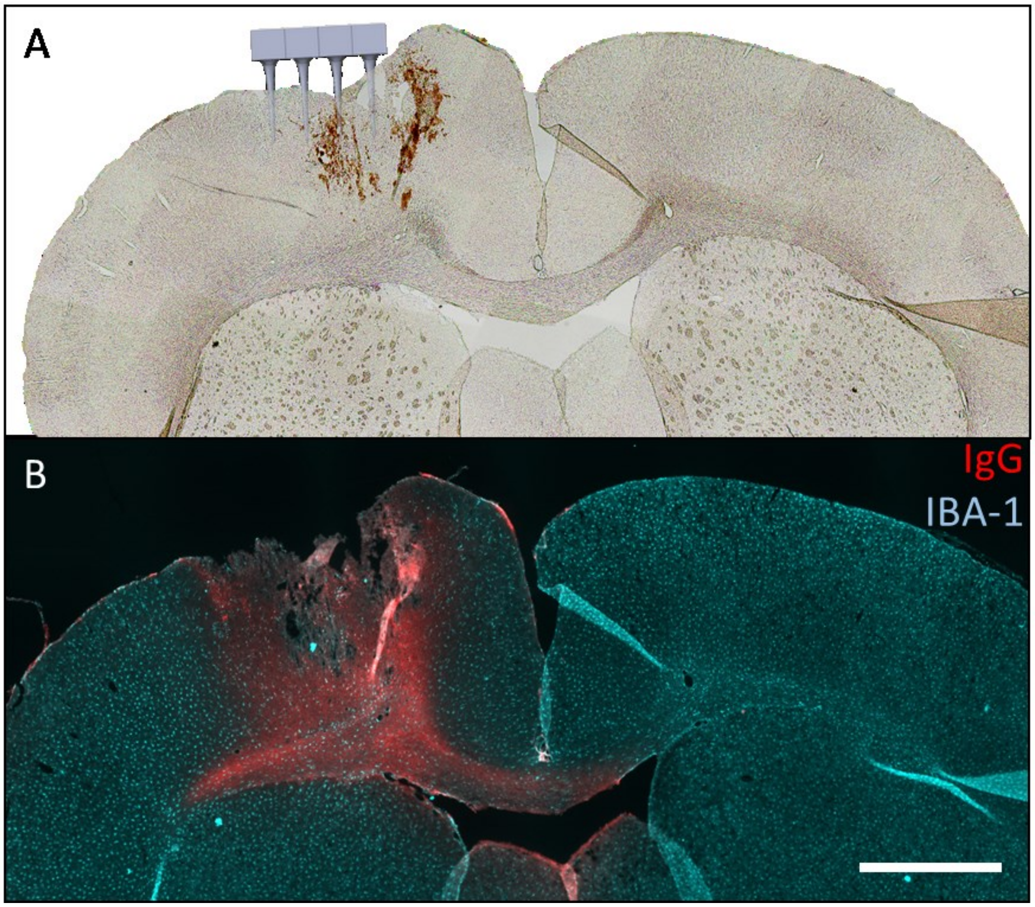

Figure 6.1 Coronal section showing blood product accumulation 24 hours after implant. A) Bright field image from a tissue section under an uncoated UEA showing target device implantation location and the presence of blood 24 hours after implantation. B) The same section view with immunohistochemical labels for IgG (red) and IBA-1 (cyan), showing plasma product accumulation that diffuse much farther into cortical parenchyma than blood products. Scale bar 1 mm.

REFERENCES

[1] J. C. Barrese *et al.*, “Failure mode analysis of siliconbased intracortical microelectrode arrays in nonhuman primates,” *J. Neural Eng.*, vol. 10, no. 6, p. 660, Nov. 2013.

[2] J. D. Simeral, S. P. Kim, M. J. Black, J. P. Donoghue, and L. R. Hochberg, “Neural control of cursor trajectory and click by a human with tetraplegia 1000 days after implant of an intracortical microelectrode array,” *J. Neural Eng.*, vol. 8, no. 2, p. 250, Mar. 2011.

[3] R. Biran, D. C. Martin, and P. A. Tresco, “Neuronal cell loss accompanies the brain tissue response to chronically implanted silicon microelectrode arrays,” *Exp. Neurol.*, vol. 195, no. 1, pp. 115–26, Sep. 2005.

[4] J. C. Williams, J. A. Hippensteel, J. Dilgen, W. Shain, and D. R. Kipke, “Complex impedance spectroscopy for monitoring tissue responses to inserted neural implants,” *J. Neural Eng.*, vol. 4, no. 4, pp. 410–423, Nov. 2007.

[5] G. C. McConnell, R. J. Butera, and R. V. Bellamkonda, “Bioimpedance modeling to monitor astrocytic response to chronically implanted electrodes,” *J. Neural Eng.*, vol. 6, no. 5, Sep. 2009.

[6] M. A. Freire *et al.*, “Comprehensive analysis of tissue preservation and recording quality from chronic multielectrode implants,” *PLoS One*, vol. 6, no. 11, pp. 23–27, Nov. 2011.

[7] N. F. Nolta, M. B. Christensen, P. D. Crane, J. L. Skousen, and P. A. Tresco, “BBB leakage, astrogliosis, and tissue loss correlate with silicon microelectrode array recording performance,” *Biomaterials*, vol. 53, pp. 753–762, Jun. 2015.

[8] D. F. Williams, “On the mechanisms of biocompatibility,” *Biomaterials*, vol. 29, no. 20, pp. 2941–53, Jul. 2008.

[9] J. Collias and E. Manuelidis, “Histopathological changes produced by implanted electrodes in cat brains,” *J. Neurosurg.*, vol. 14, no. 3, pp. 302–328, May 1957.

[10] P. A. House, J. D. MacDonald, P. A. Tresco, and R. A. Normann, "Acute microelectrode array implantation into human neocortex: Preliminary technique and histological considerations," *Neurosurg. Focus*, vol. 20, no. 5, p. E4, May 2006.

[11] E. Fernandez *et al.*, "Acute human brain responses to intracortical microelectrode arrays: Challenges and future prospects," *Front. Neuroeng.*, vol. 7, p. 24, Jul. 2014.

[12] P. J. Rousche and R. A. Normann, "Chronic recording capability of the Utah intracortical electrode array in cat sensory cortex," *J. Neurosci. Methods*, vol. 82, no. 1, pp. 1–15, Jul. 1998.

[13] E. M. Maynard, E. Fernandez, and R. A. Normann, "A technique to prevent dural adhesions to chronically implanted microelectrode arrays," *J. Neurosci. Methods*, vol. 97, no. 2, pp. 93–101, Apr. 2000.

[14] J. C. Barrese, J. Aceros, and J. P. Donoghue, "Scanning electron microscopy of chronically implanted intracortical microelectrode arrays in nonhuman primates," *J. Neural Eng.*, vol. 13, no. 2, p. 26003, Jan. 2016.

[15] P. A. Cody, J. R. Eles, C. F. Lagenaur, T. D. Y. Kozai, and X. T. Cui, "Unique electrophysiological and impedance signatures between encapsulation types: An analysis of biological Utah array failure and benefit of a biomimetic coating in a rat model," *Biomaterials*, vol. 161, pp. 117–128, Feb. 2018.

[16] X. Liu, *et al.*, "Stability of the interface between neural tissue and chronically implanted intracortical microelectrodes," *IEEE Trans. Rehabil. Eng.*, vol. 7, no. 3, pp. 315–326, Sep. 1999.

[17] S. Suner, M. R. Fellows, C. Vargas-Irwin, G. K. Nakata, and J. P. Donoghue, "Reliability of signals from a chronically implanted, silicon-based electrode array in nonhuman primate primary motor cortex," *IEEE Trans. Neural Syst. Rehabil. Eng.*, vol. 13, no. 4, pp. 524–541, Dec. 2005.

[18] J. A. Perge *et al.*, "Reliability of directional information in unsorted spikes and local field potentials recorded in human motor cortex," *J. Neural Eng.*, vol. 11, no. 4, p. 46007, Jun. 2014.

[19] M. P. Ward, P. Rajdev, C. Ellison, and P. P. Irazoqui, "Toward a comparison of microelectrodes for acute and chronic recordings," *Brain Res.*, vol. 1282, pp. 183–200, May 2009.

[20] D. McCreery, V. Pikov, and P. R. Troyk, "Neuronal loss due to prolonged controlled-current stimulation with chronically implanted microelectrodes in the cat cerebral cortex," *J. Neural Eng.*, vol. 7, no. 3, p. 36005, May 2010.

[21] R. Biran, D. C. Martin, and P. A. Tresco, "The brain tissue response to implanted

silicon microelectrode arrays is increased when the device is tethered to the skull," *J. Biomed. Mater. Res. Part A*, vol. 82A, pp. 169–178, Jan. 2007.

[22] J. Thelin *et al.*, "Implant size and fixation mode strongly influence tissue reactions in the CNS," *PLoS One*, vol. 6, no. 1, p. 16267, Jan. 2011.

[23] L. Karumbaiah *et al.*, "Relationship between intracortical electrode design and chronic recording function," *Biomaterials*, vol. 34, no. 33, pp. 8061–8074, Jul. 2013.

[24] N. T. Markwardt, J. Stokol, and R. L. Rennaker, "Sub-meninges implantation reduces immune response to neural implants," *J. Neurosci. Methods*, vol. 214, no. 2, pp. 119–125, Jan. 2013.

[25] A. Ersen, S. Elkabes, D. S. Freedman, and M. Sahin, "Chronic tissue response to untethered microelectrode implants in the rat brain and spinal cord," *J. Neural Eng.*, vol. 12, no. 1, p. 16019, Jan. 2015.

[26] A. Y. Shih *et al.*, "The smallest stroke: Occlusion of one penetrating vessel leads to infarction and a cognitive deficit," *Nat. Neurosci.*, vol. 16, no. 1, pp. 55–63, Dec. 2012.

[27] J. K. Ryu and J. G. McLarnon, "A leaky blood-brain barrier, fibrinogen infiltration and microglial reactivity in inflamed Alzheimer's disease brain," *J. Cell. Mol. Med.*, vol. 13, no. 9 A, pp. 2911–2925, Jul. 2009.

[28] D. Davalos and K. Akassoglou, "Fibrinogen as a key regulator of inflammation in disease," *Semin. Immunopathol.*, vol. 34, no. 1, pp. 43–62, Oct. 2012.

[29] M. Xue and M. R. Del Bigio, "Intracortical hemorrhage injury in rats," *Stroke*, vol. 31, pp. 1721–1727, Jul. 2000.

[30] M. C. Shearer and J. W. Fawcett, "The astrocyte/meningeal cell interface - A barrier to successful nerve regeneration?," *Cell Tissue Res.*, vol. 305, no. 2, pp. 267–273, Aug. 2001.

[31] M. Berry *et al.*, "Deposition of scar tissue in the central nervous system," in *Trauma and Regeneration: Special Symposium of the 9th International Congress of Neuropathology, Vienna, September 1982*, J. H. Adams, Ed. Vienna: Springer Vienna, pp. 31–53, Sep. 1983.

[32] J. E. Burda and M. V. Sofroniew, "Reactive gliosis and the multicellular response to CNS damage and disease," *Neuron*, vol. 81, no. 2, pp. 229–248, Jan. 2014.

[33] Y. T. Kim, R. W. Hitchcock, M. J. Bridge, and P. A. Tresco, "Chronic response of adult rat brain tissue to implants anchored to the skull," *Biomaterials*, vol. 25, no. 12, pp. 2229–2237, May 2004.

[34] F. Lapierre, S. D. Houtaud, and M. Wager, “Hemostatic agents in neurosurgery,” *Explic. Cases Controv. Issues Neurosurg.* pp. 505–5018, Oct. 2012.

[35] H. Ghuman *et al.*, “Long-term retention of ECM hydrogel after implantation into a sub-acute stroke cavity reduces lesion volume,” *Acta Biomater.*, vol. 63, pp. 50-63, Sep. 2017.

[36] Y. Wu *et al.*, “Implantation of brain-derived extracellular matrix enhances neurological recovery after traumatic brain injury,” *Cell Transplant.*, vol. 26, no. 7, pp. 1224–1234, Jul. 2017.

[37] W. He, G. C. McConnell, and R. V. Bellamkonda, “Nanoscale laminin coating modulates cortical scarring response around implanted silicon microelectrode arrays,” *J. Neural Eng.*, vol. 3, no. 4, pp. 316–26, Dec. 2006.

[38] G. Lind, C. E. Linsmeier, J. Thelin, and J. Schouenborg, “Gelatine-embedded electrodes—a novel biocompatible vehicle allowing implantation of highly flexible microelectrodes,” *J. Neural Eng.*, vol. 7, no. 4, p. 46005, Jun. 2010.

[39] E. Azemi, C. F. Lagenaur, and X. T. Cui, “The surface immobilization of the neural adhesion molecule L1 on neural probes and its effect on neuronal density and gliosis at the probe/tissue interface,” *Biomaterials*, vol. 32, no. 3, pp. 681–92, Jan. 2011.

[40] R. S. Oakes, M. D. Polei, J. L. Skousen, and P. A. Tresco, “An astrocyte derived extracellular matrix coating reduces astrogliosis surrounding chronically implanted microelectrode arrays in rat cortex,” *Biomaterials*, vol. 154, pp. 1–11, Oct. 2017.

[41] A. B. Jackson, M. Dijkers, M. J. Devivo, and R. B. Poczatek, “A demographic profile of new traumatic spinal cord injuries: Change and stability over 30 years,” *Arch. Phys. Med. Rehabil.*, vol. 85, no. 11, pp. 1740–1748, Nov. 2004.

[42] A. Burns and C. O’Connell, “Spinal cord injury facts and figures at a glance,” *Spinal Cord Inj. Stat. Cent.*, vol. 33, pp. 439-40, Feb. 2015.

[43] M. DeVivo, Y. Chen, S. Mennemeyer, and A. Deutsch, “Costs of care following spinal cord injury,” *Top. Spinal Cord Inj. Rehabil.*, vol. 16, no. 4, pp. 1–9, May 2011.

[44] V. Y Ma, L. Chan, and K. J. Carruthers, “The incidence, prevalence, costs and impact on disability of common conditions requiring rehabilitation in the US,” *Arch Phys Med Rehabil*, vol. 95, no. 5, pp. 986–995, Jan. 2014.

[45] E. J. Benjamin *et al.*, "*Heart Disease and Stroke Statistics—2017 Update: A Report From the American Heart Association*, vol. 135, no. 10. Jan. 2017.

[46] J. H. Jang, Y. G. Song, and Y. Z. Kim, “Predictors of 30-day mortality and 90-day functional recovery after primary pontine hemorrhage,” *J. Korean Med. Sci.*, vol.

26, no. 1. pp. 100–107, Jan. 2011.

[47] K. Ziegler-Graham, E. J. MacKenzie, P. L. Ephraim, T. G. Travison, and R. Brookmeyer, “Estimating the prevalence of limb loss in the United States: 2005 to 2050,” *Arch. Phys. Med. Rehabil.*, vol. 89, no. 3, pp. 422–429, Mar. 2008.

[48] A. Prochazka, V. K. Mushahwar, D. B. Mccreery, and D. Neuroscience, “Topical review neural prostheses,” *J. Physiol*, vol. 533, pp. 99–109, Nov. 2001.

[49] R. A. Markei, “Hearing aids market by product - Global forecasts to 2020,” ResearchandMarkets.com, Los Angeles, CA, USA, Tech. Rep. NGL-006, Nov. 2015.

[50] R. Cooper, A. Winter, H. Crow, and W. G. Walter, “Comparison of subcortical, cortical and scalp activity using chronically indwelling electrodes in man,” *Electroencephalogr. Clin. Neurophysiol.*, vol. 18, no. 3, pp. 217–228, Feb. 1965.

[51] W. J. Freeman, M. D. Holmes, B. C. Burke, and S. Vanhatalo, “Spatial spectra of scalp EEG and EMG from awake humans,” *Clin. Neurophysiol.*, vol. 114, no. 6, pp. 1053–1068, Jun. 2003.

[52] H. Grundfest and B. Campbell, “Origin, conduction and termination of impulses in the dorsal spino-cerebellar tract of cats,” *J. Neurophysiol.*, vol. 5, no. 4, pp. 275-294, Jul. 1942.

[53] F. R. Robinson and M. T. Johnson, “Histopathological studies of tissue reactions to various metals implanted in cat brains,” *ASD Tech. Rep.,* vol. 61, no. 397, Oct. 1961.

[54] M. Salcman and M. J. Bak, “A new chronic recording intracortical microelectrode,” *Med. Biol. Eng.*, vol. 14, no. 1, pp. 42–50, Jan. 1976.

[55] E. M. Schmidt, M. J. Bak, and J. S. McIntosh, “Long-term chronic recording from cortical neurons,” *Exp. Neurol.*, vol. 52, no. 3, pp. 496–506, Sep. 1976.

[56] K. D. Wise, J. B. Angell, and A. Starr, “An integrated-circuit approach to extracellular microelectrodes,” *IEEE Trans. Biomed. Eng.*, vol. BME-17, no. 3, pp. 238–247, Jul. 1970.

[57] S. L. BeMent, K. D. Wise, D. J. Anderson, K. Najafi, and K. L. Drake, “Solid-state electrodes for multichannel multiplexed intracortical neuronal recording,” *IEEE Trans. Biomed. Eng.*, vol. BME-33, no. 2, pp. 230–241, Feb. 1986.

[58] K. L. Drake, K. D. Wise, J. Farraye, D. J. Anderson, and S. L. BeMent, “Performance of planar multisite microprobes in recording extracellular single-unit intracortical activity,” *IEEE Trans. Biomed. Eng.*, vol. 35, no. 9, pp. 719–732, Sep. 1988.

[59] G. Buzsáki and A. Kandel, "Somadendritic backpropagation of action potentials in cortical pyramidal cells of the awake rat," *J. Neurophysiol.*, vol. 79, pp. 1587–1591, Mar. 1998.

[60] G. Buzsáki, "Large-scale recording of neuronal ensembles," *Nat. Neurosci.*, vol. 7, no. 5, pp. 446–451, May 2004.

[61] R. A. Normann, E. M. Maynard, P. J. Rousche, and D. J. Warren, "A neural interface for a cortical vision prosthesis," *Vision Res.*, vol. 39, no. 15, pp. 2577–87, Jul. 1999.

[62] S. J. Kim, S. C. Manyam, D. J. Warren, and R. A. Normann, "Electrophysiological mapping of cat primary auditory cortex with multielectrode arrays," *Ann. Biomed. Eng.*, vol. 34, no. 2, pp. 300–309, Feb. 2006.

[63] M. J. Lehmkuhle, R. A. Normann, and E. M. Maynard, "High-resolution analysis of the spatio-temporal activity patterns in rat olfactory bulb evoked by enantiomer odors," *Chem. Senses*, vol. 28, no. 6, pp. 499–508, Jul. 2003.

[64] T. Hillman, A. N. Badi, R. A. Normann, T. Kertesz, and C. Shelton, "Cochlear nerve stimulation with a 3-dimensional penetrating electrode array," *Otol. Neurotol.*, vol. 24, no. 5, pp. 764–768, Sep. 2003.

[65] R. S. Petersen and M. E. Diamond, "Spatial-temporal distribution of whisker-evoked activity in rat somatosensory cortex and the coding of stimulus location," *J. Neurosci.*, vol. 20, no. 16, pp. 6135–6143, Aug. 2000.

[66] L. R. Hochberg *et al.*, "Neuronal ensemble control of prosthetic devices by a human with tetraplegia," *Nature*, vol. 442, no. 7099, pp. 164–171, Jul. 2006.

[67] S. P. Kim, J. D. Simeral, L. R. Hochberg, J. P. Donoghue, and M. J. Black, "Neural control of computer cursor velocity by decoding motor cortical spiking activity in humans with tetraplegia," *J. Neural Eng.*, vol. 5, no. 4, pp. 455–76, Nov. 2008.

[68] J. Simeral, S.-P. Kim, M. J. Black, J. P. Donoghue, and L. R. Hochberg, "Neural control of cursor trajectory and click by a human with tetraplegia 1000 days after implant of an intracortical microelectrode array," *J. Neural Eng.*, vol. 8, no. 2, Mar. 2011.

[69] C. Chestek *et al.*, "Long-term stability of neural prosthetic control signals from silicon cortical arrays in rhesus macaque motor cortex," *J. Neural Eng.*, vol. 8, no. 4, p. 45005, Jul. 2011.

[70] L. R. Hochberg *et al.*, "Reach and grasp by people with tetraplegia using a neurally controlled robotic arm," *Nature*, vol. 485, no. 7398, pp. 372–375, May 2012.

[71] J. L. Collinger *et al.*, "High-performance neuroprosthetic control by an individual

with tetraplegia," *Lancet*, vol. 381, no. 9866, pp. 557–564, Feb. 2013.

[72] S. N. Flesher *et al.*, "Intracortical microstimulation of human somatosensory cortex," *Sci. Transl. Med.*, vol. 8, no. 361, pp. 1–11, Oct. 2016.

[73] M. Capogrosso *et al.*, "A brain-spinal interface alleviating gait deficits after spinal cord injury in primates," *Nature*, vol. 539, no. 7628, pp. 284–288, Nov. 2016.

[74] L. R. Hochberg *et al.*, "Reach and grasp by people with tetraplegia using a neurally controlled robotic arm," *Nature*, vol. 485, no. 7398, pp. 372–375, May 2012.

[75] A. B. Jarosiewicz, D. Bacher, A. A. Sarma, N. Y. Masse, and D. John, "Virtual typing by people with tetraplegia using a stabilized , self-calibrating intracortical brain-computer interface," *Sci. Transl. Medicne*, vol. 7, no. 313, pp. 1–11, Nov. 2015.

[76] A. B. Ajiboye *et al.*, "Restoration of reaching and grasping movements through brain-controlled muscle stimulation in a person with tetraplegia: a proof-of-concept demonstration," *Lancet*, vol. 389, no. 10081, pp. 1821–1830, Mar. 2017.

[77] P. J. Gilgunn, X. C. Ong, S. N. Flesher, A. B. Schwartz, and R. A. Gaunt, "Structural analysis of explanted microelectrode arrays," *Int. IEEE/EMBS Conf. Neural Eng. NER*, pp. 719–722, Nov. 2013.

[78] X. Xie *et al.*, "Long-term reliability of ALO2 and parylene c bilayer encapsulated Utah electrode array-based neural interfaces from chronic implantation," *J. Neural Eng.*, vol. 11, no. 2, pp. 1–23, Mar. 2014.

[79] A. Prasad *et al.*, "Abiotic-biotic characterization of Pt/Ir microelectrode arrays in chronic implants," *Front. Neuroeng.*, vol. 7, no. February, pp. 1–15, Feb. 2014.

[80] R. Caldwell *et al.*, "Analysis of Al2O3 Parylene-C bilayer coatings and impact of microelectrode topography on long term stability of implantable neural arrays," *J. Neural Eng.*, vol. 14, no. 4, Mar. 2017.

[81] M. Jorfi, J. L. Skousen, C. Weder, and J. R. Capadona, "Progress towards biocompatible intracortical microelectrodes for neural interfacing applications," *J. Neural Eng.*, vol. 12, no. 1, p. 11001, Oct. 2015.

[82] C. S. Bjornsson *et al.*, "Effects of insertion conditions on tissue strain and vascular damage during neuroprosthetic device insertion," *J. Neural Eng.*, vol. 3, no. 3, pp. 196–207, Jun. 2006.

[83] L. Tang, "Mechanisms of fibrinogen domains : Biomaterial interactions," *J. Biomater. Sci. Polym. Ed.*, vol. 9, no. 12, pp. 1257–1266, Jan. 1998.

[84] S. A. Smith, R. J. Travers, and J. H. Morrissey, "How it all starts: Initiation of the clotting cascade," *Crit. Rev. Biochem. Mol. Biol.*, vol. 50, no. 4, pp. 326–336,

May 2015.

[85] K. R. Lee, A. L. Betz, S. Kim, R. F. Keep, and J. T. Hoff, “The role of the coagulation cascade in brain edema formation after intracerebral hemorrhage,” *Acta Neurochir.*, vol. 138, no. 4, pp. 396–401, May 1996.

[86] M. J. Fisher, “Brain regulation of thrombosis and hemostasis from theory to practice,” *Stroke*, vol. 44, no. 11, pp. 3275–3285, Nov. 2013.

[87] G. Broughton, J. E. Janis, and C. E. Attinger, "The basic science of wound healing," *Plas. Reconstr. Surg.,* vol. 117, no. 1, pp. 12-34, Jun. 2006.

[88] B. Nilsson, K. N. Ekdahl, T. E. Mollnes, and J. D. Lambris, “The role of complement in biomaterial-induced inflammation,” *Mol. Immunol.*, vol. 44, no. 1, pp. 82–94, Jan. 2007.

[89] J. M. Anderson, A. Rodriguez, and D. T. Chang, “Foreign body reaction to biomaterials,” *Semin. Immunol.*, vol. 20, no. 2, pp. 86–100, Apr. 2008.

[90] B. D. Winslow, M. B. Christensen, W. K. Yang, F. Solzbacher, and P. A. Tresco, “A comparison of the tissue response to chronically implanted Parylene-C-coated and uncoated planar silicon microelectrode arrays in rat cortex,” *Biomaterials*, vol. 31, no. 35, pp. 9163–9172, Dec. 2010.

[91] J. L. Skousen *et al.*, “Reducing surface area while maintaining implant penetrating profile lowers the brain foreign body response to chronically implanted planar silicon microelectrode arrays,” *Prog. Brain Res.*, vol. 194, pp. 167–80, Jan. 2011.

[92] D. H. Szarowski, M. D. Andersen, S. Retterer, A. J. Spence, and M. Isaacson, “Brain responses to micromachined silicon devices,” vol. 983, pp. 23–35, Sep. 2003.

[93] J. Tanaka, K. Toku, M. Sakanaka, and N. Maeda, “Morphological differentiation of microglial cells in culture: Involvement of insoluble factors derived from astrocytes,” *Neurosci. Res.*, vol. 34, no. 4, pp. 207–15, Sep. 1999.

[94] A. Mantovani *et al.,* “The chemokine system in diverse forms of macrophage activation and polarization,” *Trends Immunol.*, vol. 25, no. 12, pp. 677–686, Dec. 2004.

[95] K. Kigerl, *et al.*, “Identification of two distinct macrophage subsets with divergent effects causing either neurotoxicity or regeneration in the injured mouse spinal cord,” *J. Neurosci.*, vol. 29, no. 43, pp. 13435–44, Oct. 2009.

[96] J. Skousen, K. Bolick, M. Bridge, and P. A. Tresco, “A predictive model of the foreign body response to devices implanted chronically in the central nervous system,” *Int. Electr. Funct. Stimul. Soc.*, Conference, Sep. 2012.

[97] J. M. Anderson, “Multinucleated giant cells,” *Curr. Opin. Hematol.*, vol. 7, no. 1, Jan. 2000.

[98] D. J. Edell, V. Van Toi, V. M. McNeil, and L. D. Clark, “Factors influencing the biocompatibility of insertable silicon microshafts in cerebral cortex,” *IEEE Trans. Biomed. Eng.*, vol. 39, no. 6, pp. 635–643, Jun. 1992.

[99] S. A. Liddelow *et al.*, “Neurotoxic reactive astrocytes are induced by activated microglia,” *Nature*, vol. 541, no. 7638, pp. 481–487, Jan. 2017.

[100] M. Pekny and M. Nilsson, “Astrocyte activation and reactive gliosis,” *Glia*, vol. 50, no. 4, pp. 427–434, Jun. 2005.

[101] J. N. Turner *et al.*, “Cerebral astrocyte response to micromachined silicon implants,” *Exp. Neurol.*, vol. 156, no. 1, pp. 33–49, Mar. 1999.

[102] R. L. Schultz and T. J. Willey, “The ultrastructure of the sheath around chronically implanted electrodes in brain,” *J. Neurocytol.*, vol. 5, no. 6, pp. 621–642, Dec. 1976.

[103] T. Roitbak and E. Syková, “Diffusion barriers evoked in the rat cortex by reactive astrogliosis,” *Glia*, vol. 28, no. 1, pp. 40–48, Oct. 1999.

[104] C. C. Stichel and H. W. Mller, “The CNS lesion scar: New vistas on an old regeneration barrier,” *Cell Tissue Res.*, vol. 294, no. 1, pp. 1–9, Oct. 1998.

[105] S. S. Stensaas and L. J. Stensaas, “Histopathological evaluation of materials implanted in the cerebral cortex,” *Acta Neuropathol.*, vol. 41, no. 2, pp. 145–55, Feb. 1978.

[106] B. D. Winslow and P. A. Tresco, “Quantitative analysis of the tissue response to chronically implanted microwire electrodes in rat cortex,” *Biomaterials*, vol. 31, no. 7, pp. 1558–67, Mar. 2010.

[107] J. L. Skousen, M. J. Bridge, and P. A. Tresco, “A strategy to passively reduce neuroinflammation surrounding devices implanted chronically in brain tissue by manipulating device surface permeability,” *Biomaterials*, vol. 36, pp. 33–43, Oct. 2014.

[108] T. Saxena *et al.*, “The impact of chronic blood-brain barrier breach on intracortical electrode function,” *Biomaterials*, vol. 34, no. 20, pp. 4703–4713, Apr. 2013.

[109] A. Sawyer and T. R. Kyriakides, “Nanoparticle-based evaluation of blood brain-barrier leakage during the foreign body response,” *J. Neural Eng.*, vol. 10, no. 1, pp. 1741–2560, Jan. 2013.

[110] N. J. Abbott, A. K. Patabendige, D. E. M. Dolman, S. R. Yusof, and D. J. Begley, “Structure and function of the blood-brain barrier,” *Neurobiol. Dis.*, vol. 37, no. 1,

pp. 13–25, Jan. 2010.

[111] B. T. Hawkins and T. P. Davis, "The blood-brain barrier / neurovascular unit in health and disease," *Pharmacol. Rev.*, vol. 57, no. 2, pp. 173–185, Jun. 2005.

[112] J. Tanaka and N. Maeda, "Microglial ramification requires nondiffusible factors derived from astrocytes," *Exp. Neurol.*, vol. 137, no. 2, pp. 367–375, Feb. 1996.

[113] A. Alonso, E. Reinz, M. Fatar, M. G. Hennerici, and S. Meairs, "Clearance of albumin following ultrasound-induced blood-brain barrier opening is mediated by glial but not neuronal cells," *Brain Res.*, vol. 1411, pp. 9–16, Sep. 2011.

[114] R. A. Adams *et al.*, "The fibrin-derived $\gamma^{377\text{-}395}$ peptide inhibits microglia activation and suppresses relapsing paralysis in central nervous system autoimmune disease," *J. Exp. Med.*, vol. 204, no. 3, pp. 571–582, Mar. 2007.

[115] V. Jolivel *et al.*, "Perivascular microglia promote blood vessel disintegration in the ischemic penumbra," *Acta Neuropathol.*, vol. 129, no. 2, pp. 279–295, Feb. 2015.

[116] M. Scholz, J. Cinatl, M. Schädel-Höpfner, and J. Windolf, "Neutrophils and the blood-brain barrier dysfunction after trauma," *Med. Res. Rev.*, vol. 27, no. 3, pp. 401–416, May 2007.

[117] P. L. McGeer and E. G. McGeer, "The inflammatory response system of brain: Implications for therapy of Alzheimer and other neurodegenerative diseases," *Brain Res. Rev.*, vol. 21, no. 2, pp. 195–218, Sep. 1995.

[118] M. A. Puchowicz *et al.*, "Diet-induced ketosis increases capillary density without altered blood flow in rat brain," *Am. J. Physiol. Endocrinol. Metab.*, vol. 292, no. 6, pp. 1607–1615, Jun. 2007.

[119] W. F. Agnew, T. G. H. Yuen, D. B. McCreery, and L. A. Bullara, "Histopathologic evaluation of prolonged intracortical electrical stimulation," *Exp. Neurol.*, vol. 92, no. 1, pp. 162–185, Apr. 1986.

[120] N. F. Nolta, "Studies of intracortical microelectrode array performance and foreign body response in young and aged rats," *PhD Dissertation*, BioEng., U. of Ut., Salt Lake City, UT, 2016.

[121] S. Schmidt, K. Horch, and R. Normann, "Biocompatibility of silicon-based electrode arrays implanted in feline cortical tissue," *J. Biomed. Mater. Res.*, vol. 27, no. 11, pp. 1393–1399, Nov. 1993.

[122] S. Kim *et al.*, "Integrated wireless neural interface based on the Utah electrode array," *Biomed. Microdevices*, vol. 11, no. 2, pp. 453–466, Apr. 2009.

[123] J. Muthuswamy, A. Gilletti, T. Jain, and M. Okandan, "Microactuated neural probes to compensate for brain micromotion," *2003 Annu. Int. Conf. IEEE Eng.*

Med. Biol. Soc., vol. 2, pp. 1941–1943, Sep. 2003.

[124] H. Lee, R. V. Bellamkonda, W. Sun, and M. E. Levenston, “Biomechanical analysis of silicon microelectrode-induced strain in the brain,” *J. Neural Eng.*, vol. 2, no. 4, pp. 81–89, Dec. 2005.

[125] J. Subbaroyan and D. R. Kipke, “The role of flexible polymer interconnects in chronic tissue response induced by intracortical microelectrodes - A modeling and an in vivo study,” *Annu. Int. Conf. IEEE Eng. Med. Biol. Proc.*, vol. 1, pp. 3588–3591, Sep. 2006.

[126] P. Moshayedi *et al.*, “The relationship between glial cell mechanosensitivity and foreign body reactions in the central nervous system,” *Biomaterials*, vol. 35, no. 13, pp. 3919–25, Apr. 2014.

[127] A. Gilletti and J. Muthuswamy, “Brain micromotion around implants in the rodent somatosensory cortex,” *J. Neural Eng.*, vol. 3, no. 3, pp. 189–195, Sep. 2006.

[128] P. J. Rousche and R. A. Normann, “A method for pneumatically inserting an array of penetrating electrodes into cortical tissue,” *Ann. Biomed. Eng.*, vol. 20, no. 4, pp. 413–422, May 1992.

[129] C. T. Nordhausen, P. J. Rousche, and R. A. Normann, “Optimizing recording capabilities of the Utah intracortical electrode array,” *Brain Res.*, vol. 637, no. 1–2, pp. 27–36, Feb. 1994.

[130] D. F. Rolfe and G. C. Brown, “Cellular energy utilization and molecular origin of standard metabolic rate in mammals,” *Physiol. Rev.*, vol. 77, no. 3, pp. 731–758, Jul. 1997.

[131] D. Begley and M. Brightman, "Structural and functional aspects of the blood-brain barrier," *Prog. Brain Res.*, vol. 61. Sep. 2003.

[132] P. S. Tsai *et al.*, “Correlations of neuronal and microvascular densities in murine cortex revealed by direct counting and colocalization of nuclei and vessels,” *J. Neurosci.*, vol. 29, no. 46, pp. 14553–14570, Nov. 2009.

[133] F. Lauwers, F. Cassot, V. Lauwers-Cances, P. Puwanarajah, and H. Duvernoy, “Morphometry of the human cerebral cortex microcirculation: General characteristics and space-related profiles,” *Neuroimage*, vol. 39, no. 3, pp. 936–948, Feb. 2008.

[134] Y. Miyoshi, I. Date, and T. Ohmoto, “Three-dimensional morphological study of microvascular regeneration in cavity wall of the rat cerebral cortex using the scanning electron microscope: Implications for delayed neural grafting into brain cavities,” *Exp. Neurol.*, vol. 131, no. 1, pp. 69–82, Jan. 1995.

[135] H. M. M. Duvernoy, S. Delon, and J. L. L. Vannson, “Cortical blood vessels of the

human brain," *Brain Res. Bull.*, vol. 7, no. 5, pp. 519–578, Nov. 1981.

[136] P. Blinder *et al.*, "The cortical angiome: An interconnected vascular network with noncolumnar patterns of blood flow," *Nat. Neurosci.*, vol. 16, no. 7, pp. 889–97, Jun. 2013.

[137] B. Weber, A. L. Keller, J. Reichold, and N. K. Logothetis, "The microvascular system of the striate and extrastriate visual cortex of the macaque," *Cereb. Cortex*, vol. 18, no. 10, pp. 2318–2330, Jan. 2008.

[138] B. V. Zlokovic, "The blood-brain barrier in health and chronic neurodegenerative disorders," *Neuron*, vol. 57, no. 2, pp. 178–201, Jan. 2008.

[139] K. Baeten and K. Akassoglou, "Extracellular matrix and matrix receptors in blood-Brain barrier formation and stroke," *Dev. Neurobiol.*, vol. 71, no. 11, pp. 1018–1039, Nov. 2012.

[140] V. Brundula, N. B. Rewcastle, L. M. Metz, C. C. Bernard, and V. W. Yong, "Targeting leukocyte MMPs and transmigration: Minocycline as a potential therapy for multiple sclerosis," *Brain*, vol. 125, no. 6, pp. 1297–1308, Jun. 2002.

[141] G. Allt and J. G. Lawrenson, "Pericytes: Cell biology and pathology," *Cells Tissues Organs*, vol. 169, no. 1, pp. 1–11, Aug. 2001.

[142] C. M. Peppiatt, C. Howarth, P. Mobbs, and D. Attwell, "Bidirectional control of CNS capillary diameter by pericytes," *Nature*, vol. 443, no. 7112, pp. 700–704, Oct. 2006.

[143] N. J. Abbott, L. Rönnbäck, and E. Hansson, "Astrocyte–endothelial interactions at the blood–brain barrier," *Nat. Rev. Neurosci.*, vol. 7, no. 1, pp. 41–53, Jan. 2006.

[144] H. Wolburg, S. Noell, A. Mack, K. Wolburg-Buchholz, and P. Fallier-Becker, "Brain endothelial cells and the glio-vascular complex," *Cell Tissue Res.*, vol. 335, no. 1, pp. 75–96, Jan. 2009.

[145] N. Abbott, "Astrocyte–endothelial interactions and blood–brain barrier permeability," *J. Anat.*, vol. 200, pp. 629– 638, Jun. 2002.

[146] C. M. Anderson and M. Nedergaard, "Astrocyte-mediated control of cerebral microcirculation," *Trends Neurosci.*, vol. 26, no. 7, pp. 340–344, Jul. 2003.

[147] J. Defelipe, L. Alanso-Nanclares, and J. Arellano, "Microstructure of the neocortex comparative aspects," *J. Neurocytol.*, vol. 31, pp. 299–316, Mar. 2002.

[148] J. DeFelipe, "The evolution of the brain, the human nature of cortical circuits, and intellectual creativity," *Front. Neuroanat.*, vol. 5, p. 29, May 2011.

[149] F. A. C. Azevedo *et al.*, "Equal numbers of neuronal and nonneuronal cells make

the human brain an isometrically scaled-up primate brain," *J. Comp. Neurol.*, vol. 513, no. 5, pp. 532–541, Apr. 2009.

[150] J. Nguyen, N. Nishimura, R. N. Fetcho, C. Iadecola, and C. B. Schaffer, "Occlusion of cortical ascending venules causes blood flow decreases, reversals in flow direction, and vessel dilation in upstream capillaries," *J. Cereb. Blood Flow Metab.*, vol. 31, no. 11, pp. 2243–2254, Jun. 2011.

[151] T. G. Bush *et al.*, "Leukocyte infiltration , neuronal degeneration , and neurite outgrowth after ablation of scar-forming, reactive astrocytes in adult transgenic mice," *Neuron*, vol. 23, pp. 297–308, Jun. 1999.

[152] I. Kwon, E. H. Kim, G. J. del Zoppo, and J. H. Heo, "Ultrastructural and temporal changes of the microvascular basement membrane and astrocyte interface following focal cerebral ischemia," *J. Neurosci. Res.*, vol. 87, no. 3, pp. 668–676, Feb. 2009.

[153] A. Nimmerjahn, F. Kirchhoff, and F. Helmchen, "Resting microglial cells are highly dynamic surveillants of brain parenchyma in vivo," vol. 308, no. 5, pp. 1314–1319, May 2005.

[154] E. Baumann, E. Preston, J. Slinn, and D. Stanimirovic, "Postischemic hypothermia attenuates loss of the vascular basement membrane proteins, agrin and SPARC, and the blood-brain barrier disruption after global cerebral ischemia," *Brain Res.*, vol. 1269, pp. 185–197, May 2009.

[155] G. Stoll, S. Jander, and M. Schroeter, "Inflammation and glial responses in ischemic brain lesions," *Prog. Neurobiol.*, vol. 56, no. 2, pp. 149–171, Oct. 1998.

[156] M. Xue and M. R. Del Bigio, "Intracerebral injection of autologous whole blood in rats: Time course of inflammation and cell death," *Neurosci. Lett.*, vol. 283, no. 3, pp. 230–232, Apr. 2000.

[157] S. J. Campbell *et al.*, "Central nervous system injury triggers hepatic CC and CXC chemokine expression that is associated with leukocyte mobilization and recruitment," vol. 166, no. 5, pp. 1487–1497, Jan. 2005.

[158] H. D. Soares, R. R. Hicks, D. Smith, and T. K. McIntosh, "Inflammatory leukocytic recruitment and diffuse neuronal degeneration are separate pathological processes resulting from traumatic brain injury," *J. Neurosci.*, vol. 15, no. 12, pp. 8223–33, Dec. 1995.

[159] U. K. Hanisch and H. Kettenmann, "Microglia: Active sensor and versatile effector cells in the normal and pathologic brain," *Nat. Neurosci.*, vol. 10, no. 11, pp. 1387–1394, Oct. 2007.

[160] M. T. Fitch, C. Doller, C. K. Combs, G. E. Landreth, and J. Silver, "Cellular and molecular mechanisms of glial scarring and progressive cavitation: In vivo and in

vitro analysis of inflammation-induced secondary injury after CNS trauma," *J. Neurosci.*, vol. 19, no. 19, pp. 8182–98, Oct. 1999.

[161] H. Kawano *et al.*, "Role of the lesion scar in the response to damage and repair of the central nervous system," *Cell Tissue Res.*, vol. 349, no. 1, pp. 169–180, Feb. 2012.

[162] I. B. Wanner *et al.*, "Glial scar borders are formed by newly proliferated, elongated astrocytes that interact to corral inflammatory and fibrotic cells via STAT3-dependent mechanisms after spinal cord injury," *J. Neurosci.*, vol. 33, no. 31, pp. 12870–12886, Jul. 2013.

[163] J. Silver, M. A. Edwards, and P. Levitt, "Immunocytochemical demonstration of early appearing astroglial structures that form boundaries and pathways along axon tracts in the fetal brain," *J. Comp. Neurol.*, vol. 328, no. 3, pp. 415–436, Feb. 1993.

[164] F. M. Bareyre *et al.*, "The injured spinal cord spontaneously forms a new intraspinal circuit in adult rats," *Nat. Neurosci.*, vol. 7, no. 3, pp. 269–277, Feb. 2004.

[165] S. T. Carmichael, "Cellular and molecular mechanisms of neural repair after stroke: Making waves," *Ann. Neurol.*, vol. 59, no. 5, pp. 735–742, Apr. 2006.

[166] V. S. Polikov, P. A. Tresco, and W. M. Reichert, "Response of brain tissue to chronically implanted neural electrodes," *J. Neurosci. Meth.*, vol. 148, no. 1, pp. 1–18, Oct. 2005.

[167] M. Goss-Varley *et al.*, "Microelectrode implantation in motor cortex causes fine motor deficit: Implications on potential considerations to Brain Computer Interfacing and Human Augmentation," *Sci. Rep.*, vol. 7, no. 1, pp. 1–12, Nov. 2017.

[168] S. Nabeshima, T. S. Reese, D. M. D. Landis, and M. W. Brightman, "Junctions in the meninges and marginal glia," *J. Comp. Neurol.*, vol. 164, no. 2, pp. 127–169, Nov. 1975.

[169] R. J. Vetter, J. C. Williams, J. F. Hetke, E. A. Nunamaker, and D. R. Kipke, "Chronic neural recording using silicon-substrate microelectrode arrays implanted in cerebral cortex," *IEEE Trans. Biomed. Eng.*, vol. 51, no. 6, pp. 896–904, Jun. 2004.

[170] C. Bernards and H. Hill, "Morphine and alfentanil permeability through the spinal dura, arachnoid, and pia mater of dogs and monkeys," *Anesthesiology*, vol. 73, no. 6, pp. 1214–1219, Dec. 1990.

[171] E. T. Zhang, C. B. Inman, and R. O. Weller, "Interrelationships of the pia mater and the perivascular (Virchow-Robin) spaces in the human cerebrum," *J. Anat.*, vol. 170, pp. 111–23, Jun. 1990.

[172] A. W. L. Maxwell, R. Follows, D. E. Ashhurst, and M. Berry, “The response of the cerebral hemisphere of the rat to injury,” *Phil. Trans. R. Soc. Lond.*, vol. 328, no. 1250, pp. 479–500, Jun. 1990.

[173] A. L. Carbonell and J. Boya, “Ultrastructural study on meningeal regeneration and meningo-glial relationships after cerebral stab wound in the adult rat,” *Brain Res.*, vol. 439, no. 1–2, pp. 337–344, Jan. 1988.

[174] L. Q. Bundesen, T. A. Scheel, B. S. Bregman, and L. F. Kromer, “Ephrin-B2 and EphB2 regulation of astrocyte-meningeal fibroblast interactions in response to spinal cord lesions in adult rats,” *J. Neurosci.*, vol. 23, no. 21, pp. 7789–800, Aug. 2003.

[175] A. Logan *et al.*, “Effects of transforming growth factor β1, on scar production in the injured central nervous system of the rat,” *Eur. J. Neurosci.*, vol. 6, no. 3, pp. 355–363, Mar. 1994.

[176] C. C. Stichel *et al.*, “Inhibition of collagen IV deposition promotes regeneration of injured CNS axons,” *Eur. J. Neurosci.*, vol. 11, no. 2, pp. 632–646, Feb. 1999.

[177] Y. River, A. Schwartz, J. M. Gomori, D. Soffer, and T. Siegal, “Clinical significance of diffuse dural enhancement detected by magnetic resonance imaging,” *J. Neurosurg.*, vol. 85, no. 5, pp. 777–783, Nov. 1996.

[178] L. M. Mellema, V. F. Samii, K. M. Vernau, and R. A. Lecouteur, “Meningeal enhancement on magnetic resonance imaging in 15 dogs and 3 cats,” *Vet. Radiol. Ultrasound*, vol. 43, no. 1, pp. 10–15, Jan. 2002.

[179] E. C. Bourekas, J. S. Lewin, and C. F. Lanzieri, “Postcontrast meningeal MR enhancement secondary to intracranial hypotension caused by lumbar puncture,” *J. Comput. Assist. Tomogr.*, vol. 19, no. 2, pp. 299–301, Mar. 1995.

[180] J. W. Burke, A. E. Podrasky, and W. G. Bradley, “Meninges: Benign postoperative enhancement on MR images,” *Radiology*, vol. 174, no. 1, pp. 99–102, Jun. 1990.

[181] D. S. Martin, E. E. Awwad, and T. Pittman, “Meningeal fibrosis appearing shortly after ventricular shunting,” *Am. J. Neuroradiol.*, vol. 11, no. 3. p. 617, May 1990.

[182] L. T. Saldin, M. C. Cramer, S. S. Velankar, L. J. White, and S. F. Badylak, “Extracellular matrix hydrogels from decellularized tissues: Structure and function,” *Acta Biomater.*, vol. 49, pp. 1–15, Feb. 2017.

[183] D. M. Faulk *et al.*, “ECM hydrogel coating mitigates the chronic inflammatory response to polypropylene mesh,” *Biomaterials*, vol. 35, no. 30, pp. 8585–95, Oct. 2014.

[184] M. T. Wolf *et al.*, “Polypropylene surgical mesh coated with extracellular matrix mitigates the host foreign body response,” *J. Biomed. Mater. Res. A*, vol. 102, no.

1, pp. 234–46, Jan. 2014.

[185] S. Hou *et al.*, “The repair of brain lesion by implantation of hyaluronic acid hydrogels modified with laminin,” *J. Neurosci. Meth.*, vol. 148, no. 1, pp. 60–70, Oct. 2005.

[186] F. Z. Cui, W. M. Tian, S. P. Hou, Q. Y. Xu, and I. S. Lee, “Hyaluronic acid hydrogel immobilized with RGD peptides for brain tissue engineering,” *J. Mater. Sci. Mater. Med.*, vol. 17, no. 12, pp. 1393–1401, Dec. 2006.

[187] Y. T. Wei *et al.*, “Hyaluronic acid hydrogels with IKVAV peptides for tissue repair and axonal regeneration in an injured rat brain,” *Biomed. Mater.*, vol. 2, no. 3, Jul. 2007.

[188] M. M. H, Ghuman *et al.*, “ECM hydrogel for the treatment of stroke: Characterization of the host cell infiltrate,” *Biomaterials*, vol. 91, pp. 166–181, Mar. 2016.

[189] T. L. Sellaro, A. K. Ravindra, D. B. Stolz, and S. F. Badylak, “Maintenance of hepatic sinusoidal endothelial cell phenotype *in vitro* using organ-specific extracellular matrix scaffolds,” *Tissue Eng.*, vol. 13, no. 9, pp. 2301–2310, Sep. 2007.

[190] J. Cortiella *et al.*, “Influence of acellular natural lung matrix on murine embryonic stem cell differentiation and tissue formation,” *Tissue Eng. Part A*, vol. 16, no. 8, pp. 2565–2580, Aug. 2010.

[191] T. J. Keane *et al.*, “Tissue-specific effects of esophageal extracellular matrix,” *Tissue Eng. Part A*, vol. 21, no. 17, pp. 2293–2300, Sep. 2015.

[192] J. L. Dziki *et al.*, “Solubilized extracellular matrix bioscaffolds derived from diverse source tissues differentially influence macrophage phenotype,” *J. Biomed. Mater. Res.*, vol. 105, no. 1, pp. 138–147, Jan. 2017.

[193] W. He, G. C. McConnell, and R. V Bellamkonda, “Nanoscale laminin coating modulates cortical scarring response around implanted silicon microelectrode arrays,” *J. Neural Eng.*, vol. 3, no. 4, pp. 316–26, Dec. 2006.

[194] A. M. Dymond, L. E. Kaechele, J. M. Jurist, and P. H. Crandall, “Brain tissue reaction to some chronically implanted metals,” *J. Neurosurg.*, vol. 33, no. 5, pp. 574–80, Nov. 1970.

[195] T. L. Babb and W. Kupfer, “Phagocytic and metabolic reactions to chronically implanted metal brain electrodes,” *Exp. Neurol.*, vol. 86, no. 2, pp. 171–182, Nov. 1984.

[196] W. M. Grill and J. Thomas Mortimer, “Electrical properties of implant encapsulation tissue,” *Ann. Biomed. Eng.*, vol. 22, no. 1, pp. 23–33, Jun. 1994.

[197] C. T. Nordhausen, E. M. Maynard, and R. A. Normann, “Single unit recording capabilities of a 100 microelectrode array,” *Brain Res.*, vol. 726, no. 1–2, pp. 129–140, Jul. 1996.

[198] D. J. Warren, E. Fernandez, and R. A. Normann, “High-resolution two-dimensional spatial mapping of cat striate cortex using a 100-microelectrode array,” *Neuroscience*, vol. 105, no. 1, pp. 19–31, Jul. 2001.

[199] A. A. Linninger *et al.*, “Cerebral microcirculation and oxygen tension in the human secondary cortex,” *Ann. Biomed. Eng.*, vol. 41, no. 11, pp. 2264–2284, Jul. 2013.

[200] J. Reichold *et al.*, “Vascular graph model to simulate the cerebral blood flow in realistic vascular networks,” *J. Cereb. Blood Flow Metab.*, vol. 29, no. 8, pp. 1429–1443, May 2009.

[201] L. Risser *et al.*, “From homogeneous to fractal normal and tumorous microvascular networks in the brain,” *J. Cereb. Blood Flow Metab.*, vol. 27, no. 2, pp. 293–303, Feb. 2007.

[202] J. P. Donoghue, A. Nurmikko, M. Black, and L. R. Hochberg, “Assistive technology and robotic control using motor cortex ensemble-based neural interface systems in humans with tetraplegia,” *J. Physiol.*, vol. 579, pp. 603–611, Mar. 2007.

[203] P. Stice, A. Gilletti, A. Panitch, and J. Muthuswamy, “Thin microelectrodes reduce GFAP expression in the implant site in rodent somatosensory cortex,” *J. Neural Eng.*, vol. 4, no. 2, pp. 42–53, Jun. 2007.

[204] G. Paxinos and C. Watson, *The Rat Brain in Stereotaxic Coordinates*, 2nd Edition. San Diego: Academic Press, Inc., 1986.

[205] S. Roth and I. Freund, “Coherent optical harmonic generation in rat-tail tendon,” *Opt. Commun.*, vol. 33, no. 3, pp. 292–296, Jun. 1980.

[206] A. Sharma, L. Rieth, P. Tathireddy, R. Harrison, and F. Solzbacher, “Long term in vitro stability of fully integrated wireless neural interfaces based on Utah slant electrode array,” *Appl. Phys. Lett.*, vol. 96, no. 7, pp. 1–13, Jan. 2010.

[207] A. Mantovani, S. K. Biswas, M. R. Galdiero, A. Sica, and M. Locati, “Macrophage plasticity and polarization in tissue repair and remodelling,” *J. Pathol.*, vol. 229, no. 2, pp. 176–185, Jan. 2013.

[208] C. Larochelle, J. I. Alvarez, and A. Prat, “How do immune cells overcome the blood-brain barrier in multiple sclerosis?,” *FEBS Lett.*, vol. 585, no. 23, pp. 3770–3780, May 2011.

[209] G. C. McConnell *et al.*, “Implanted neural electrodes cause chronic, local inflammation that is correlated with local neurodegeneration,” *J. Neural Eng.*, vol.

6, no. 5, p. 56003, Oct. 2009.

[210] M. B. Ariganello, D. T. Simionescu, R. S. Labow, and J. Michael Lee, "Macrophage differentiation and polarization on a decellularized pericardial biomaterial," *Biomaterials*, vol. 32, no. 2, pp. 439–449, Jan. 2011.

[211] N. Sadr *et al.*, "Enhancing the biological performance of synthetic polymeric materials by decoration with engineered, decellularized extracellular matrix," *Biomaterials*, vol. 33, no. 20, pp. 5085–5093, Jul. 2012.

[212] B. N. Brown, J. E. Valentin, A. M. Stewart-Akers, G. P. McCabe, and S. F. Badylak, "Macrophage phenotype and remodeling outcomes in response to biologic scaffolds with and without a cellular component," *Biomaterials*, vol. 30, no. 8, pp. 1482–91, Mar. 2009.

[213] L. Huleihel *et al.*, "Macrophage phenotype in response to ECM bioscaffolds," *Semin. Immunol.*, vol. 29, no. April, pp. 2–13, Feb. 2017.

[214] D. Giulian and J. Baker, "Characterization of ameboid mammalian brain microglia isolated from developing brain," *J. Neurosci. Methods*, vol. 6, pp. 2163–2178, Aug. 1986.

[215] M. S. Rao, M. Noble, and M. Mayer-Pröschel, "A tripotential glial precursor cell is present in the developing spinal cord," *Proc. Natl. Acad. Sci. U. S. A.*, vol. 95, no. 7, pp. 3996–4001, Mar. 1998.

[216] M. Soleimani and S. Nadri, "A protocol for isolation and culture of mesenchymal stem cells from mouse bone marrow," *Nat. Protoc.*, vol. 4, no. 1, pp. 102–106, Feb. 2009.

[217] J. C. Wolchok and P. A. Tresco, "The isolation of cell derived extracellular matrix constructs using sacrificial open-cell foams," *Biomaterials*, vol. 31, no. 36, pp. 9595–603, Dec. 2010.

[218] M. Ni and M. Aschner, "Neonatal rat primary microglia: Isolation, culturing and selected applications," *Curr. Prot. Toxicol.*, pp. 1–20, Feb. 2010.

[219] W. R. Wagner, J. M. Pachence, J. Ristich, and P. C. Johnson, "Comparative in vitro analysis of topical hemostatic agents," *J. Surg. Res.*, vol. 66, no. 2, pp. 100–8, Dec. 1996.

[220] H. H. I. Yao, M. K. H. Hong, and K. J. Drummond, "Haemostasis in neurosurgery: What is the evidence for gelatin-thrombin matrix sealant?," *J. Clin. Neurosci.*, vol. 20, no. 3, pp. 349–356, Mar. 2013.

[221] S. Schermer, *The Blood Morphology of Laboratory Animals*. 3rd ed. Philidelphia, PA, USA: F. A. Davis Company, 1967.

[222] W. D. Spotnitz and S. Burks, “Hemostats, sealants, and adhesives: Components of the surgical toolbox,” *Transfusion*, vol. 48, no. 7, pp. 1502–16, Jul. 2008.

[223] W. D. Spotnitz and S. Burks, “Hemostats, sealants, and adhesives III: A new update as well as cost and regulatory considerations for components of the surgical toolbox,” *Transfusion*, vol. 52, no. 10, pp. 2243–55, Oct. 2012.

[224] M. Gabay and B. A. Boucher, “An essential primer for understanding the role of topical hemostats, surgical sealants, and adhesives for maintaining hemostasis,” *Pharmacotherapy*, vol. 33, no. 9, pp. 935–955, Sep. 2013.

[225] R. W. Farndale, J. J. Sixma, M. J. Barnes, and P. G. de Groot, “The role of collagen in thrombosis and hemostasis,” *J. Thromb. Haemost.*, vol. 2, no. 4, pp. 561–73, Apr. 2004.

[226] S. F. Badylak, “Xenogeneic extracellular matrix as a scaffold for tissue reconstruction,” *Transpl. Immunol.*, vol. 12, no. 3–4, pp. 367–77, Apr. 2004.

[227] P. M. Crapo, T. W. Gilbert, and S. F. Badylak, “An overview of tissue and whole organ decellularization processes,” *Biomaterials*, vol. 32, no. 12, pp. 3233–43, Apr. 2011.

[228] D. Faulk *et al.*, “The effect of detergents on the basement membrane complex of a biologic scaffold material,” *Acta Biomater.*, vol. 10, no. 1, pp. 1841–1850, Jan. 2014.

[229] Y. Zhang *et al.*, “Tissue-specific extracellular matrix coatings for the promotion of cell proliferation and maintenance of cell phenotype,” *Biomaterials*, vol. 30, no. 23–24, pp. 4021–4028, Aug. 2009.

[230] N. C. Cheng, B. T. Estes, H. A. Awad, and F. Guilak, “Chondrogenic differentiation of adipose-derived adult stem cells by a porous scaffold derived from native articular cartilage extracellular matrix,” *Tissue Eng. Part A*, vol. 15, no. 2, pp. 231–41, Feb. 2009.

[231] T. L. Sellaro *et al.*, “Maintenance of human hepatocyte function in vitro by liver-derived extracellular matrix gels,” *Tissue Eng. Part A*, vol. 16, no. 3, pp. 1075–82, Mar. 2010.

[232] M. Van Der Rest and R. Garrone, “Collagen family of proteins,” *FASEB J.*, vol. 5, no. 13, pp. 2814–2823, Oct. 1991.

[233] W. L. Maxwell, V. C. Duance, M. Lehto, D. E. Ashurst, and M. Berry, “The distribution of types I, III, IV and V collagens in penetrant lesions of the central nervous system of the rat,” *Histochem. J.*, vol. 16, no. 11, pp. 1219–1229, Nov. 1984.

[234] D. Nikitovic, P. Katonis, A. Tsatsakis, N. K. Karamanos, and G. N. Tzanakakis,

“Lumican, a small leucine-rich proteoglycan,” *IUBMB Life*, vol. 60, no. 12, pp. 818–823, Dec. 2008.

[235] R. V. Lozzo and R. D. Sanderson, “Proteoglycans in cancer biology, tumour microenvironment and angiogenesis,” *J. Cell. Mol. Med.*, vol. 15, no. 5, pp. 1013–1031, May 2011.

[236] X. J. Liu *et al.*, “Lumican accelerates wound healing by enhancing α2β1 integrin-mediated fibroblast contractility,” *PLoS One*, vol. 8, no. 6, pp. 1–9, Jun. 2013.

[237] C. Denis *et al.*, “Localization of von Willebrand factor binding domains to endothelial extracellular matrix and to type VI collagen,” *Arterioscler. Thromb. Vasc. Biol.*, vol. 13, no. 3, pp. 398–406, Mar. 1993.

[238] N. A. DiProspero, S. Meiners, and H. M. Geller, “Inflammatory cytokines interact to modulate extracellular matrix and astrocytic support of neurite outgrowth,” *Exp. Neurol.*, vol. 148, no. 2, pp. 628–639, Dec. 1997.

[239] A. Rolls, R. Shechter, and M. Schwartz, “The bright side of the glial scar in CNS repair,” *Nat. Rev. Neurosci.*, vol. 10, p. 235, Mar. 2009.

[240] Y. Deguchi *et al.*, “Internalization of basic fibroblast growth factor at the mouse blood–brain barrier involves perlecan, a heparan sulfate proteoglycan,” *J. Neurochem.*, vol. 83, no. 2, pp. 381–389, Oct. 2002.

[241] M. Tenan *et al.*, “Thrombospondin-1 is downregulated by anoxia and suppresses tumorigenicity of human glioblastoma cells,” *J. Exp. Med.*, vol. 191, no. 10, pp. 1789–1798, May 2000.

[242] H. Wang *et al.*, “Peripheral administration of fetuin-A attenuates early cerebral ischemic injury in rats,” *J. Cereb. Blood Flow Metab.*, vol. 30, no. 3, pp. 493–504, Mar. 2010.

[243] J. Elsas *et al.*, “Fetuin-A in the developing brain,” *Dev. Neurobiol.*, vol. 73, no. 5, pp. 354–369, May 2013.

[244] M. Xue and M. R. Del Bigio, “Acute tissue damage after injections of thrombin and plasmin into rat striatum,” *Stroke*, vol. 32, no. 9, pp. 2164–2169, Sep. 2001.

[245] M. Xue and M. R. Del Bigio, “Injections of blood, thrombin, and plasminogen more severely damage neonatal mouse brain than mature mouse brain,” *Brain Pathol.*, vol. 15, no. 4, pp. 273–280, Oct. 2005.

[246] N. Aihara, H. Tanno, J. J. Hall, L. H. Pitts, and L. J. Noble, “Immunocytochemical localization of immunoglobulins in the rat brain: Relationship to the blood-brain barrier,” *J. Comp. Neurol.*, vol. 342, no. 4, pp. 481–496, Apr. 1994.

[247] K. A. F. Pulford, A. Sipos, J. L. Cordell, W. P. Stross, and D. Y. Mason,

"Distribution of the CD68 macrophage/myeloid associated antigen," *Int. Immunol.*, vol. 2, no. 10, pp. 973–980, Jul. 1990.

[248] J. E. Valentin, A. M. Stewart-Akers, T. W. Gilbert, and S. F. Badylak, "Macrophage participation in the degradation and remodeling of extracellular matrix scaffolds," *Tissue Eng. Part A*, vol. 15, no. 7, pp. 1687–1694, 2009.

[249] M. Walker, J. G. Kublin, and J. R. Zunt, "The effect of source animal age upon the in vivo remodeling characteristics of an extracellular matrix scaffold," *Biomaterials*, vol. 42, no. 1, pp. 115–125, Jul. 2009.

[250] N. J. Turner, S. A. Johnson, L. J. R. Foster, and S. F. Badylak, "Sutureless nerve repair with ECM bioscaffolds and laser-activated chitosan adhesive," *J. Biomed. Mater. Res. Part B Appl. Biomater.*, vol. 106, no. 5, pp. 1–14, Jul. 2017.

[251] C. Zhang *et al.*, "Improved cartilage regeneration utilizing mesenchymal stem cells in TGFb1 activated scaffolds," *Tissue Eng. Part A*, vol. 15, no. 9, pp. 2687–2698, 2009.

[252] B. N. Brown *et al.*, "Macrophage phenotype as a predictor of constructive remodeling following the implantation of biologically derived surgical mesh materials," *Acta Biomater.*, vol. 8, no. 3, pp. 978–87, Mar. 2012.

[253] B. M. Sicari *et al.*, "The promotion of a constructive macrophage phenotype by solubilized extracellular matrix," *Biomaterials*, vol. 35, no. 30, pp. 8605–12, Oct. 2014.

[254] M. R. Galdiero and A. Mantovani, "Macrophage plasticity and polarization: Relevance to biomaterials," *Host Response to Biomater.*, pp. 117–130, Oct. 2015.

[255] G. Gondo, T. Yamashita, Y. Ishiwata, K. Hirata, and M. Satoh, "Peculiar computed tomographic images after intracranial use of microfibrillar collagen hemostat: Report of three cases," *No Shinkei Geka.*, vol. 17, no. 11, p. 1067 - 71, Nov. 1989.

[256] T. Ribalta *et al.*, "Textiloma (gossypiboma) mimicking recurrent intracranial tumor," *Arch. Pathol.*, vol. 128, no. 7, pp. 749–758, Jul. 2004.

[257] B. A. O'Shaughnessy, K. T. Schafernak, A. J. DiPatri, S. Goldman, and T. Tomita, "A granulomatous reaction to Avitene mimicking recurrence of a medulloblastoma case report," *J. Neurosurg.*, vol. 104, no. 1, pp. 33–6, Jan. 2006.

[258] K. Ono, J. Hatada, K. Minamuria, I. Ohara, and K. Wada, "Delayed enlargement of brain edema after resection of intracranial meningioma," *Neurol. Med. Chir. (Tokyo).*, vol. 49, no. 10, pp. 478–481, Oct. 2009.

[259] L. Apel-Sarid, D. D. Cochrane, P. Steinbok, A. T. Byrne, and C. Dunham, "Microfibrillar collagen hemostat–induced necrotizing granulomatous

inflammation developing after craniotomy: A pediatric case series," *J. Neurosurg. Pediatr.*, vol. 6, no. 4, pp. 385–392, Oct. 2010.

[260] J. J. Graber, V. Tabar, C. Brennan, M. Rosenblum, and L. M. DeAngelis, "Acute inflammatory reactions to hemostatic materials mimicking postoperative intracranial abscess," *Interdiscip. Neurosurg. Adv. Tech. Case Manag.*, vol. 1, no. 1, pp. 5–7, Mar. 2014.

[261] S. M. Renati, S. Kaur, J. Kresak, M. Wicklund, and I. Malty, "Granulomatous meningitis secondary to Avitene (microfibrillar collagen)," *Neurol. Clin. Pract.*, vol. 7, no. 5, pp. 384–386, Sep. 2016.

[262] F. DeLustro *et al.*, "Reaction to injectable collagen: Results in animal models and clinical use," *Plast. Reconstr. Surg.*, vol. 79, no. 4, pp. 581-90, Apr. 1987.

[263] J. P. McCoy *et al.*, "Immune responses to bovine collagen implants: Significance of pretreatment serology," *J. Am. Acad. Dermatol.*, vol. 16, no. 5, pp. 955–960, May 1987.

[264] J. Keefe, L. Wauk, S. Chu, and F. DeLustro, "Clinical use of injectable bovine collagen: A decade of experience," *Clin. Mater.*, vol. 9, no. 3, pp. 155–162, Jan. 1992.

[265] F. Aragona, L. D'Urso, and R. Marcolongo, "Immunologic aspects of bovine injectable collagen in humans," *Eur. Urol.*, vol. 33, no. 2, pp. 129–133, Feb. 1998.

[266] G. Lind, L. Gällentoft, N. Danielsen, J. Schouenborg, and L. M. E. Pettersson, "Multiple implants do not aggravate the tissue reaction in rat brain," *PLoS One*, vol. 7, no. 10, p. e47509, Oct. 2012.

[267] A. A. Schendel *et al.*, "A cranial window imaging method for monitoring vascular growth around chronically implanted microECoG devices," *J. Neurosci. Methods*, vol. 218, no. 1, pp. 121–130, Aug. 2013.

[268] E. Ryapolova-Webb *et al.*, "Chronic cortical and electromyographic recordings from a fully implantable device: Preclinical experience in a nonhuman primate," *J. Neural Eng.*, vol. 11, no. 1, Feb. 2014.

[269] A. Degenhart *et al.*, "Histological evaluation of a chronically implanted electrocorticographic electrode grid in a nonhuman primate," *J. Neural Eng.*, vol. 13, no. 4, pp. 1–25, Aug. 2016.

[270] A. Schendel *et al.*, "The effect of microECoG substrate footprint on the meningeal tissue response," *J. Neural Eng.*, vol. 11, no. 4, pp. 305–315, Aug. 2014.

[271] A. A. Schendel *et al.*, "A cranial window imaging method for monitoring vascular growth around chronically implanted microECoG devices," *J. Neurosci. Methods*, vol. 218, no. 1, pp. 121–130, Aug. 2013.

[272] S. F. Badylak and T. W. Gilbert, “Immune response to biologic scaffold materials,” *Semin. Immunol.*, vol. 20, no. 2, pp. 109–116, Jun. 2009.

[273] J. Lok *et al.* , “Intracerebral Hemorrhage: mechanisms of secondary brain injury,” *Acta Neurochir. Suppl.*, vol. 111, pp. 63–69, Jun. 2011.

[274] C. G. Knight *et al.*, “Collagen-platelet interaction: Gly-Pro-Hyp is uniquely specific for platelet Gp VI and mediates platelet activation by collagen,” *Cardiovasc. Res.*, vol. 41, no. 2, pp. 450–7, Feb. 1999.

[275] J. Emsley, C. G. Knight, R. W. Farndale, M. J. Barnes, and R. C. Liddington, “Structural basis of collagen recognition by integrin alpha2beta1,” *Cell*, vol. 101, no. 1, pp. 47–56, Mar. 2000.

[276] M. A. Laurenzi, C. Arcuri, R. Rossi, P. Marconi, and V. Bocchini, “Effects of microenvironment on morphology and function of the microglial cell line BV-2,” *Neurochem. Res.*, vol. 26, no. 11, pp. 1209–16, Nov. 2001.